TUM School of Natural Sciences

Technische Universität München

Precise Measurement of Nuclear Interaction Cross Sections with R3B

Lukas Ponnath

Vollständiger Abdruck der von der TUM School of Natural Sciences der Technischen Universität München zur Erlangung des akademischen Grades eines

Doktors der Naturwissenschaften (Dr. rer. nat.)

genehmigten Dissertation.

Vorsitz:	Apl. Prof. Dr. Norbert Kaiser
Prüfer*innen der Dissertation:	1. Prof. Dr. Laura Fabbietti
	2. Prof. Dr. Lothar Oberauer

Die Dissertation wurde am 28.09.2023 bei der Technischen Universität München eingereicht und durch die TUM School of Natural Sciences am 23.10.2023 angenommen.

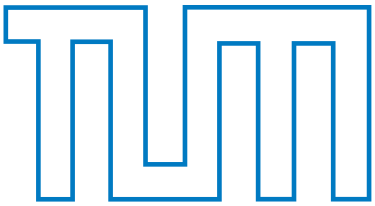

TUM School of Natural Sciences

Precise Measurement of Nuclear Interaction Cross Sections with R3B

Lukas Ponnath

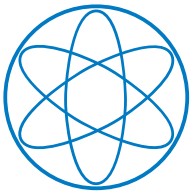

Techinsche Universität München

Fachbereich: Dense and Strange Hadronic Matter (E62)

2023

Abstract

Astrophysical observations of neutron stars (NS) provide rather precise data about the global properties of such unique and fascinating objects, e.g., the mass and radius. For the interpretation of this data and to gain a profound understanding of the inner structure of NS, it is essential to investigate nuclear matter under extreme conditions. A key instrument to describe nuclear matter over a wide density range is the equation of state (EOS). The radius and stability of NS are governed by the pressure of the highly asymmetric matter in the inside, which is defined by the so-called symmetry energy in the EOS. This quantity and especially its slope parameter L around nuclear saturation density are experimentally only weakly constraint so far.

A experimental attempt to constrain the L parameter is to measure the neutron-skin thickness of highly asymmetric nuclei since both quantities are directly correlated. One of the most established experimental methods to probe the nuclear density distribution is the measurement of total interaction cross section at radioactive beam facilities. A common method to describe integrated cross sections is the Glauber reaction model. In such a model, which includes realistic in-medium modification for composite nuclei, the only inputs are the experimental nucleon-nucleon cross sections and the density distribution of the projectile and target nucleus.

For a precise determination of the neutron-skin thickness of exotic nuclei, and thus to constrain the symmetry energy slope parameter, it is essential to quantify the uncertainty of the reaction model under ideal conditions.

This work provides a detailed summary of the precise measurement of total interaction cross sections of ^{12}C+^{12}C collisions in the energy regime between 400 and 1000 MeV/nucleon. The underlying experiment was carried out as part of the commissioning of the R^{3}B setup during the FAIR Phase-0 campaign at GSI. The present analysis of total interaction cross sections is based on a transmission measurement, where the numbers of incoming and non-reacted projectiles before and after the reaction target have been identified. The identification of the non-reacted ^{12}C poses a challenge to the experimental setup since the time- and rate-dependent detector efficiency, as well as the geometrical acceptance of the whole setup, have to be considered.

The presented cross sections was determined with a total experimental uncertainty down to 0.4 % and represent the most precise data currently available in this energy regime. The validity of the measurement and analysis method was confirmed by data from previous experiments. It was shown that predictions based on a realistic Glauber reaction model are in good agreement with the presented experimental results for low energy but overestimate them by around 2.5 % at higher energies.

Zusammenfassung

Astrophysikalische Beobachtungen von Neutronensternen (NS) liefern recht genaue Messdaten über globale Eigenschaften wie den Radius und die Masse dieser einzigartigen und faszinierenden Objekte. Um diese Daten zu interpretieren und ein profundes Verständnis über die innere Struktur von NS zu erhalten, ist es essenziell, nukleare Materie unter extremen Bedingungen zu untersuchen. Ein Schlüsselinstrument zur Beschreibung von nuklearer Materie über einen weiten Dichtebereich ist die Zustandsgleichung (EOS). Der Druck von hoch asymmetrischer Materie in einem NS definiert unter anderem die Struktur und Stabilität und wird in der EOS durch die sogenannte Symmetrieenergie beschrieben. Der Wertebereich für diesen Parameter und insbesondere der des zugehörigen Steigungsparameters L konnten bisher experimentell nicht präzise bestimmt werden.

Ein experimenteller Ansatz, um den L-Parameter zu bestimmen, ist die Messung der Dicke der Neutronenhaut von hoch asymmetrischen Kernen, da beide Parameter direkt korreliert sind. Eine der etabliertesten experimentellen Methoden für die Untersuchung der nuklearen Dichteverteilung ist die Messung von totalen Interaktions-Wirkungsquerschnitten an Beschleunigeranlagen für Ionenstrahlen. Eine gängige Methode zur theoretischen Beschreibung von integrierten Wirkungsquerschnitten ist das Glauber-Reaktionsmodell. In diesem Modell, welches In-Medium-Modifikationen für zusammengesetze Kerne enthält, werden nur der experimentelle Wirkungsquerschnitt von Nukleon-Nukleon-Kollisionen und die Dichteverteilung des Projektile- und Target-Kerns als Eingabe verwendet.

Für eine präzise Bestimmung der Neutronenhautdicke von exotischen Kernen und somit des Wertes für den Steigungsparameter L ist es essenziell, die Unsicherheit des Reaktionsmodells unter idealen Umständen zu quantifizieren.

Diese Arbeit liefert eine detaillierte Zusammenfassung der präzisen Messung totaler Interaktions-Wirkungsquerschnitte von ^{12}C+^{12}C-Kollisionen in einem Energiebereich von 400 bis 1000 MeV/nucleon. Als Teil der Inbetriebnahme des R^{3}B-Versuchsaufbaus wurde das zugehörige Experiment während der FAIR Phase-0 Kampagne an der GSI durchgeführt. Die vorliegende Analyse von totalen Interaktions-Wirkungsquerschnitten basiert auf einer Transmissionsmessung, bei der die Anzahl der einkommenden und nicht reagierenden Projektile vor und nach dem Reaktions-Target identifiziert wird. Insbesondere die Identifikation der nicht reagierenden ^{12}C-Kerne stellt eine Herausforderung für den Versuchsaufbau dar, da die zeit- und ratenabhängige Effizienz der Detektoren sowie die geometrische Akzeptanz des gesamten Aufbaus berücksichtigt werden müssen.

Die präsentierten Wirkungsquerschnitte wurden mit einer Messunsicherheit von bis zu 0.4 % bestimmt und stellen somit die genauesten, aktuell verfügbaren Messwerte in diesem Energiebereich dar. Die Validität der Messung und der Analysemethode wurde anhand von Messwerten früherer Experimente bestätigt werden. Es wurde gezeigt, dass Vorhersagen, welche auf einem realistischen Glauber-Reaktionsmodell basieren, mit den vorliegenden Messwerte bei niedrigen Energien übereinstimmen, diese jedoch bei hohen Energien um etwa 2.5 % überschätzen.

Contents

1 Introduction

The detection of gravitational wave signatures from neutron-star merger events during the last years promoted a strong experimental interest in studying the properties of nuclear matter on a high precision level. A detailed description of these reaction mechanisms requires the investigation of the composition inside a neutron star (NS) which could provide answers to many open questions in physics, such as the maximum mass of a NS, quark confinement inside the NS core and the synthesis of heavy elements. Therefore it is essential to investigate nuclear matter over a wide range of densities in terrestrial laboratories. This will provide stringent constraints for the interpretation and modeling of nuclear matter under such extreme conditions, generally described by the equation of state (EOS). The determination of one key parameter in the EOS, namely the slope parameter of the symmetry energy, via direct nuclear reactions is part of the scientific program of the R3B (Reactions with Relativistic Radioactive Beams) collaboration at the GSI/FAIR facility (Facility for Antiproton and Ion Research). An essential ingredient for this proposed technique is a realistic theoretical description of the reaction mechanism, including in-medium modifications inside a nucleus. This thesis presents a precise measurement of nuclear interaction cross sections to challenge such a realistic and extended reaction model using a ^{12}C beam at relativistic energies. The first part of this chapter briefly reviews the discovery and formation of neutron stars (NS) and introduces selected global properties obtained from astrophysical observations. Section 1.2 focuses on the EOS of asymmetric nuclear matter and its relation to these observations. In Section 1.3, the relation between the symmetry energy and the neutron-skin thickness is explained. There are several experimental approaches to determine the symmetry energy near saturation density [1], such as by studying nuclear electric dipole polarizability [2, 3] or to determine the neutron-skin thickness via the weak interaction by measuring the parity violating asymmetry [4, 5]. In this thesis, a experimental method is discussed to determine the neutron-skin thickness via nuclear fragmentation reactions. The experimental technique and the dependency on calculations based on the Glauber model are described in the following.

1.1 Neutron Stars

The existence of NS was predicted for the first time in 1934 by Baade and Zwicky [6] as a "transition of an ordinary star" to an object which consists "mainly of neutrons" and "possess a very small radius and an extremely high density". Remarkably, this hypothesis was made just two years after Chadwick's discovery of the neutron in 1932 [7]. Even though the first discovery of a NS took another three decades. In 1967

Bell-Burnell and Hewish measured a repeating signal from an extraterrestrial source at the Mullard Radio Astronomy Observatory in Cambridge, which they interpreted as a signal emitted from a white dwarf or a neutron star. Up to today more than 3000 NS have been discovered and categorized [8].

The investigation of NS is equivalent to an expedition in the world of nuclear matter under extreme conditions, far beyond the reach of terrestrial laboratories. The journey starts with the death of a massive star. At the end of the lifetime of a star with more than eight solar masses ($M_\odot$) [9] the inner core mainly consists of nuclei around ^{56}Fe as a final result of nuclear fusion reactions. When the energy gain of further fusion reactions dramatically drops, the radiation pressure cannot balance the gravitational force anymore. The main contribution of the stabilizing pressure in the star is yield by electrons in the core [10]. During the gravitational core collapse the matter becomes more and more neutron-rich induced by electron-capture processes. This process decreases the electron pressure and further accelerates the collapse. Electron-neutrinos, produced in these processes, become trapped inside the collapsing matter at a density of around 10^{-4}fm^{-3}. When matter inside the core reaches the nuclear saturation density n_0 the collapse suddenly halts due to the short-range repulsive nature of the nuclear force. This leads to a rebound of the core and triggers a shock wave that starts propagating from the inner core. If the shock wave fails to propagate the mass accretion continues and a black hole could be formed. Otherwise this shock wave could launch a supernova. The whole propagation mechanism is very complex and depends on many initial parameters e.g. the core and outer layer composition and neutrino heating/cooling processes [11, 12] and will not be discussed further in this work. A descriptive and detailed review of the evolution and forming of NS can be found in [13, 14, 15, 16].

1.1.1 Global Properties of Neutron Stars

The new-born "Proto-NS" still has a radius in the range of $\sim$ 100km and high temperature ($T \geq 10$ MeV). After a few seconds, the NS cools down ($T \leq 1$ MeV) due to neutrino emission and becomes a compact object. With a radius around $\sim$ 10km and a mass between 1.5 - 2 $M_\odot$ the NS reaches a central density of several times the nuclear saturation density n_o.

Their compactness and relatively low temperature ($T_N \ll E_{Fermi}$) make the NS unique in the observable universe, but also challenging to study. The tremendous technical progress of astrophysical telescopes and detectors e.g. LIGO or NICER allows to measure NS masses and radii. Whereas the mass measurement could be achieved quite precisely, the radius measurement is more complicated. The radius determination mostly includes the distance of the compact object to the observer, which is on the

scale of several hundred light-years, and therefore represents the most significant uncertainty. Fig. 1 shows the mass-radius relation of a gravitational-wave measurement of a NS binary system (GW170817 [17]), of a NICER measurement of a millisecond pulsar (PSR J0030+0451 [18] and the mass measurement of the heaviest NS observed so far (J0740+6620) via a Shapiro delay measurement [19]. The colored solid and dashed lines represent mass-radius-curves based on different microscopic and phenomenological theories [16]. To understand which quantities have to be included in such a calculation and how the mass-radius-curve can be used to interpret the astrophysical observations of the global properties of a NS, it is necessary to have a closer look to its inner composition and structure.

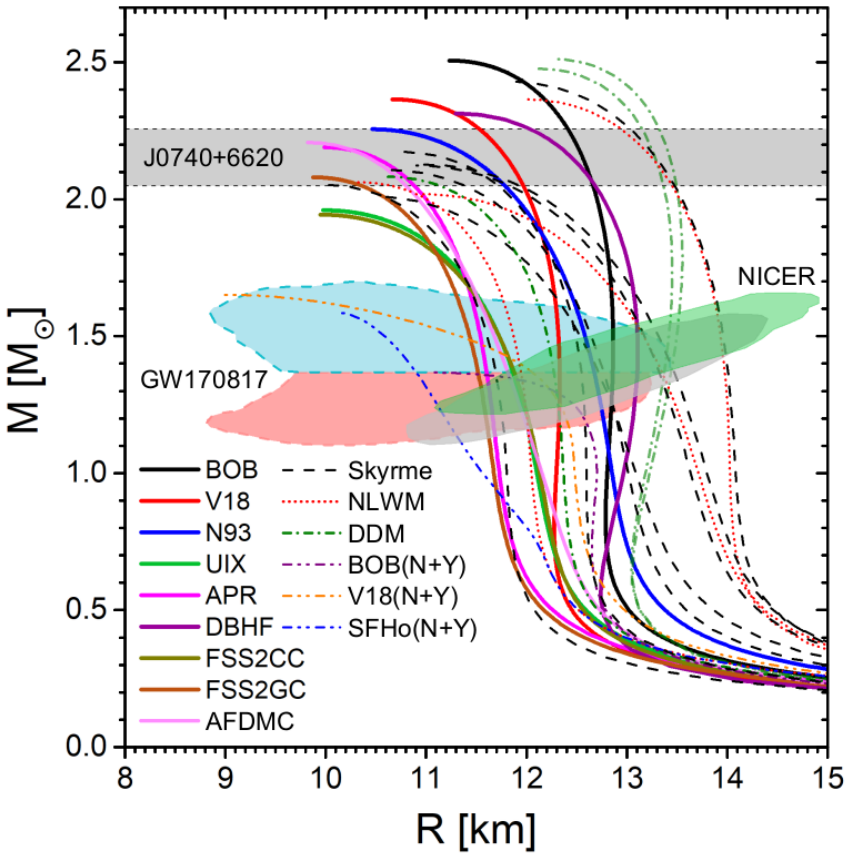

Figure 1: The mass-radius relation from a gravitational wave signal (GW170817 [17]), a NICER analysis [18] and of the heaviest NS observed so far J0740+6620 [19]. The different lines represent relations obtained by different microscopic (solid) and phenomenological (dashed) EOS. The picture was adopted from [16].

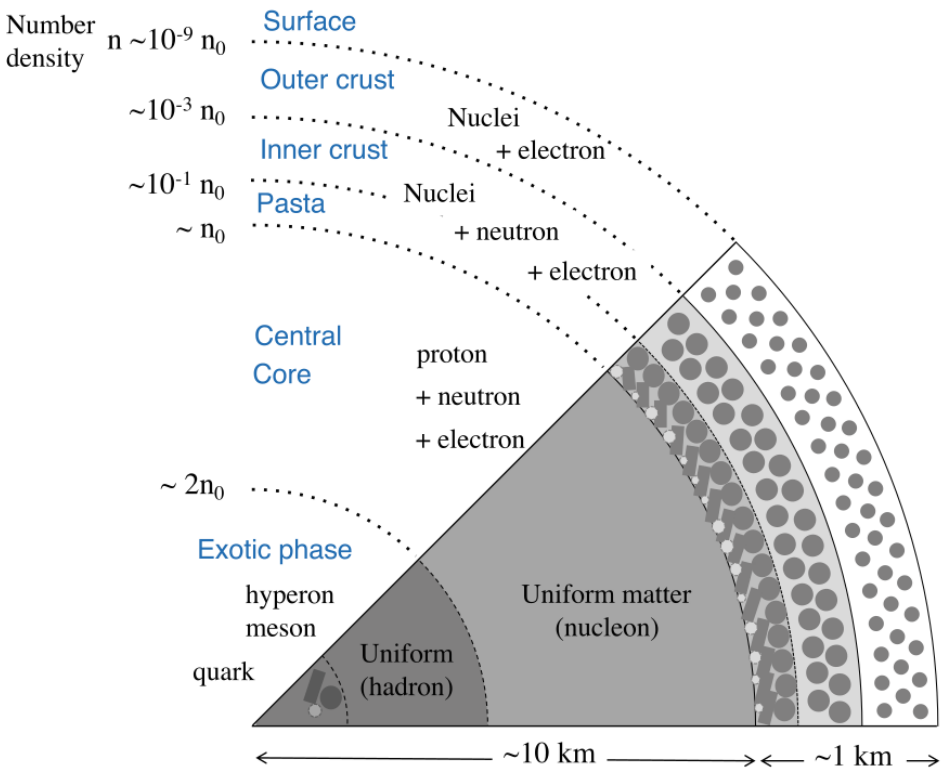

Figure 2: Schematic sketch of the inner structure and different layers of a NS. The picture was taken from [15].

1.1.2 Structure of a Neutron Star

When the NS reaches its final compact size after the cooling process, it remains in an equilibrium state between the pressure of the neutron-rich matter and the gravitational force. From the surface to the inner core the density rises from $\sim 10^{-10} n_0$ to several times n_0 as illustrated in Fig. 2. At the surface, matter consists of stable nuclei e.g. ^{56}Fe as the most stable one, and becomes more neutron-rich at densities around $10^{-8} n_0$ (Outer crust). A further compression at around $10^{-2} n_0$ leads to nonspherical 3D, 2D and 1D shapes of the nuclei which is called pasta structure. In the central core (see Fig. 2) with densities between one and two times n_0, we expect to find uniform matter with free neutrons, protons and electrons. When the density overcomes $n > 2n_0$ in the very inner part of the NS core, there might be an exotic phase with new degrees of freedom in terms of hyperons and quarks. The appearance of these particles could modify the global properties of a NS such as its maximum mass and therefore its mass-radius relation.

1.1.3 Tolman-Oppenheimer-Volkoff Equation

A first estimate of the NS mass-radius-relation can be done by using the so-called Tolman-Oppenheimer-Volkoff equation [20]. This equation defines the pressure gradient of a spherically symmetric body that is in gravitational equilibrium:

$$\frac{dP(r)}{dr} = -\frac{GM(r)n(r)}{r^2}\left(1+\frac{P(r)}{n(r)}\right)\left(1+\frac{4\pi r^3 P(r)}{M(r)}\right)\left(1-\frac{2GM(r)}{r}\right)^{-1} \quad (1)$$

, where $P(r)$ and $n(r)$ are the pressure and density at a given radius r. The mass inside a spherical symmetric volume with radius r can be obtained by:

$$\frac{dM(r)}{dr} = 4\pi r^2 n(r) \quad (2)$$

The first part of Eq. (1) represents the pressure gradient, which is compensated by the classical Newton gravitational force. The last three terms on the right side are corrections according to general relativity.

After setting a central density n_c at $r = 0$ one can integrate over all layers and respective densities, as illustrated in Fig. 2, until the pressure reaches zero (r=R). This defines the total radius of the NS which is then used to calculate its mass using Eq. (2) with $M_{NS} = M(R)$.

For such a calculation n_c, $P(r)$ and $n(r)$ are provided by theories that make predictions on the degrees of freedom in the central exotic phase, on the strength of the corresponding forces and evolution of the different layers. Such a theory is called equation of state. There is a large variety of EOSs with predictions on the mass-radius-relation and on the corresponding maximum NS mass differing over a wide range (see Fig. 1). EOSs which predict a maximum NS mass of less than $2M_\odot$ could be ruled out by the astrophyical observations of e.g. J0740+6620 [19]. The large variation of the predictions of different EOSs in Fig. 1 is owed by the challenge to describe the NS matter in terms of isospin asymmetry and density over a wide range compared to nuclear matter we know from stable or even exotic nuclei we have investigated so far.

1.2 Equation of State of Asymmetric Nuclear Matter

The properties of symmetric nuclear matter at densities around n_0 are quite well investigated and known from experimental results. Whereas the behavior of highly asymmetric or pure neutron matter still remains as an open question in nuclear physics. A common approach to disentangle both the symmetric and asymmetric contribution to the EOS of nuclear matter, is to express the energy per nucleon in a Taylor expansion around the relative neutron-proton asymmetry δ.

$$\delta = \frac{N-Z}{A} \quad (3)$$

Where N, Z and A are the neutron, proton and total nucleon numbers. Even the most exotic heavy nuclei we know are in the range $\delta \lesssim 0.25$, whereas NS matter is highly asymmetric with $\delta \gtrsim 0.8$. The energy per nucleon expanded around $\delta = 0$, which refers to symmetric nuclear matter reads as

$$E(n,\delta) = E(n,0) + \frac{1}{2}\left.\frac{\partial^2 E(n,\delta)}{\partial \delta^2}\right|_{\delta=0} \delta^2 + \mathcal{O}(n^4) \tag{4}$$

Due to the isospin invariance of the nuclear force, only even powers of δ are allowed. The first part on the right side is the energy per nucleon in symmetric nuclear matter. This term can be further expanded around the nuclear saturation density n_0 using the shift parameter $\epsilon = (n - n_0)/3n_0$ which leads to

$$E(n,0) = E(n_0,0) + \frac{1}{2}K_0\epsilon + \mathcal{O}(n^3) \tag{5}$$

The energy per nucleon of symmetric nuclear matter at saturation density is known from experimental data to be $E(n_0,0) \approx -16MeV$. K_0, which is $9n_0^2\partial E(n,0)/\partial n^2$, is the incompressibility parameter and determines the density dependence of $E(n_0,0)$. The value for K_0 can be extracted from experimental data, such as excitations of isoscalar giant monopole resonances, and has been constrained around $K_0 = 223^{+7}_{-8}$MeV [21]. The first derivative of $E(n,0)$, which is the pressure $P(n) = n\partial E(n,0)/\partial n$, vanishes at saturation density. This explains the stability of nuclei at constant density and that densities greater than n_0 can just be achieved with external pressure. In the case of NS matter the gravitational force induces this external pressure.
The second term on the left side of Eq. (4) is called the asymmetry term. With

$$S(n) = \frac{1}{2}\left.\frac{\partial^2 E(n,\delta)}{\partial \delta^2}\right|_{\delta=0} \tag{6}$$

which is called the symmetry energy, Eq. (4) reads as

$$E(n,\delta) = E(n,0) + S(n)\delta^2 + \mathcal{O}(n^4) \tag{7}$$

The general definition of the symmetry energy is the energy cost to convert symmetric nuclear matter into pure neutron matter and is density dependent. Due to a small value of the asymmetry parameter δ, even for neutron-rich isotopes ($\delta \sim 0.25$), higher orders ($\mathcal{O}(n^4)$) of the symmetry energy just give a small contribution to the total energy of a nucleus. Therefore, $S(n)$ is commonly approximated with the symmetry energy. The density dependence of this quantity has to be constrained very precisely in nuclear experiments since deviation will lead to significant uncertainties for predictions on the NS properties, such as radius or cooling pathways by neutrino emission, due to the high isospin asymmetry ($\delta \gtrsim 0.8$) of NS matter [22].

The symmetry energy near the nuclear saturation density expressed in the same manner as Eq. (5) is

$$S(n) = J + L\epsilon + \frac{1}{2}K_{sym}\epsilon^2 + \mathcal{O}(\epsilon^3) \tag{8}$$

with

$$\begin{aligned} J &= S(n_0), \\ L &= 3n_0 \left.\frac{\partial S(n)}{\partial n}\right|_{n=n_0}, and \\ K_{sym} &= 9n_0^2 \left.\frac{\partial^2 S(n)}{\partial n^2}\right|_{n=n_0} \end{aligned} \tag{9}$$

, where J is the symmetry energy at saturation density n_0, L is the slope parameter and K_{sym} is the curvature parameter.

The parameter J is constrained between 30 and 35 MeV, which is compatible with theoretical predictions [14, 23]. For L and K_{sym} the situation is not so clear. Experimental constraints for K_{sym} are limited [14] and the contribution to the symmetry energy near saturation density is small due to the quadratic dependence on the asymmetry ϵ. Whereas the slope parameter L is the dominating factor which mainly defines the pressure P_0 of neutron matter at n_0 via $L = 3P_0/n_0$. The pressure P_0 represents the dominant contribution of the baryons pressure in the NS central core region around n_0 (see Fig. 2) and therefore has a huge influence on the NS radius. Hence the slope parameter L at saturation density represents an essential link between our understanding of nuclear matter and the interpretation of astrophysical observation on the global properties of NS. A precise determination of this parameter requires a strong synergy of both, theoretical and experimental efforts.

1.3 Constraining the Symmetry Energy Parameters

The determination of the symmetry energy and its parameters requires on the one hand a theoretical model which can precisely reproduce the bulk properties of finite neutron-rich nuclear matter. On the other hand, experimental observables accessible in the laboratory are needed which are linked to these predictions and could be used to validate the theoretical model.

Theoretical models to describe the nuclear structure are ranging from ab initio models which are capable to treat two- or three-body interactions explicitly, up to fully macroscopic descriptions such as the liquid drop model. For a description of finite neutron matter, it turned out that the balance between both extremes is the best choice. So-called self-consistent mean-field models represent an approach allowing to investigate a wide mass range of different isotopes and dense matter on the basis of effective

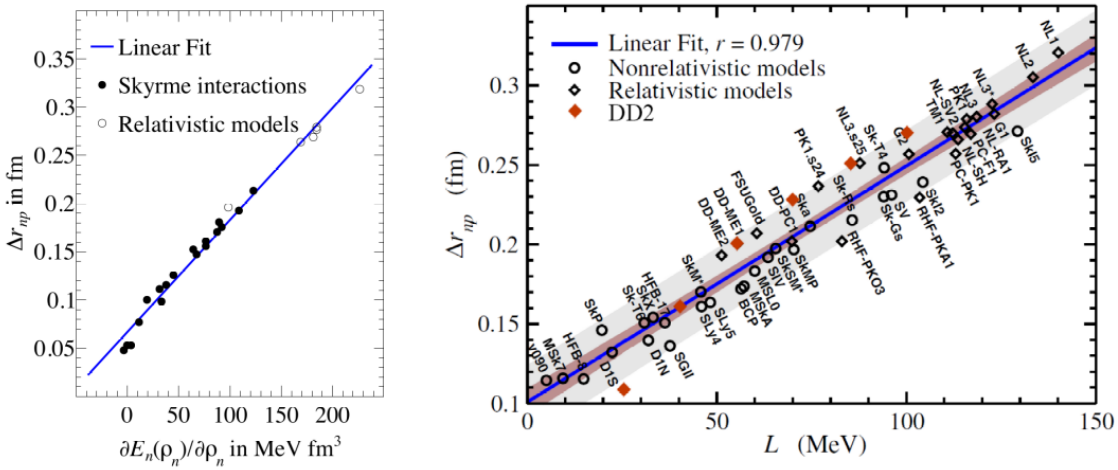

Figure 3: Left panel: The derivative of the the EOS at n = 0.1/fm^3 versus the neutron-skin thickness of ^{208}Pb for different Skyrme interactions (closed symbols) [24] and relativistic models (open symbols) [25]. Right panel: Neutron-skin thickness of ^{208}Pb versus the slope parameter L calculated with different relativistic and non-relativistic models [5] [26]

energy density functionals such as Skyrme and Gogny interactions. In this models, the nucleon-nucleon interaction is used to solve many-body problems on a mean-field level. A detailed discussion of these models is beyond the scope of this work and can be found in [27, 28].

The different models are used to make predictions on the symmetry energy and its parameters, which cover a wide range of the energy density, depending on the used interaction. This variation on the predicted symmetry energy values and their effect on the EOS or mass-radius-relation is illustrated in Fig. 1 by the different mass-radius-curves.

Despite this large variation, it turned out that all interactions are showing a linear correlation between their prediction of the symmetry energy or its slope parameter and the neutron-skin thickness. This correlation was first published by Brown [24] who calculated the neutron-skin thickness and the derivative of the neutron EOS at n = 0.1/fm^3 for ^{208}Pb. The left panel of Fig. 3 illustrates the correlation of both quantities for different Skyrme interactions (closed symbols) [24] and relativistic models (open symbols) [25]. Later Roca-Maza et al. showed the same linear correlation of the neutron-skin thickness on the symmetry energy slope parameter for different relativistic and non-relativistic models in case of ^{208}Pb (Right panel of Fig. 3). This means that with a precise measurement of the neutron-skin thickness it is possible to constrain the value of the symmetry energy or its slope parameter near nuclear saturation density. Hence

the neutron-skin thickness presents an ideal experimental observable to test theoretical models and to define precisely the range of predicted values for the symmetry energy.

1.4 The Neutron-Skin Thickness of Exotic Nuclei

The formation of a neutron skin in exotic nuclei can be understood by reviewing the dynamical structure proposed by the shell model. The quantum mechanical description of the nucleus interaction potential together with a spin-orbit coupling leads to discrete energy levels which are called shells. According to Pauli exclusion principle, these shells can be occupied by a limited amount of nucleons. This results in shell closures similar to electron shells in atomic physics. The number of protons(neutrons) that lead to a closed shell is called magic proton(neutron) number. An important feature of isotopes with magic nucleon numbers is the increase of the corresponding nucleon separation energy.

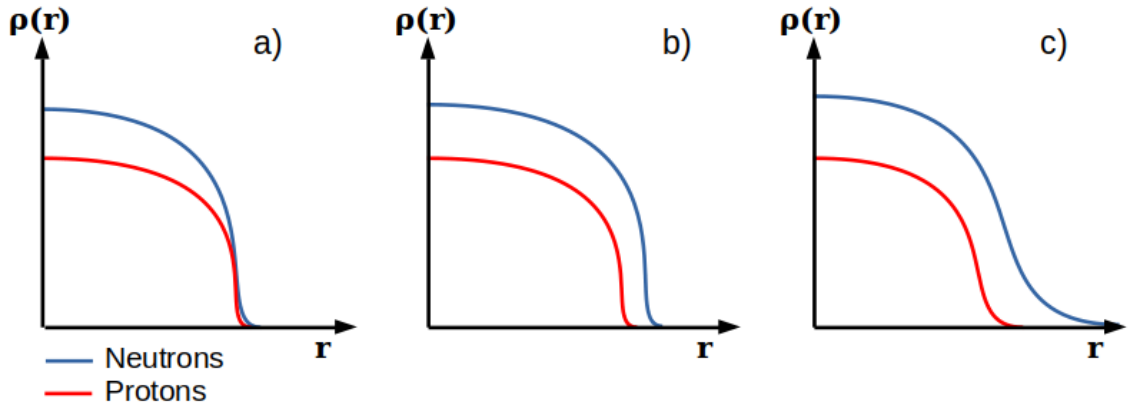

Figure 4: Evolution of the proton (blue) and neutron (red) density distribution from β-stable nuclei (a), neutron-rich nuclei (b) and neutron-rich nuclei which are reaching the neutron-drip-line (c).

For β-stable nuclei the neutron and proton separation energy are similar around 10 MeV over a wide range of the nuclear chart. Especially the radial distributions of neutrons and protons, mainly expressed by the root mean square radius $\langle r^2_{n/p}\rangle^{1/2}$, have a similar cut off and densities are just scaled by the number of available nucleons of each species (panel a) in Fig. 4). This originates in a classical picture dominantly from the balance of asymmetry and coulomb energy. By getting more and more neutron-rich the neutron separation energy decreases and the neutron exceeds the proton density distribution (panel b) in Fig. 4). The difference between the neutron and proton density distribution is defined as the neutron skin with:

$$\Delta r_{np} = \langle r^2_n\rangle^{1/2} - \langle r^2_p\rangle^{1/2} \tag{10}$$

The increase of the proton separation energy with growing neutron excess is caused by an increase of the pairing strength as discussed in [29]. If the neutron separation energy reaches zero the neutron wave function evolves a tail outside of the potential due to quantum tunneling. This gives a non-zero probability for neutrons to be located far away from the core and a neutron halo can be formed (panel c in Fig. 4). Such a highly spatial extended matter radius was first discovered in the pioneering experiments of Tanihata et al. in the mid-1980s at LBNL [30]. By measuring the total interaction cross-section of different light isotopes they found a strong increase in the reaction probability for the neutron-rich isotope ^{11}Li. This effect was then interpreted by Jonson and Hansen as a result of a large matter radius of a ^{9}Li core with 2 valence neutrons forming a halo [31]. This discovery was the beginning of a new era of nuclear physics experiments and established total reaction or fragmentation measurements as a tool to probe the nucleus distribution.

There is currently a high experimental efford to measure the neutron-skin thickness of exotic nuclei precisely. Consequently, also many different experimental techniques are proposed which either probe the matter or neutron density distribution or are directly sensitive to the neutron-skin thickness. An example of a experimental probe of the density dependence of the symmetry energy near saturation density is the electric dipole response of exotic nuclei [3]. Another promising proposal for a precise determination of the neutron-skin thickness is the measurement of the parity-violating asymmetry in polarized electron scattering with the Parity Radius Experiment (PREX) at Jefferson Lab [4]. It is not the intention of this work to compare and quantify the applicability of the different techniques.

The following chapter concentrates on a similar approach that was discussed above and which led to the discovery of halo nuclei, namely the measurement of total reaction cross-sections.

1.5 Total Reaction Cross Section

The experiments by Tanihata et al already proved that the reaction cross-section is sensitive to the total nucleon density distribution. Since this time, reaction cross-section measurements have been widely carried out to investigate the density distribution of stable and exotic nuclei at radioactive ion beam facilities at intermediate [32, 33, 34] or at relativistic energies, e.g., at the GSI facility [35, 36, 37].

In order to understand the sensitivity of reactions on the nucleon distribution it is helpful to use a simplified picture of the target and projectile and consider them as spheres with radius $r_{t/p}$ in a reaction plane. Both radii represent the spatial distribution of the whole nucleus according to an envelope of the density distributions illustrated in

Fig. 4. If both spheres are overlapping in a collision, there is a certain probability for a reaction. This probability is isospin and energy-dependent, which will be discussed in more detail in Chapter 2. Therefore, it is necessary to distinguish between a proton- and a neutron-radius for both the target and projectile. If the proton distribution of the projectile overlaps with the target distribution, a projectile proton could react either react with a target proton or a neutron. Such a reaction could lead to a knock-out of a proton which is then called charge-changing reaction $\sigma_{\Delta Z}$. The same situation can now be considered with a projectile neutron which could lead to a neutron-removal reaction $\sigma_{\Delta N}$. The sum of both reaction probabilities is called interaction cross-section σ_I and represents the probability that the projectile changes its identity during a reaction.
Beside those nucleon removal reactions, the projectile could elastically traverse the target without changing its internal degrees of freedom (σ_{el}) or can be inelastically excited to a bound state (σ_{inel}). Especially the later one is the dominant reaction mechanism at low beam energies ($E_{Beam} < 200$MeV/nucleon) and decreases at higher energies. The sum of the inelastic and interaction cross section is called reaction cross section σ_R. Additional identification of the elastic contribution gives the total cross section σ_T. Table 1 gives a summary of the different discussed cross sections and their relation to each other.

Total Elastic Cross Section	σ_{el}
Total Inelastic Cross Section	σ_{inel}
Total Charge-Changing Cross Section	$\sigma_{\Delta Z}$
Total Neutron-Removal Cross Section	$\sigma_{\Delta N}$
Total Interaction Cross Section	$\sigma_I = \sigma_{\Delta Z} + \sigma_{\Delta N}$
Total Reaction Cross Section	$\sigma_R = \sigma_I + \sigma_{inel}$
Total Cross Section	$\sigma_T = \sigma_R + \sigma_{el}$

Table 1: Summary of the different integrated cross-section.

From this definition, it becomes clear that especially the total neutron-removal cross-section is sensitive on the radial distribution of neutrons, or matter radius, of the projectile. A measurement of this quantity with exotic beams at relativistic energies together with a precise determination of the charge radius was proposed to be an ideal

candidate to determine the neutron-skin thickness [38, 39]. In contrast, there are several experimental techniques to measure the charge radius of nuclei very precisely. The most precise measurements are achieved via electron scattering or laser-spectroscopy. A basic overview of the different experimental techniques can be found in [40].
For the direct measurement of the neutron distribution these electromagnetic probes cannot be used as there is no first order effect from neutral particles. But, as discussed above, the strong interaction allows for a rather direct measurement. Precisely measured total reaction or interaction cross-sections are compared with theoretical predictions in order to determine a density distribution of the nucleus. In the case of these integrated cross sections a common theoretical approach is the Glauber reaction model. In the following, the basic assumptions of the Glauber model are discussed. A detailed deduction and discussion of this framework is presented in Chapter 2.

1.6 Concept and Outline of this Thesis

The Glauber model starts with a quantum mechanical description of the scattering process and introduces approximations based on a geometrical treatment of the whole system. Therefore the resulting equations are denoted to be neither purely quantum mechanical nor purely classical, they are semiclassical. With this ansatz, the scattering amplitude and thus the integrated cross section can be expressed in terms of the so-called impact parameter, which is the offset between the projectile and target nucleus center, and depends mainly on three inputs quantities. The first two are the already discussed projectile and target density distribution. The third input is the isospin and energy-dependent nucleon-nucleon interaction probability. This probability is included via the free proton-proton (neutron-neutron) and proton-neutron interaction cross-section which is available from experimental data over a wide energy range. An integral over the impact parameter gives an interpolation from the nucleon-nucleon to a nucleus-nucleus cross-section. However, since the input reaction probability refers to a free proton or neutron, several in-medium effects, such as Pauli blocking or Coulomb effects, have to be considered in order to obtain a realistic description of the reaction mechanism. Before the model can be used to reproduce the measured cross sections of exotic nuclei by adjusting the projectile density distribution, it is essential to test the introduced in-medium corrections under stable conditions. For this purpose ^{12}C as projectile and target nucleus represents the perfect test case. Since ^{12}C is stable, the charge radius of ^{12}C was extensively investigated and is well-known. With a symmetric proton and neutron number and a relatively small contribution from the coulomb interaction, the matter and charge radius of ^{12}C can be considered to be the same.
A measurement of the energy-dependent total interaction cross-section of a ^{12}C beam

on a ^{12}C target at relativistic energies was performed during the FAIR Phase-0 campaign of the R^{3}B collaboration at the GSI/FAIR facility. The measurement was carried out with initial beam energies of 400, 550, 650, 800 and 1000 MeV/nucleon. In this energy regime are currently just three data points available covered by relatively large error bars. Goal of this work was to provide a larger data set at the precision level of $\Delta\sigma_I < 0.1\%$, including statistical and systematic error contributions.

The structure of the present thesis is outlined in the following. Chapter 2 starts with a brief overview of the Glauber framework for total reaction cross sections, based on a quantum mechanical description of a scattering process and making use of eikonal wave functions and an optical potential. Inputs for the cross section calculations are the free nucleon-nucleon cross section and nuclear density distributions, which are discussed in Section 2.2. So-called in-medium modifications for the cross section calculation, as introduced in [41, 42], are briefly summarized in Section 2.3.

Chapter 3 provides a brief discussion of experimental challenges and requirements for a precise measurement of absolute cross sections, followed by a introduction of the GSI/FAIR facility and the R^{3}B experimental setup.

Experimental quantities and the corresponding analysis methods and systematic uncertainties are discussed in Chapter 4.

The experimentally obtained total interaction cross sections of ^{12}C+^{12}C collisions for the different beam and target combinations are presented and discussed in Chapter 5. A summary and conclusion is provided in Chapter 6.

2 The Glauber Model

The term Glauber Model is ascribed to the initial work of Roy J. Glauber in the 1950s. In his summarizing lectures on theoretical physics from 1959 [43], Glauber introduced the use of eikonal wave functions to describe nuclear scattering reactions at high energies. The basic expression for total reaction cross sections presented by Glauber relies on a simple geometrical treatment of the reaction process [44].

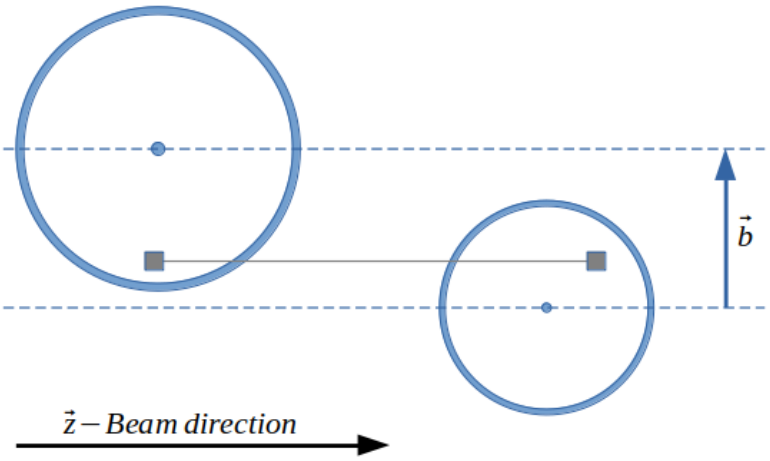

Figure 5: A simplified geometrical illustration of a nucleus-nucleus collision.

In this picture, the projectile and target nucleus are simplified and assumed to be homogenous spheres (see Fig. 5). The offset between both sphere centers is the impact parameter $\vec{b}$. This classical approach and a quantum mechanical description of the scattering process lead to the semiclassical denotation of the model. Depending on the purpose of the calculation, there are different ways to express integrated cross sections in the Glauber framework. The more classical one called the "Probability Approach," starts with the definition of a so-called "thickness function". This quantity can be derived from Fig. 5 by defining the overlap of a projectile and target nucleon. Hence, it has to contain information about the density profile of both. The probability for a reaction in this overlap area is introduced by the free nucleon-nucleon cross section. In the last step, a combinatorial factor is used to consider the whole nucleus. This approach is descriptive and detailed discussed in "Introduction to Nuclear Reactions" by Carlos Bertulani and Pawel Danielewicz [45] and was summarized in the Ph.D. Thesis of Fabia Schindler [46].

The discussion in this Chapter will concentrate on the second approach to describe reaction cross sections in the Glauber framework. Here, one starts with the quantum

mechanical description of a scattering process, followed by several approximations. A short de Broglie wavelength of the projectile compared to the interaction range of the scattering potential allows to solve the Schrödinger equation using an eikonal wave function. This approximation restricts the calculation to energies above $\sim 100MeV$ and, therefore short interaction times. But it also reduces the potential to a single integral along the beam direction. This reflects the geometrical picture of the projectile passing the target on a straight line until the interaction occurs. In an explicit calculation of a nucleus-nucleus collision, the interaction between every nucleon of the projectile and the target must be considered. Such an expensive calculation can be simplified with an averaged interaction based on a $t\rho\rho$ approximation. This approximation is called optical limit representation and makes use of an optical potential where the interaction is expressed in terms of the free nucleon-nucleon cross section and the projectile and target density distribution. On the one hand, the optical potential reduces the reaction information, e.g., on specific final states or secondary reactions. However, since this work concentrates on an integrated cross section, detailed information on the final state is not needed, and this approximation is considered to be valid.
Section 2.1 provides a detailed derivation of total reaction cross sections in the discussed framework. The discussion is strongly orientated to the work of Carlos Bertunlani/Pawel Danielewicz [45] and the summary of Fabia Schindler [46]. The preliminary result will only depend on the free nucleon-nucleon cross section and the projectile and target density distribution. Both will be discussed in more detail in Section 2.2. For a realistic interpolation of the free nucleon-nucleon to a nucleus-nucleus cross section, it is imperative to introduce several in-medium corrections (Section 2.3). The final results of such a realistic model calculation of total interaction cross sections for the ^{12}C+^{12}C system, as published in [42] and provided by Carlos Bertulani [47], are presented in Section 2.4.

2.1 Reaction Cross Sections in the Glauber Model

2.1.1 Scattering in Quantum Mechanics

The discussion of scattering of incoming plane waves from a short-range potential $V(\vec{r})$ in quantum mechanics starts with the time-independent Schrödinger equation:

$$H\psi_{\vec{k}}(\vec{r}) = E\psi_{\vec{k}}(\vec{r}), \tag{11}$$

where the Hamiltonian is defined as

$$H = -\frac{\hbar^2}{2\mu}\vec{\nabla}^2 + V(\vec{r}) \tag{12}$$

The stationary state $\psi_{\vec{k}}(\vec{r})$ is a solution of Eq. (11) where k denotes the wave number. Due to the distortion of the incoming plane wave by the scatterer, it can be written as

$$\psi_{\vec{k}}(\vec{r}) = \phi_{\vec{k}}(\vec{r}) + \psi^{sc}_{\vec{k}}(\vec{r}), \tag{13}$$

where $\phi_{\vec{k}}(\vec{r})$ is the incoming plane wave and $\psi^{sc}_{\vec{k}}(\vec{r})$ is the outgoing spherical wave, with an asymptotic behavior near the detector ($r \to \infty$)

$$\psi^{sc}_{\vec{k}}(\vec{r}) \to f(\Omega)\frac{e^{ikr}}{r} \tag{14}$$

The introduced $f(\Omega)$ is the so-called scattering amplitude, which describes the orientation dependence of the strength of the outgoing spherical wave. By assuming a central potential, the angular dependence of the scattering amplitude is reduced to $f(\Omega) = f(\theta)$. The $1/r$ dependence ensures the conservation of the particle flux within the spherical surface. With this asymptotic behavior, Eq. (13) can be written as:

$$\psi_{\vec{k}}(\vec{r}) \to A\left(e^{i\vec{k}\vec{r}} + f(\theta)\frac{e^{ikr}}{r}\right), \tag{15}$$

where A denotes a normalization constant. To find an expression for the scattering amplitude that describes the transition of the incoming plane wave to the outgoing, it is common to solve the Lippmann-Schwinger equation:

$$|\psi_{\vec{k}}\rangle = |\phi_{\vec{k}}\rangle + G_0(E)V(\vec{r})|\phi_{\vec{k}}\rangle \tag{16}$$

Here $G_0(E)$ is the Green's operator. The asymptotic solution of Eq. (16) is ([45] Sec. 3.3, Eq. (3.45))

$$\psi^{sc}_{\vec{k}}(\vec{r}) = \frac{1}{(2\pi)^{3/2}}\left[e^{i\vec{k}\vec{r}} + \frac{e^{ikr}}{r}\left(-2\pi^2\left(\frac{2\mu}{\hbar^2}\right)\langle\phi_{\vec{k}'}|V(\vec{r})|\psi_{\vec{k}}\rangle\right)\right] \tag{17}$$

By comparing Eq. (15) and Eq. (17) the normalization factor A is

$$A = \frac{1}{(2\pi)^{3/2}} \tag{18}$$

and the scattering amplitude can be written as

$$\begin{aligned} f(\theta) &= -2\pi^2\left(\frac{2\mu}{\hbar^2}\right)\langle\phi_{\vec{k}'}|V(\vec{r})|\psi_{\vec{k}}\rangle \\ &= -2\pi^2\left(\frac{2\mu}{\hbar^2}\right)\int \phi^*_{\vec{k}'}(\vec{r})V(\vec{r})\psi_{\vec{k}}(\vec{r})d\vec{r} \end{aligned} \tag{19}$$

The transition of the initial state $\psi_{\vec{k}}$ to final state $\phi_{\vec{k}'}$ is now expressed by the matrix element of the potential in Eq. (19). The observation angle θ corresponds to the angle between the initial and final wave vectors k and k', respectively.

The differential elastic cross section is defined as the absolute square value of the scattering amplitude:

$$\frac{d\sigma_{el}}{d\Omega} = |f(\theta)|^2 \tag{20}$$

From this definition, the total elastic cross section is

$$\sigma_{el} = \int d\Omega |f(\theta)|^2 \tag{21}$$

The optical theorem finally relates the total cross section with the imaginary part of the scattering amplitude at zero degrees ($\theta = 0$)

$$\sigma_T = \frac{4\pi}{k} \operatorname{Im}[f(\theta = 0)] \tag{22}$$

2.1.2 Eikonal Wave Function

The eikonal approximation is used to define the wave function of the incoming particle and the distorted outgoing wave function. The main assumption of the eikonal approximation is that the projectile passes the target on a straight line. As a consequence of this picture, the interaction range a of the target potential has to be large compared to the projectile wavelength

$$ka = 2\pi \frac{a}{\lambda} \gg 1 \tag{23}$$

Equivalent the energy $E = \frac{k^2\hbar^2}{2\mu}$ has to be much larger than the potential depth

$$E \gg |V_0| \tag{24}$$

which is valid for a projectile substantially energy larger than 40-50 MeV.
These assumptions are used in the following to simplify the solution of the Schrödinger equation (Eq. (11)) in spherical coordinates $\vec{r} = (\vec{c}, z)$. As shown previously the solution $\psi_{\vec{k}}(\vec{r})$ is an incoming plane wave e^{ikz} which gets distorted $\phi(\vec{c}, z)$ by the scattering potential

$$\psi_{\vec{k}}(\vec{r}) = e^{ikz}\phi(\vec{c}, z) \tag{25}$$

With this ansatz Eq. (11) becomes

$$e^{ikz}\vec{\nabla}^2_{\vec{c}}\phi(\vec{c}, z) + 2ike^{ikz}\frac{\partial\phi(\vec{c}, z)}{\partial z} + e^{ikz}\frac{\partial^2\phi(\vec{c}, z)}{\partial z^2} - \frac{2\mu}{\hbar^2}V(\vec{r})e^{ikz}\phi(\vec{c}, z) = 0 \tag{26}$$

The approximation of a large interaction range and, therefore, slowly varying potential leads consequently to a slowly varying distortion. This simplifies Eq. (26) since the first and third term can be neglected and results in

$$\frac{\partial\phi(\vec{r})}{\partial z} + \frac{i}{\hbar\nu}V(\vec{r})\phi(\vec{r}) = 0 \tag{27}$$

where $\nu = \hbar k/\mu$. The solution of this first-order differential equation is (see [45] Sec. 8.4, Eq. (8.66))

$$\phi(\vec{c}, z) = exp\left\{-\frac{i}{\hbar\nu}\int_{-\infty}^{z} V(\vec{c}, z')dz'\right\} \tag{28}$$

and the eikonal wave function can now be written as

$$\psi_{\vec{k}}(\vec{r}) = e^{ikz+i\chi(\vec{c},z)} \tag{29}$$

where $\chi(\vec{c}, z)$ is the so-called eikonal phase

$$\chi(\vec{c}, z) = -\frac{1}{\hbar\nu}\int_{-\infty}^{z} V(\vec{c}, z')dz' \tag{30}$$

The eikonal wave function is a solution for the outgoing distorted wave. Both the incoming plane wave and the outgoing eikonal wave can now be used to express the scattering amplitude in Eq. (14) as

$$\begin{aligned} f(\theta) &= -2\pi^2\left(\frac{2\mu}{\hbar^2}\right)\left(\frac{1}{(2\pi)^{3/2}}\right)^2\int e^{-i\vec{k}'\vec{r}}V(\vec{r})e^{i\vec{k}\vec{r}}e^{i\chi(\vec{r})}d\vec{r} \\ &= -\frac{1}{4\pi}\left(\frac{2\mu}{\hbar^2}\right)\int e^{i(\vec{k}-\vec{k}')\vec{r}}V(\vec{r})e^{i\chi(\vec{r})}d\vec{r} \\ &= -\frac{1}{4\pi}\left(\frac{2\mu}{\hbar^2}\right)\int d\vec{c}e^{i\vec{q}\vec{c}}\int_{-\infty}^{+\infty} dzV(\vec{c}, z)e^{i\chi(\vec{c},z)} \end{aligned} \tag{31}$$

From line 2 to line 3 in the equation above, the wave vector difference $(\vec{k} - \vec{k}')\vec{r}$ was substituted by the momentum transfer $\vec{q}\vec{c}$. This is possible since in the high energy regime of the eikonal approximation the scattering process is restricted to small angels and $\vec{k}' \approx \vec{k}$. After some more substitution (Eq. 2.55 - 2.66 in [46]), the eikonal phase can be used to express the scattering amplitude as

$$f(\theta) = -\frac{ik}{2\pi}\int d\vec{c}e^{i\vec{q}\vec{c}}(e^{i\chi(\vec{c})} - 1) \tag{32}$$

Inserting this expression into Eq. (21) and Eq. (22) gives the total elastic cross section

$$\sigma_{el} = \int \left|e^{i\chi(\vec{c})} - 1\right|^2 d\vec{c} \tag{33}$$

and total cross section in the eikonal approximation

$$\sigma_T = 2\int \left(1 - Re\left[e^{i\chi(\vec{c})}\right]\right) d\vec{c} \tag{34}$$

According to the definition in Section 1.5, the total cross section is the sum of the total elastic and total reaction cross sections. Hence, the total reaction cross section in the eikonal approximation read as

$$\sigma_R = \int \left(1 - \left|e^{i\chi(\vec{c})}\right|^2\right) d\vec{c} \tag{35}$$

or

$$\sigma_R = \int \left(1 - |S(\vec{c})|^2\right) d\vec{c} \tag{36}$$

where $S(\vec{c})$ is the eikonal elastic S-matrix element [44]. The interaction potential V and, therefore, the eikonal phase χ are complex, where the imaginary part describes the absorptive nature. From Eq. (35) and Eq. (36), it becomes clear that the total reaction cross section just depends on the imaginary part of the potential. The next chapter will discuss how such a complex potential is defined.

2.1.3 The optical limit in the Glauber Model

A common expression of the potential for nuclear reactions in the Glauber framework is an optical potential. For the study of total reaction cross sections, the Coulomb contribution to the potential is neglected. The simplest version of such a potential can be obtained with the so-called $t\rho\rho$-approximation[45]. The discussion starts with single nucleon-nucleus interaction, which is folded with the single particle densities of the proton and neutron ($t\rho$). In a second step, this definition is interpolated to nucleus-nucleus interaction[48]. For the reaction of a projectile proton with a target nucleon, the potential reads as

$$V_{opt} = \langle t_{pn} \rangle \rho_n(\vec{r}) + \langle t_{pp} \rangle \rho_p(\vec{r}) \tag{37}$$

In this approximation, the nucleon-nucleon interaction is expressed by the transition matrix element $\langle t_{pn} \rangle / \langle t_{pp} \rangle$. Using Eq. (19), the transition matrix element for small scattering angles can be written as

$$t_{pi}(\theta \approx 0) = -\frac{2\pi\hbar^2}{\mu} f_{pi}(\theta \approx 0) = -\frac{\hbar\nu}{2} \sigma_{pi}(\alpha_{pi} + i) \tag{38}$$

where σ_{pi} is the total proton nucleon cross section (see Eq. (22)). Since the scattering amplitude is complex, the last term of Eq. (38) can be expressed in terms of the ratio (α_{pi}) of the real and imaginary part of $f_{pi}(\theta = 0)$. With this definition the optical potential (Eq. (37)) can be written as

$$V_{opt}(\vec{r}) = \left(-\frac{\hbar\nu}{2}(\sigma_{pn}\alpha_{pn}\rho_n(\vec{r}) + \sigma_{pp}\alpha_{pp}\rho_p(\vec{r}))\right) + i\left(-\frac{\hbar\nu}{2}(\sigma_{pn}\rho_n(\vec{r}) + \sigma_{pp}\rho_p(\vec{r}))\right) \tag{39}$$

The total reaction cross section depends on the absolute square value of the eikonal elastic S-matrix element (see Eq. (35) and Eq. (36))

$$|S(\vec{c})|^2 = \left|e^{i\chi(\vec{c})}\right|^2 = exp\left(\frac{2}{\hbar\nu}\int_{-\infty}^{+\infty} Im\left[V_{opt}(\vec{r})\right] dz'\right) \tag{40}$$

$$= exp\left(\int_{-\infty}^{+\infty} (-\sigma_{pn}\rho_n(\vec{r}) - \sigma_{pp}\rho_p(\vec{r}))dz'\right) \tag{41}$$

With this expression, it becomes clear that in the case of total reaction cross sections, just the imaginary part of the potential contributes. The optical potential for this specific case can be written as

$$V_{opt}(\vec{r})^R = iIm[V_{opt}] = -i\frac{\hbar\nu}{2}(\sigma_{pn}\rho_n(\vec{r}) + \sigma_{pp}\rho_p(\vec{r})) \tag{42}$$

The only inputs are the free nucleon-nucleon cross sections and the single particle densities. By replacing the projectile proton with a nucleus, Eq. (42) has to be extended to a nucleus-nucleus potential. Therefore, the single proton-nucleon interaction is replaced by an isospin-averaged transition matrix element [45, 46]

$$t_{NN} = -i\frac{\hbar\nu}{2}\left[\frac{Z_P N_T + Z_T N_P}{A_P A_T}\sigma_{pn} + \frac{Z_P N_T + N_P N_T}{A_P A_T}\sigma_{pp}\right] \tag{43}$$

$$= -i\frac{\hbar\nu}{2}\sigma_{NN}, \tag{44}$$

where A, N, and Z are the mass, neutron, and proton numbers of the target (T) and projectile (P), respectively.
Additionally, the single particle densities in Eq. (42) are replaced by an integral over the ground state nuclear densities of the target $\rho_T(\vec{r})$ and projectile $\rho_P(\vec{r})$. With these extensions, the optical potential for a nuclear nucleon-nucleon interaction can be written as

$$V_{OL}(\vec{r}) = -i\frac{\hbar\nu}{2}\sigma_{NN}\int d\vec{r}\rho_P(\vec{r})\rho_T(\vec{r}-\vec{b}) \tag{45}$$

And the total reaction cross section (Eq. (36)) becomes

$$\sigma_R = 2\pi\int d\vec{b}\left(1 - exp\left(-\sigma_{NN}\int d\vec{z}'\int d\vec{r}\rho_P(\vec{r})\rho_T(\vec{r}-\vec{b})\right)\right) \tag{46}$$

In this representation, σ_R just depends on the projectile and target density distribution and the averaged free nucleon-nucleon cross section. The latter mainly defines the energy-dependent trend of the reaction cross section. In comparison, the nucleon density distribution gives rise to the absolute magnitude of the reaction probability. Both will be discussed in the following chapters in more detail.

2.2 Input for the Glauber Model

2.2.1 The free Nucleon-Nucleon Cross-Section

As presented in the last section, the discussion of a theoretical expression for a nucleus-nucleus reaction started with single nucleon-nucleon interaction and was extended in further steps. In the preliminary expression for the total reaction cross section

(Eq. (46)), σ_{NN} denotes the isospin averaged nucleon-nucleon cross section. To understand the contribution of this parameter to the final cross section σ_R, it is necessary to decompose σ_{NN} again and to examine the free nucleon-nucleon cross sections for proton-proton(neutron-neutron) and neutron-proton interaction separately.
The experimental cross-section data [49] of free proton-proton (red symbols) and neutron-proton (black symbols) nuclear reactions (without Coulomb scattering) are plotted in Fig. 6. Since the nuclear force is charge-independent, the neutron-neutron and proton-proton cross section are assumed to be the same. The red and black lines are fit functions to the experimental data based on a parameterization given in [41], which are used to calculate σ_{NN}.

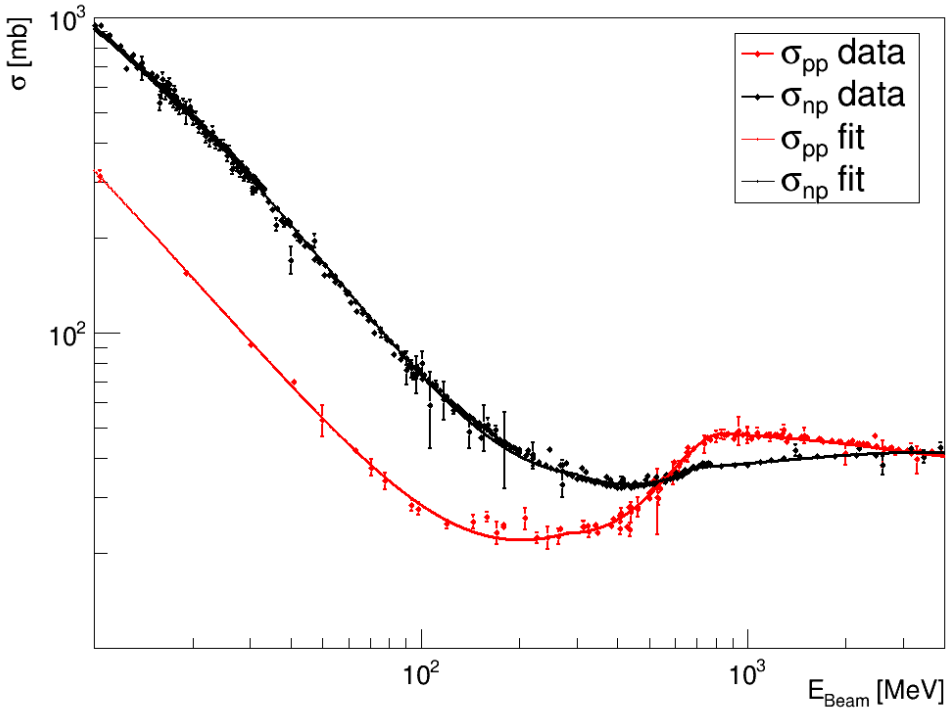

Figure 6: Nuclear cross sections of free proton-proton (red symbols) and neutron-proton (black symbols) reactions [49]. The red and black lines illustrate fits on the experimental data obtained by a parameterization from [41].

Elastic Scattering The dominant process in the energy regime below $\sim 280MeV$ is elastic scattering. As discussed in the previous section, the eikonal approximation is just valid for energies above $\sim 100MeV$. But for completeness, the nucleon-nucleon cross section in the low-energy regime will also be briefly discussed. The cross section decreases with increasing energy for both the pp and np systems. In the case of elastic

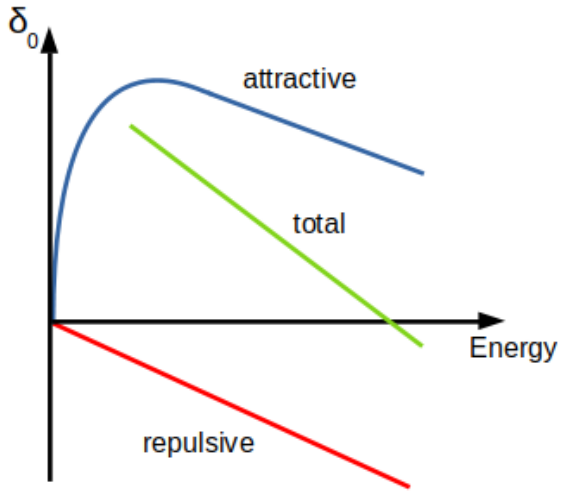

Figure 7: Schematic representation of the positive and negative contribution to the energy-dependent total phase shift caused by a long-range attractive and short-range repulsive part of the nucleon-nucleon potential.

scattering, the scattering amplitude can be described by a partial wave decomposition as

$$f(\theta) = \frac{1}{k}\sum_{l=0}^{\infty}(2l+1)e^{i\delta_l}sin\delta_l P_l(cos\theta) \tag{47}$$

where $k = 1/\lambda$ is the wave number of the scattered nucleon, P_l is an eigenfunction with the angular momentum l of the Legendre polynomials, and δ_l is the phase shift between the incoming and scattered wave. Especially the phase relation defines the energy dependency of the scattering amplitude and, therefore, the elastic cross section (see Eq. (21)). At low energies, the scattering process can be described by a point-like particle as an incoming plane wave scattering on a Yukawa potential. This potential can be decomposed into a long-range attractive and a short-range repulsive part. For low energies (large wavelength), the incoming wave is primarily distorted by the attractive potential, which can be effectively described by a virtual one- or two-pion exchange and results in a positive phase shift. With increasing energy, the repulsive contribution of the potential, described by an exchange of three or more virtual pions and causes a negative phase shift, gets more relevant. When the wavelength of the incoming particle is in the order of effective potential radius, both contributions are of the same order (but different signs), and the phase shift and, therefore, the cross section reaches a minimum. Fig. 7 illustrates the energy dependence of both contributions and the total phase shift for a nucleon-nucleon potential.

For elastic scattering the ratio of σ_{pn} and σ_{pp} (see Fig. 6) varies from $\sim$ 3.3 at $50MeV$ to $\sim$ 1.7 at $200MeV$ (see Fig. 8). A precise analysis of this discrepancy is complicated since several electromagnetic corrections must be considered [50]. A more general explanation can be found in the already mentioned picture, where a virtual pion

exchange mediates the strong force. In the case of proton-proton (neutron-neutron) scattering, just the neutral pion π^0 is exchanged. Whereas in neutron-proton scattering both charged pions, π^+ and π^-, participate.

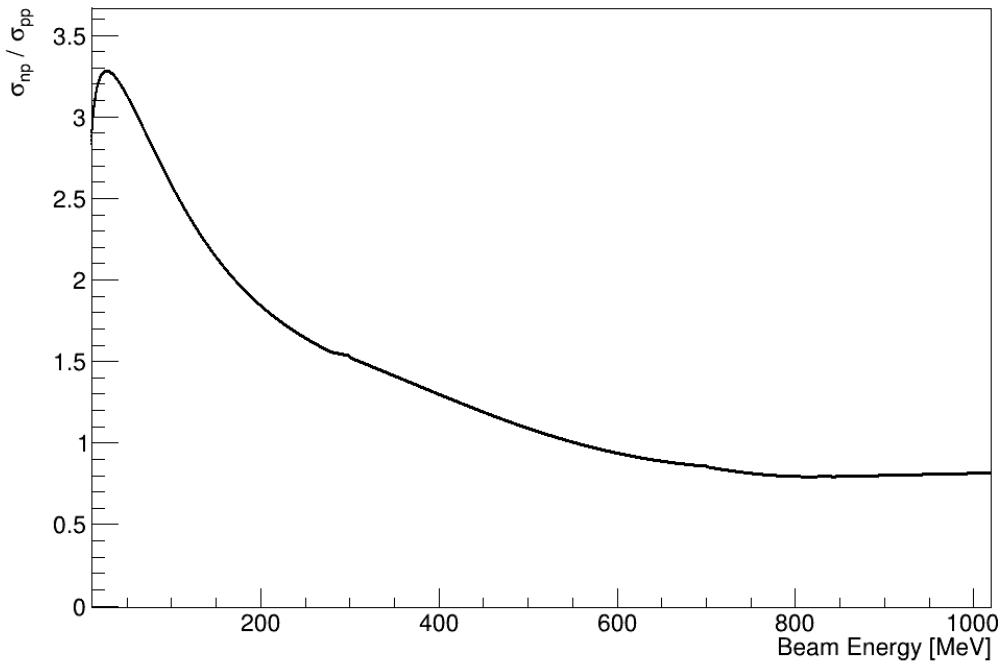

Figure 8: Ratio of the neutron-proton and proton-proton cross section (as given in Fig. 6) versus the beam energy.

Additionally, the different interaction strength is related to the spin-dependence of the nuclear force. A nucleon-nucleon pair's total wave function, consisting of a spin- and an isospin part, has to be anit-symmetric. For the neutron-proton pair, it is not just possible to form a system with parallel spin (triplet) and anti-parallel isospin (singlet), known as the deuterium, and is a bound system. Furthermore, neutrons and protons can also couple to an unbound system with anti-parallel spin (singlet) and parallel isospin (triplet). On the other hand, the two protons (neutrons) can just form a system with parallel isospin (triplet) and anti-parallel spin (singlet) due to the Pauli exclusion principle for identical particles.

Pion Production At beam energies above $280 MeV$, the first inelastic reaction channel opens is the single-pion production. Compared to the previously discussed pion exchange picture, the creation of real particles is energetically possible in this energy regime. The following different combinations of initial and final states are possible for

the pp and pn systems:

$$\begin{aligned} p+p &\rightarrow p+p+\pi^0 \\ &\rightarrow p+n+\pi^- \\ p+n &\rightarrow p+n+\pi^0 \\ &\rightarrow p+p+\pi^- \\ &\rightarrow n+n+\pi^+ \end{aligned} \tag{48}$$

It is again considered that the nn system is equivalent to pp. Although the pn has more final state possibilities, the production cross section is lower than for the pp system (see Fig. 6 and Fig. 8). The investigation of such a 3-body final state is quite complex, but it can be simplified by concentrating on the isospin conservation. To estimate the difference between both systems for a specific final state, the pp and pn system can be expressed in the Dirac notation $|I, I_z\rangle$ in terms of the isospin I and its third component I_z as

$$\begin{aligned} |pp\rangle &= |1, +1\rangle \\ |pn\rangle &= \frac{1}{\sqrt{2}}(|1,0\rangle - |0,0\rangle) \end{aligned} \tag{49}$$

The pn system is again a combination of the isospin singlet and triplet state. The factor $1/\sqrt{2}$ is the Glebsch-Gordon coefficient for adding angular momenta of a combined system. For a final state, including deuterium, an additional π^+ (initial pp) or π^0 (initial pn) is produced (see Eq. (48)). The final states can be written as

$$\begin{aligned} |d\pi^+\rangle &= |1, +1\rangle \\ |d\pi^0\rangle &= |1, 0\rangle \end{aligned} \tag{50}$$

If the corresponding final state in Eq. (50) acts on the initial state in Eq. (49), just the isovector ($I = 1$) part of the pn system contributes. Therefore, the reaction probability for the pp system in this example is two times larger than for the pn system.
In total, σ_{pn} was estimated to be about 62% of σ_{pp} for the one-pion procduction according to [48].
Besides the dominant single pion production, a second inelastic reaction channel opens for nucleon-nucleon reactions below $1GeV$. The two-pion production reaction becomes energetically possible above a threshold of $\sim 530MeV$. However, the production cross section for multiple-pions is orders of magnitude smaller compared to one-pion production [48]. Both the single- and multiple-pion production mechanism lead to isospin change or knockout reaction in the case of a nucleus projectile and therefore contribute to the investigated total interaction cross section.

2.2.2 Nuclear Density Distribution

The integral over the nuclear density distribution is used in the Glauber framework to translate the free nucleon-nucleon cross section to nucleus-nucleus reactions. The first experimental determination of a nucleus size can be ascribed to the pioneering work of Rutherford et al. [51]. By letting alpha particles impinge on a gold foil, it was possible to estimate the size of the nucleus as a few femtometers. Since the alpha particle interacts via electromagnetic and the strong force, such an experiment probes the total nuclear size. As discussed in Chapter 1, it is necessary to distinguish between the matter radius, which represents the spatial neutron density distribution, and the charge radius of the proton density. In the case of a stable nucleus with the same proton and neutron number like ^{12}C, both distributions can be assumed to be spherically symmetric and of the same size. Hence, for calculations of the ^{12}C+^{12}C total reaction cross section, it is just necessary to measure the charge radius precisely.
Since the first experiment by Rutherford et al., the techniques to measure the charge radius have been extensively developed. The most established methods to determine the charge radius of stable isotopes are electron scattering and spectroscopy of muonic atoms. Both use the electroweak interaction of a point-like lepton with the spatially extended nucleus, either in scattering experiments or by investigating the binding energy. A descriptive overview of the different experimental techniques, even for the measurement of charge radii of unstable isotopes, can be found in [40]
Calculations of total reaction cross sections of ^{12}C+^{12}C, which were published in [42] and are discussed in this work, were carried out with charge densities determined from electron scattering data. The differential cross section of an elastic scattering process of charged particles on point-like potential is defined by the Rutherford formula. To extend this expression to a spatially extended target potential, the so-called form factor $F(q^2)$ is introduced

$$\frac{d\sigma}{d\Omega} = \left(\frac{d\sigma}{d\Omega}\right)_{Rutherford} \cdot \left|F\left(q^2\right)\right| \tag{51}$$

where q is the momentum transfer carried by the virtual photon. For a spherically symmetric potential, the form factor can be expressed as the Fourier transform of the charge distribution ρ_c as

$$F(q^2) = \frac{4\pi\hbar}{q}\int_0^\infty drr\rho_c(r)sin(qr/\hbar) \tag{52}$$

With this definition, the charge density distribution can be written as

$$\rho_c(r) = \frac{1}{2\pi\hbar^2}\int_0^\infty dqq^2F(q^2)\frac{sin(qr/\hbar)}{qr} \tag{53}$$

Since experimental elastic scattering data and the form factor are restricted to a specific range of q, the representation of the charge density distribution is limited. This can be

compensated using model-dependent analysis of the density by assuming a functional shape of, e.g., a Fermi or harmonic oscillator type. The parametrization for the ^{12}C density distribution used in the provided calculations was presented in [52] and gives an rms radius of $2.3fm$.

2.3 In-Medium Modifications

The derived Eq. (46) contains realistic energy-dependent reaction probabilities for single nucleon-nucleon interactions, which were interpolated to nucleon-nucleon reactions by integrating over measured density distributions. However, dynamical and structural in-medium modifications of nucleons inside nuclei have not been considered so far. This chapter briefly overviews different in-medium corrections to the Glauber Model as summarized and discussed in [42].

2.3.1 Fermi Motion

The relative motion of nucleons inside a nucleus follows, according to the Glodhaber model [53], a Gaussian momentum distribution. This so-called Fermi motion can modify the collision energy and, therefore, could lead to a shift of the total reaction cross section. The proposed attempt to include this momentum uncertainty of projectile and target nucleons, presented in [42] is to use a Fermi motion-average nucleon-nucleon cross section. This modification of Eq. (43) increases the interaction cross section for calculations of ^{12}C + ^{12}C collisions. Nevertheless, this increase amounts to $\sim 3\%$ for beam energies of 30 MeV/nucleon and is smaller than 0.1 % for energies above 200 MeV/nucleon [42]. Therefore, the effect of Fermi motion is negligible for discussing the presented analysis.

2.3.2 Pauli Blocking

A non-negligible in-medium effect appears by considering excitations of the projectile nucleus induced by inelastic scattering processes. According to Paulis exclusion principle, certain final states that are already occupied cannot be populated and are forbidden. This reduces the phase space and, therefore, leads to a reduction of the total reaction cross section. In a geometrical approximation, the projectile and target nucleus can be considered as Fermi spheres with radii k_{F1} and k_{F2}. Here, Pauli blocking can be introduced by restricting the final nucleon momenta outside these spheres. This limits the possible scattering angles for the nucleons.
Based on that geometrical treatment, Bertulani et al. [41] have presented an analytical expression that introduces Pauli blocking as a reduction of the nucleon-nucleon cross

section as

$$\sigma_{NN}^{Pauli}(E,\rho_1,\rho_2) = \sigma_{NN}^{free}(E)\frac{1}{1+1.982\left(\frac{|\rho_1-\rho_2|}{\tilde{\rho}\rho_0}\right)}^{2.75} \times \begin{cases} 1-\frac{37.02\tilde{\rho}^{2/3}}{E} & \text{if } E > 46.27\tilde{\rho}^{2/3} \\ \frac{E}{231.38\tilde{\rho}^{2/3}} & \text{if } E \leq 46.27\tilde{\rho}^{2/3} \end{cases} \tag{54}$$

Here E is the beam energy, $\tilde{\rho} = (\rho_1 + \rho_2)/\rho_0$ with $\rho_0 = 0.16fm^{-3}$ and $\rho_{1/2}$ are the local nucleon densities. As presented in [42] for calculations for ^{12}C+^{12}C collisions, Pauli blocking reduces the total reaction cross section significantly at low energies and becomes less important for larger beam energies.

2.3.3 Coulomb Repulsion

The integration factor b in Eq. (46) denotes the impact parameter. This parameter defines the density overlap of the projectile and target along a straight-line trajectory in the discussed geometrical treatment of scattering processes in the Glauber framework. At low bombarding energies, the Coulomb field can distort the relative motion of the projectile and target. Such a distortion of the straight line can, according to [45], be introduced by a modification of the impact parameter as the distance of closest approach b' under the influence of the Coulomb potentials at each value of b

$$b' = \left(\eta + \sqrt{\eta^2 + b^2k^2}\right)/k, \tag{55}$$

where $\eta = Z_1Z_2e^2/(4\pi\epsilon_0\hbar v^2)$ is the dimensionless Sommerfeld parameter. This correction reduces the total reaction cross section, especially for heavy and highly charged particles. Nevertheless, it has also a non-negligible effect on the ^{12}C+^{12}C system [42].

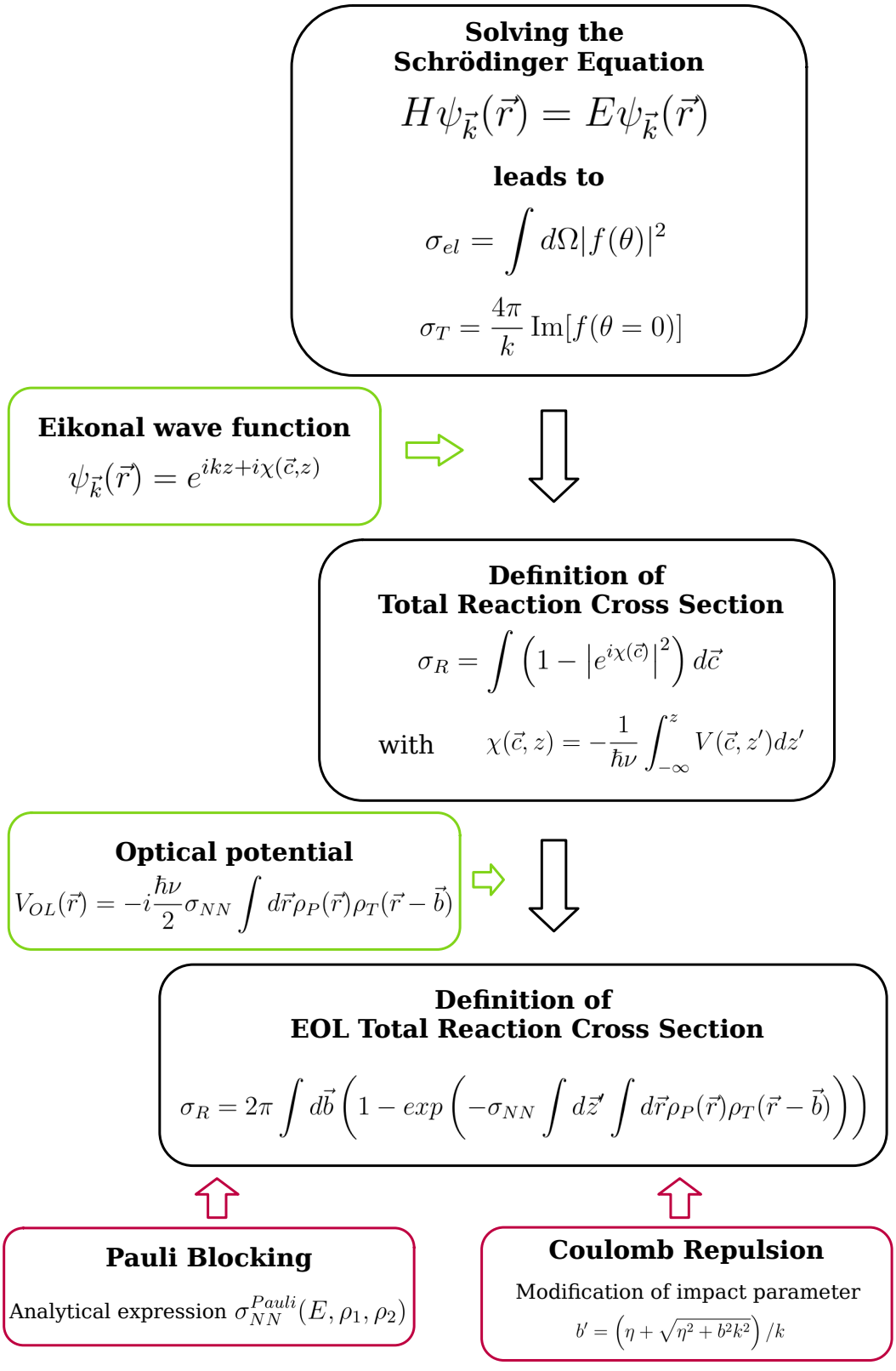

Figure 9: Overview for the total reaction cross section deduction in the Glauber model.

2.4 Total Reaction Cross Sections for the ^{12}C+^{12}Cystem

Calculations of the total reaction cross section for ^{12}C+^{12}C collisions are published by Teixeira et al. [42] and were kindly provided by Carlos Bertulani [47] for a comparison with the presented analysis results. The black symbols in Fig. 10 represent cross-section calculations using Eq. (46) with the parameterization for the free nucleon-nucleon cross section as presented in [41] and the ^{12}C density distribution discussed in the previous section. The in-medium modifications, namely Pauli blocking and Coulomb repulsion, were included in the same calculation and are plotted with red diamonds in Fig. 10.

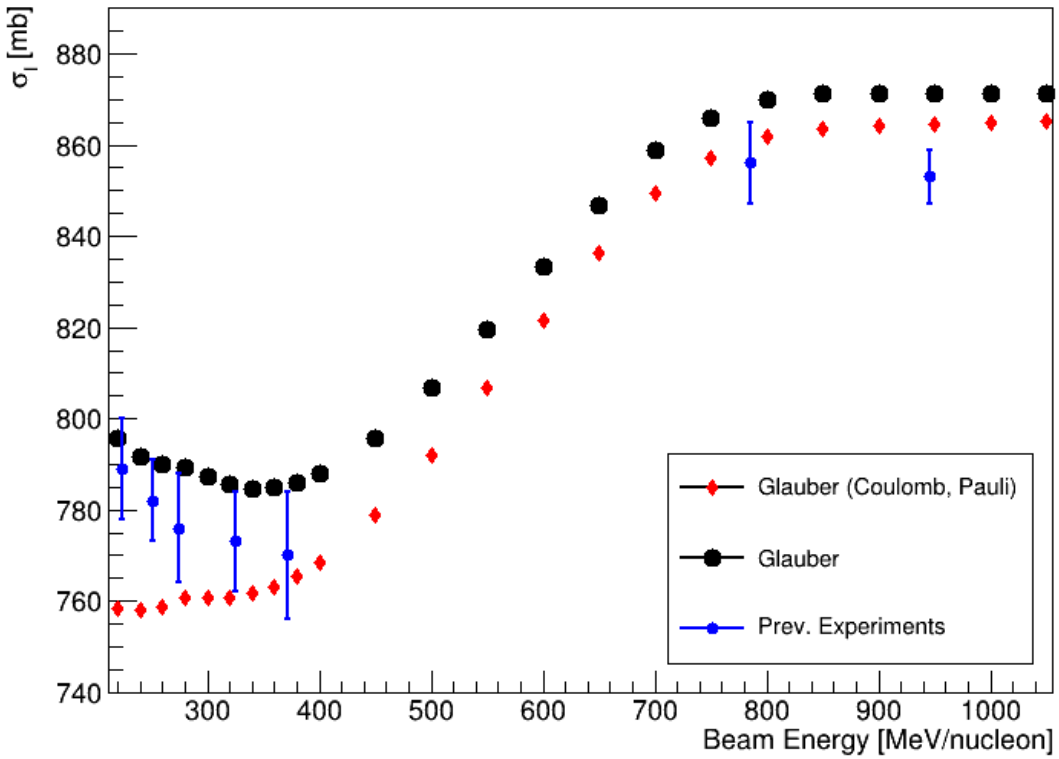

Figure 10: Total interaction cross section for versus beam energy for ^{12}C+^{12}C. The black symbols illustrate data points for an eikonal calculation in the optical-limit approximation (according to Eq. (46)). The red diamonds are results from the same calculation but include in-medium modifications (Pauli blocking and Coulomb repulsion), as discussed in Section 2.3. Blue data points are results from previous experiments [54, 55, 56].

In the energy regime between 350 and 1000 MeV/nucleon, just three experimental data points are available (370 MeV/nucleon - Takechi et al. [55], 790 MeV/nucleon - Tanihata et al. [54], 950 MeV/nucleon - Ozawa et al. [56]). At low energies, the

inclusion of Pauli blocking seems to overestimate this effect. This was already discussed in [42], where it is argued that excluding both full Fermi spheres might overestimate Pauli blocking. With increasing beam energy, the probability for inelastic excitation into a bound state decreases [57], and pion production remains as a dominant contribution to the total reaction cross section. The data points at 370, and 790 MeV/nucleon seem to agree with the in-medium corrected Glauber calculation. However, the significant uncertainties (>2%) for this data do not allow a final confirmation of the presented Glauber data. By also considering the data point at 950 MeV/nucleon, the red diamonds are overestimating the experimental data at high energies up to 2%. Furthermore, no experimental data is available in the regime between 500 and 750 MeV/nucleon, where the cross section rises with the beam energy. For a conclusive analysis of the impact of the presented in-medium corrections on the $^{12}C+^{12}C$ reaction system at high energies, experimental data with an uncertainty smaller than 1% is needed.

The analysis presented here not only provides precise values for the total interaction cross section of $^{12}C+^{12}C$ at beam energies of 400, 800, and 1000 MeV/nucleon to validate previous results. Additionally, two more data points at 550 and 650 MeV/nucleon are presented, which allow a systematic analysis of the energy dependence and constrain the impact of modifications of Glauber calculations.

3 Experimental Concept and Setup

This chapter starts with a discussion of the general challenges in measurements of absolute cross sections. The presented experiment was carried out as the first part of the FAIR Phase-0 campaign of the R^3B (Reaction with Relativistic Radioactive Beams) collaboration at the GSI/FAIR facility, introduced with a brief historical review. The underlying experiment's setup and main detector systems are presented in Chapter 3.3 and the following.

3.1 Requirements for Absolute Measurements

Reaction cross sections are fundamental quantities in nuclear physics and are essential for understanding, e.g., reaction rates in astrophysical processes. Many models and observations, as discussed in Chapter 1, are supported by experimental cross-section data. The accuracy and predictive power of theoretical calculation are, therefore, highly influenced by the precision of this data. Since the experimental uncertainty propagates into the model uncertainty, the interpretation of precise astrophysical observations can be improved by high-quality experimental data.
In a simplified form, the cross section σ for any reaction can be defined with three measurable quantities as

$$\sigma(E) = \frac{N_R}{N_0 \cdot N_t} \tag{56}$$

, where N_R and N_0 are the number of reactions and incoming particles on the target per unit time. The number of particles or scattering centers per unit area in the target is denoted by N_t. All three quantities contribute to the total uncertainty of the measured cross section. In the following, a short overview of challenges and requirements for the measurement of absolute cross sections is provided.
Inhomogeneity and contamination of the target material falsify the determination of scattering centers N_t. Therefore, the analysis and specification of the target material is an essential step for the preparation of an experiment (see Section 3.5). Additionally, the operation of detector systems in vacuum improves the accuracy of a measurement by reducing the number of additional scattering centers along the particle trajectory.
Identifying incoming projectiles represents a challenge for the acceleration facility and the experimental setup. The delivered beam characteristic varies depending on the experimental requirements for specific measurements. Measurements with exotic and short-lived nuclei require a dedicated identification system with precise mass and charge resolution before the experimental cave. To achieve a high-purity isotope separation, the nucleus has to be fully stripped, which requires high secondary beam energies.

The identification of projectiles on the target is mainly done by detector systems right in front of the target area. It is essential to analyze the incident angle to guarantee that the beam just hits the target surface. Another beam characteristic, which can vary for different experiments, is the intensity and time structure. High beam intensities reduce the statistical uncertainty in the data but also face a challenge to the detector response and dead time for the whole system.
For measurements of total reaction cross sections, N_R represents the absolute value of reactions in the target material. This seems trivial but implicates several challenges. The usage of a thick reaction target minimizes the statistical uncertainty of this quantity but results in large angular and energy straggling for reaction products. Therefore, a setup with large geometrical acceptance is needed for complete identification. In addition the detector themselves act as a target. This contribution is measured by so-called empty target measurements, which has a substantial impact on statistical errors. Background radiation from the experimental cave or detector material can cause additional contamination in the signal. Identifying all reaction products in so-called kinematically complete measurements generates a set of redundant observables. This information can be used to minimize the background to get a clear signal signature and to identify specific reaction channels.
The following sections will reveal why the R^3B experimental setup at GSI/FAIR represents the perfect environment to challenge the discussed requirements for measurements of total interaction cross sections at relativistic energies.

3.2 GSI/FAIR Facility

The "GSI Helmholtzzentrum für Schwerionenforschung" is an accelerator facility located in Darmstadt in Germany. It was founded as "Gesellschaft für Schwerionenforschung mbH" in 1969, joined the Helmholtz Association in 1970, and started operation in 1975 with the linear accelerator UNILAC. From these first days up to today, GSI has evolved into an international and multidisciplinary campus, including biophysics research, development of medical applications (e.g., ion therapy was established as cancer treatment), a versatile petawatt laser facility (PHELIX), and many more. The Discovery of six new chemical elements (Bohrium, Hassium, Meitnerium, Darmstadtium, Roentgenium, Copernicium) from 1981 until 2010 are milestones of GSI.
The production of heavy ion beams at GSI can be separated into four stages:

- The ion source
- The linear accelerator UNILAC - "UNIversal Linear ACcelerator"
- The ring accelerator SIS18 - "SchwerIonenSynchrotron 18"

- The fragment separator FRS

The starting point of every heavy ion beam experiment is the ionization of neutral atoms, which is done in the ion source. Depending on the requirements of a proposed experiment, elements ranging from hydrogen to uranium can be used as sources. There are various types of ion source devices available at GSI. However, the standard procedure is to create free electrons of the injected gas or solid material by applying high voltages. This leads to a chain reaction of further electron collisions, generating a plasma. At this stage, ions are extracted with high voltage and injected into the linear accelerator UNILAC. The pre-acceleration in UNILAC is done with a radio-frequency quadrupole and consecutive cavities where the bunched beam reaches approximately 5% of the velocity of light. An intermediate stripping stage allows to strip off more electrons and thus achieves a high acceleration efficiency. In the second acceleration stage, the beam reaches a final velocity of around 16 % of the speed of light. The beam can now be guided in one of the experimental caves in the "Targethalle 1" or further accelerated with the SIS18. In the transfer channel to the SIS another stripper removes all remaining electrons to provide the lowest rigidity, especially for the very heavy ions. With a circumference of 216 meters, this ring accelerator can accelerate stable ions from hydrogen up to uranium to a velocity of nearly 90 % of the speed of light.

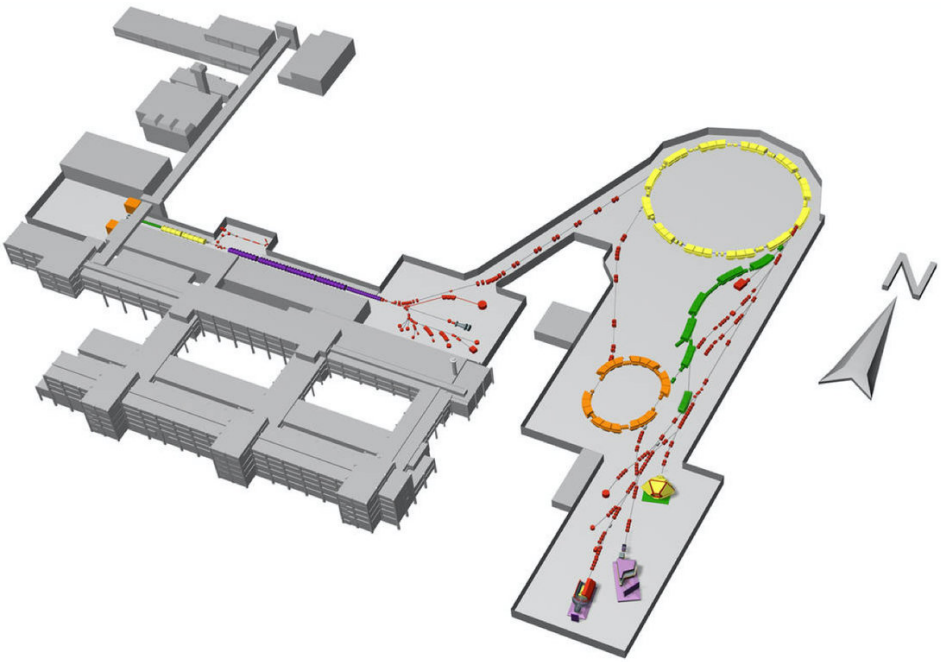

Figure 11: Schematic view of the GSI accelerator facility. The picture was taken from [58]

The high-energy beam is now guided directly in one of the experimental areas called "caves" or can be used to produce exotic nuclei. In the collision with a production

target in front of the FRS, all kinds of isotopes are created in various reactions. This in-flight-produced ion cocktail enters the fragment separator. Several sets of magnetic quadrupoles and dipoles separate the ion species of interest and deliver this secondary beam to the individual experiments.
As an upgrade of GSI, the realization of FAIR, the Facility for Antiproton and Ion Research, was approved in 2003. The main components of FAIR will be the SIS100 synchrotron and the Super-Fragment-Separator - Super-FRS. The ion beam of SIS18 will be used as an injection for SIS100. With a circumference of 1100 meters, it allows for much higher beam intensities or energies, up to 99 % of the speed of light. The combined operation with the Super-FRS enables unique possibilities for an accelerator facility worldwide. Primary beam intensities of 10^{11} particles per second allow to produce the most exotic nuclei with a reasonable intensity. The high primary beam energies enable the production of fully stripped exotic ions, which can precisely be separated in a three-stage analysis of the magnetic rigidity and energy loss and with a large phase-space acceptance of the Super-FRS.
As part of the NUSTAR (NUclear Structure, Astrophysics and Reactions) collaboration, the R^3B experiment will be located at the focal plane of the high-energy branch after Super-FRS at FAIR.

3.3 R^3B at GSI/FAIR

The R^3B setup is designed and currently constructed for kinematically complete reaction studies with exotic nuclei at the upcoming FAIR facility. The broad physics program of R^3B [59] ranges from the investigation of the dynamics and structure of nuclei far off stability [60] to studies of astrophysical reactions [61]. A schematic view of the different main detector systems is shown in Fig. 12. The whole setup can be described as a magnetic dipole spectrometer with a series of different detector elements arranged before and after the GLAD magnet. Depending on the requirement of a proposed experiment, the detectors can be independently arranged at different positions around GLAD. This flexibility and the detector design allow to adapt the setup to the highest possible transmission efficiency of secondary beams delivered by the Super-FRS.

The incoming radioactive ion beams (RIB) from the fragment separator (left side in Fig. 12) are tracked and identified via time-of-flight (ToF) and ΔE measurements on an event-by-event basis. A calorimeter for the simultaneous detection of gamma rays and light-charged particles (CALIFA), which will consist of 1952 individual CsI crystals [63, 64] in its final design, surrounds the reaction target and will cover polar angles between 7° and 140° [65]. Projectiles and reaction residues after the target are kinematically focused forward and enter the large acceptance dipole magnet GLAD.

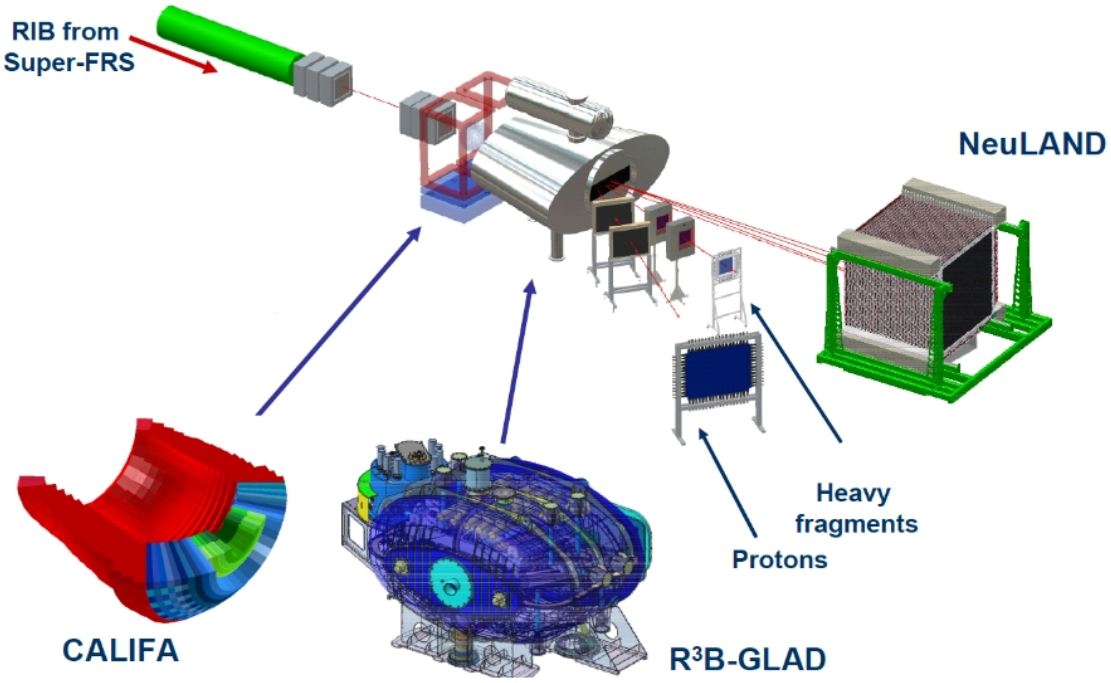

Figure 12: Schematic view of the R^{3}B experimental setup in the configuration used during the FAIR phase-0 campaign. The picture was taken from [62].

They are identified via a momentum analysis, including detectors at the heavy and light fragment arm after GLAD. Knocked-out or evaporated neutrons are detected by the new large array neutron detector (NeuLAND), which is installed at zero degrees after GLAD [66].
The capability of R^{3}B to precisely identify incoming beams on an event-by-event basis, as well as to detect all reaction particles and gamma rays in kinematically complete measurements, presents the perfect environment for precise measurements of absolute reaction cross sections.

3.4 Detector Components in the S444 Experiment

The underlying experimental data was recorded during the S444 commissioning experiment of the R^{3}B collaboration in February 2019, which was the first experiment of the FAIR Phase-0 program in Cave-C at GSI. Fig. 13 shows a schematic view of the main detector systems of the R^{3}B setup used during the commissioning in Cave-C. To minimize multiple scattering, the particles were propagated in vacuum from the beam entry of the cave to the magnet, its detector chamber, and the connected vacuum pipe with a diameter of 60 cm on the fragment arm. After the beam exit window, only the last two fiber detectors and the TOFD scintillator wall were operated in air.

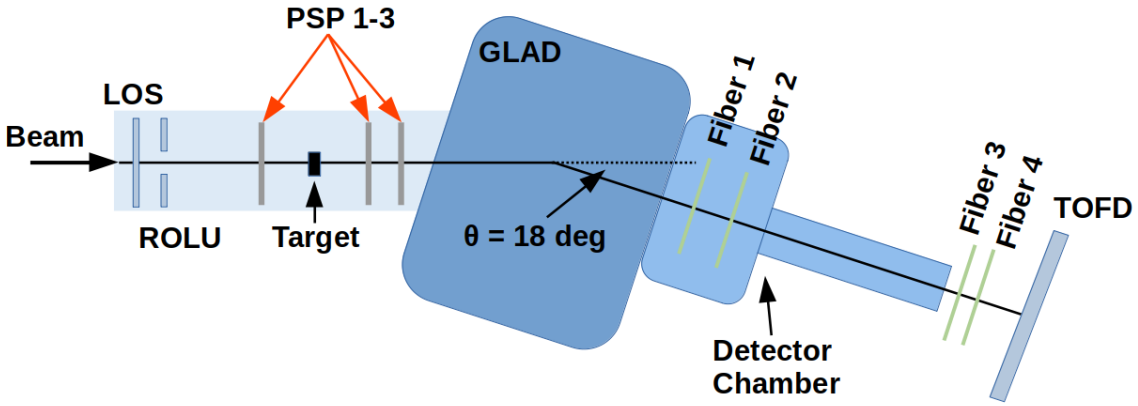

Figure 13: Schematic view of the R^3B experimental setup used during the S444 commissioning experiment in the Cave-C at GSI.

3.4.1 LOS and ROLU

Coming from the SIS18, the beam enters the experimental setup in Cave-C from the left side in Fig. 13. The first detector in the R^3B beamline in Cave-C is the LOS detector. LOS is made of an octagonal-shaped plastic scintillator material (EJ204) with a thickness of 0.5 mm and an active area with a diameter of 65 mm. LOS is read out by eight Hamamatsu photomultipliers directly glued on the back side surface. This design maximizes the collected light and enables a charge and position identification of incoming particles.

The following detector right after LOS is ROLU which consists of four rectangular scintillators where two of each forming a slit in the vertical and horizontal direction, respectively. The ROLU signal is used as a veto to exclude particles with a larger offset to the beamline than the adjustable ROLU aperture. In the discussed experiment, typical openings of Δ x/y = $\pm$5 mm were used.

3.4.2 PSP Detector

PSP detectors are made of silicon with 32 vertical resistive strips on the front and 32 horizontal resistive strips on the backside. Each strip has a length of 9.57 cm, which gives a total active area of 9.57 x 9.57 cm^2. All detectors have a total thickness of 313 μm. By measuring the collected charge at both ends of one strip, it is possible to identify the energy loss and, thus, the charge of passing particles and their position along the strip.

A set of three PSP silicon strip detectors was installed in the setup to make a charge and position identification before and after the target. PSP1 was installed 0.8 m upstream

of the fixed target/reaction point. PSP2 was mounted 0.8 m after the target, and PSP3 with a displacement of 0.2 m further downstream.

3.4.3 GLAD

GLAD is a zero-degree superconducting dipole magnet with a large angular acceptance (±80 mrad for neutrons) and an adjustable integrated magnetic field of max. 5 Tm. The GLAD current and, thus, the magnetic field strength was adjusted for each beam energy individually to deflect ^{12}C isotopes onto the 18-degree line with respect to the incoming beam. To avoid hysteresis effects and to cover an extensive program of more than 40 different beam/target combinations, the magnet setting was not changed for additional energy loss in different targets.

3.4.4 Fiber Detector

Four fiber detectors were used for particle identification after the magnetic field of GLAD. Two of them - Fiber 1 and Fiber 2 - using vertical fibers only are placed inside the detector chamber perpendicular to the 18-degree line at a distance of 1.5 m with respect to each other. Fiber 3 and 4 are mounted right after the exit window of the vacuum pipe, with Fiber 4 rotated by 90 degrees to also measure the vertical beam position.
All four fiber detectors used in this experiment have an active area of 50 x 50 cm^2 consisting of 1024 square-shaped fibers with a thickness of 500 μm. The fibers are read out on one side by two Hamamatsu multi-anode photomultiplier tubes (PMT) with two adjacent fibers connected to one pixel and on the other side by four single PMTs, connecting odd or even fiber numbers in different PMTs. Due to the longer drift length of the photoelectrons in the single PMTs, the magnetic field affected the performance of these detectors in the detector chamber dramatically. Therefore, the analysis was performed without the single PMT information; thus, two neighboring fibers could not be distinguished.

3.4.5 Time-of-Flight wall - TOFD

A newly designed Time-of-Flight wall - TOFD [67] - was installed at the end of the setup, perpendicular to the 18-degree line. This detector is designed for the identification of heavy reaction fragments. In the used configuration, TOFD consists of 4 planes with each 44 vertical plastic scintillator bars, which have a dimension of 1000 x 27 x 5 mm^3 and are shifted with respect to the adjacent plane by half a bar. The total active area of this detector is 1200 x 1000 mm^2. Each bar is read out at both ends by a PMT with

a fast timing response. This allows precise time-of-flight measurement (σ up to 14 ps for uranium) and charge identification via ΔE measurement.

3.5 Target Specification

Figure 14: Orginal mechanical drawing of the target wheel. In the S444 experiment, the target wheel hosts 7 different targets and a large cut-out for background measurements.

A target wheel, as shown in Fig. 14, was mounted between PSP1 and PSP2. It can hold up to seven targets and has a remote-controlled stepper motor. In the actual version, two holders were merged into a large cut-out, which enables background measurements.
In addition to three carbon targets, two CH_2 targets, one Pb, and a segmented plastic target were mounted. In consideration of the $^{12}C+^{12}C$ analysis, the focus of the remaining chapter lies on the carbon targets.
The target material was ordered from "SGL Carbon GmbH", cut and prepared by the GSI workshop, and characterized in the GSI target lab. An essential quantity for determining cross sections is the number of scattering centers per unit area inside the target material. Or, more precisely, the number of carbon atoms the beam particle passes on its way through the target.
To precisely determine this number, two target properties, namely the volume density ρ and the thickness in beam direction z, must be measured.

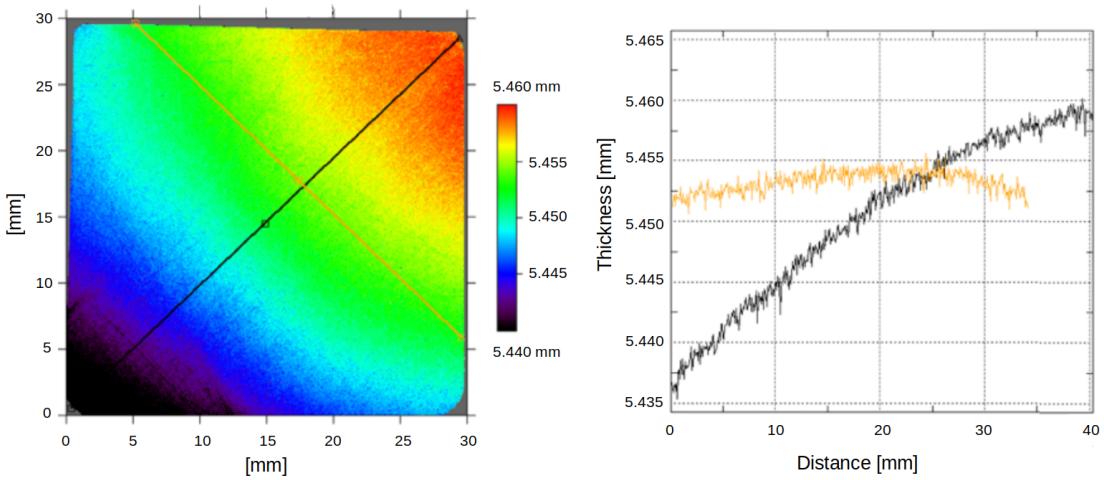

(a) Thin carbon target

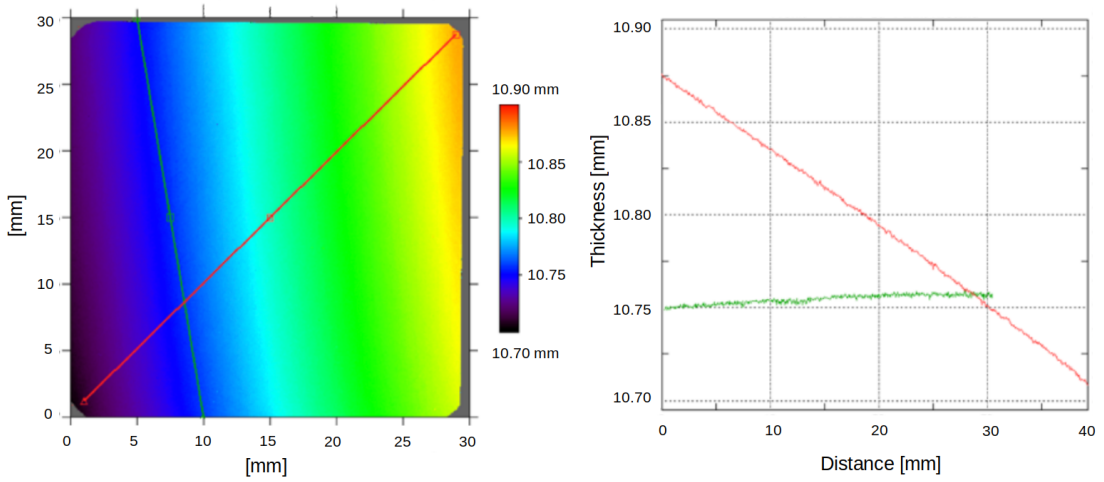

(b) Medium carbon target

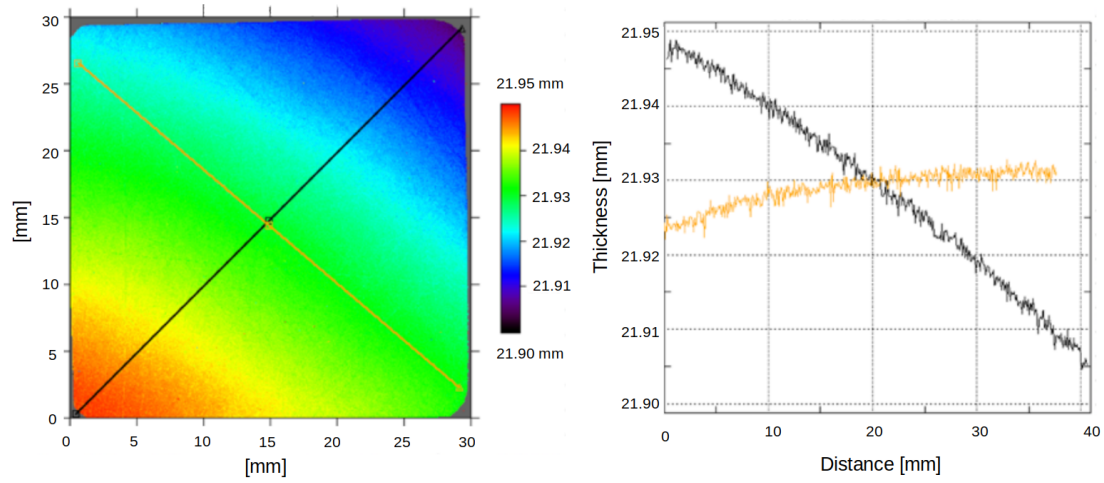

(c) Thick carbon target

Figure 15: Target thickness measurement results from the GSI target lab.

According to the SGL data-sheet[1], the density of the target material is 1.84 g/cm^3, where unfortunately no errors are provided for this number .
The target thickness was measured in the GSI target lab over an area of 30 mm x 30 mm with a chromatic sensor. Fig. 15 shows the measurement result for the thin (a), medium (b), and thick (c) carbon targets. All panels on the left side show the 2D depth profile. The panels on the right side illustrate the indicated diagonal projection of the depth profile and a second variable projection over a homogeneous area.
To estimate the area on the target surface covered by the beam, it is possible to use the X- and Y-position information of PSP1 and PSP2, respectively. Since the target wheel was mounted right between PSP1 and PSP2, the X- and Y-position of particles at the target position can be calculated as:

$$\mathrm{X/Y_{target}} = \frac{\mathrm{X/Y_{PSP2}} - \mathrm{X/Y_{PSP1}}}{2} \tag{57}$$

Fig. 16 shows the measured XY beam spot position for an empty run. The width of

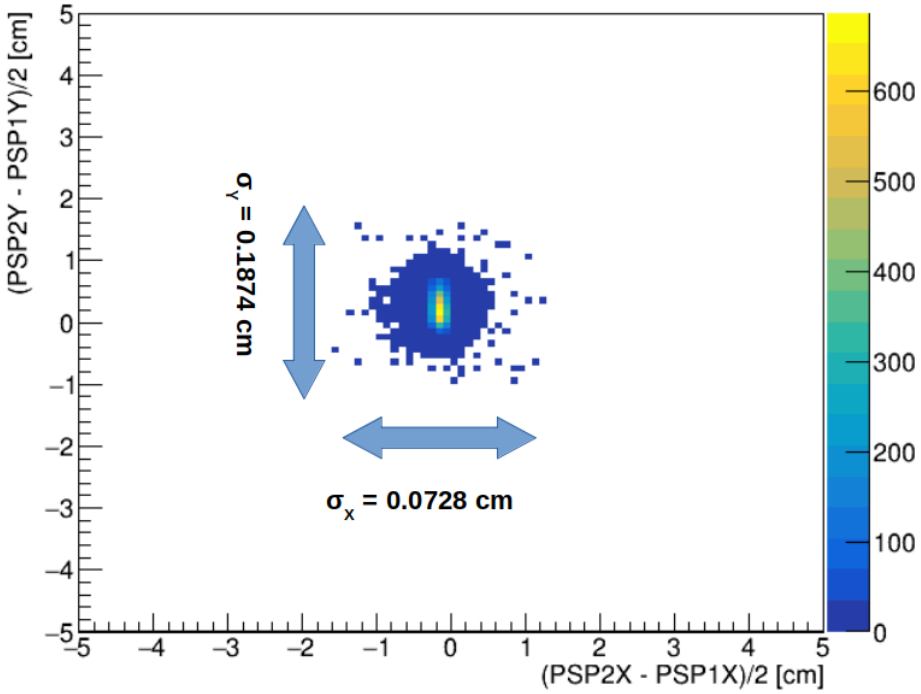

Figure 16: XY beam spot at the target position.

the beam spot is estimated by the standard deviation of a 2D Gaussian fit function with $\sigma_\mathrm{X} = 0.0728$ cm and $\sigma_\mathrm{Y} = 0.1874$ cm. The beam spot size was constant during the whole experiment. As shown in the right panels of Fig. 15, the target surface is flat in one direction and has a curvature in the other direction. Since it was not documented

[1]Data-sheet: Grade R 6650 / Specialty Graphites from SGL CARBON

whether the flat or curved direction corresponds to the measured X- and Y-direction of the PSPs, the most accurate estimation is to take the mean of both standard deviation values (0.1301 cm) and estimate the maximum thickness uncertainty using the curved surface projection.
The number of scattering centers per unit area is defined as:

$$N_t = \frac{\rho \cdot z \cdot N_A}{M}, \tag{58}$$

where N_A is the Avogadro constant ($6.02214076 \cdot 10^{23} mol^-1$), and M is the molar mass of carbon ($12.011 g \cdot mol^-1$). The measured mean values and standard deviations of the target thickness, as well as the resulting values and uncertainties for N_t are listed in Table 2:

^{12}C targets	d[cm]	N_t $[cm^{-2}]$	ΔN_t[%]
thin	0.5451(4)	$5.0289409 \cdot 10^{22}$	0.0648
medium	1.0793(15)	$9.9573215 \cdot 10^{22}$	0.2620
thick	2.1928(5)	$2.0230163 \cdot 10^{23}$	0.0322

Table 2: Target thickness d, number of scattering centers per unit area N_t and corresponding uncertainties for all three carbon targets.

3.6 Calibration of Detector Systems

The digitized experimental data of the various detector systems mainly consists of timing and amplitude information and is stored in so-called LMD (List-Mode-Data) file format. To extract the physics information on the involved particles, the data has to be unpacked, synchronized, and calibrated. The first step is to assign all signals to the correspondent physical detector channels. After time-sorting and stitching the signals of all independent detector systems within a global timestamp domain, the data is organized in an event-by-event structure. For this unpacking procedure, the UCESB (Unpack & Check Every Single Bit) software tool, developed by Håkan T. Johansson [68], is used. The output file is stored in ROOT format [69], which is compatible with the analysis software package R3BRoot[70], used in the present work.
The unpacked file contains accumulated electronic signals of the individual detectors mapped on the corresponding physical channels ("Mapped" level). For synchronization and calibration of the respective channels ("Cal" level), a set parameter has to be produced. Depending on the required detector information, the calibrated signals can be translated into physical quantities such as positions, energy loss, or nuclear charge ("Hit" level). This translation can require a dedicated measurement (e.g., a sweep run

along the detector's active area) and the detector geometry. Fig. 17 illustrates the calibration scheme for the TOFD detector from the Raw to the Hit level.
This section provides an overview of the general calibration procedure for the TOFD and PSP detectors. All calibration steps used in the present work are subroutines of the R3BRoot package.

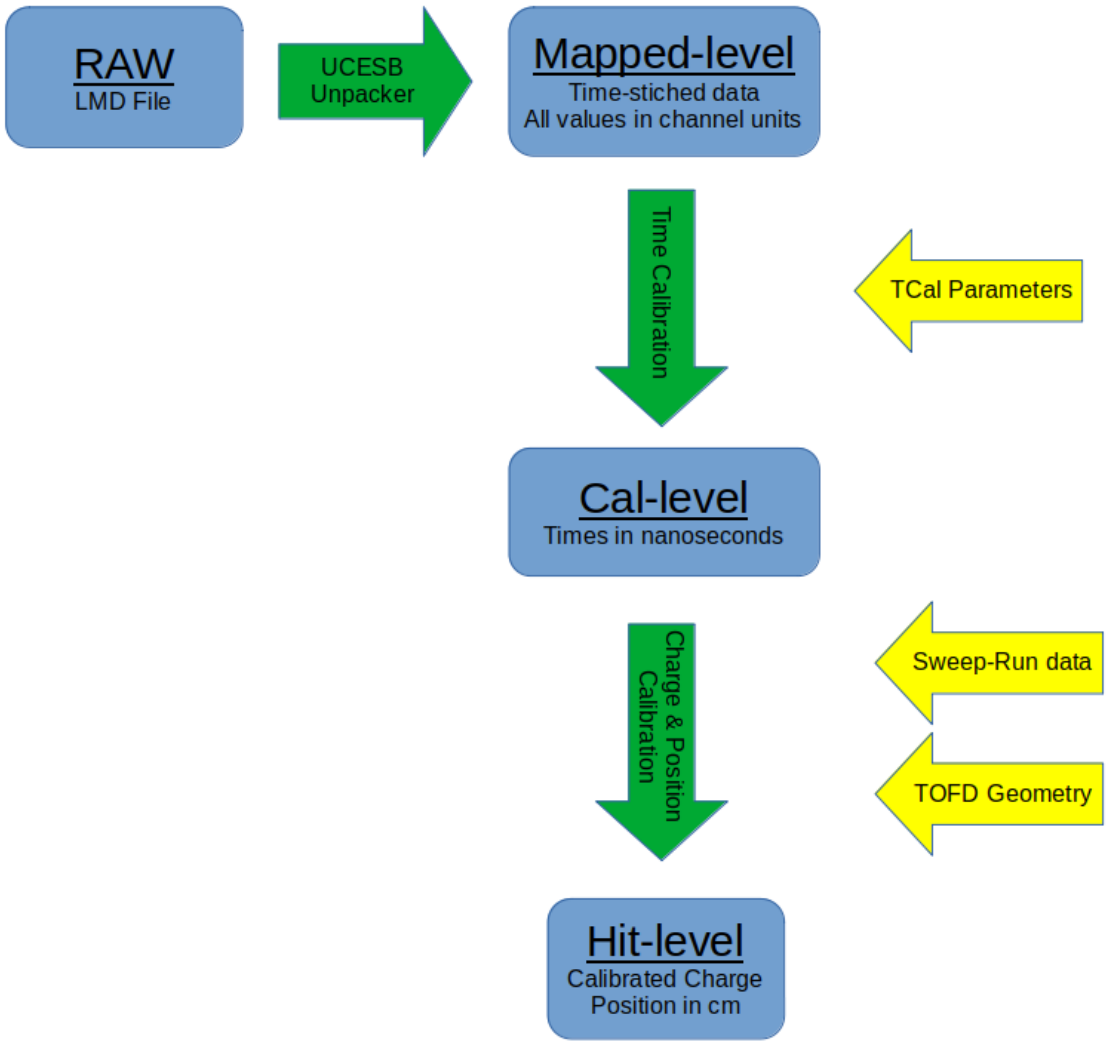

Figure 17: Calibration scheme for experimental TOFD data from raw to hit level (blue boxes). The yellow arrows illustrate the required parameter sets for the different calibration steps.

3.6.1 TOFD Calibration

The TOFD detector is designed to measure the Time-of-Flight (ToF) and nuclear charge of heavy fragments and the unreacted beam at the end of the experimental setup [67]. The later measurement states a challenge to the stability performance of the detector since the electronics have to compensate for high beam rates with multi-hit capability. The nuclear charge is identified by measuring the energy loss of the particles within the scintillator material. Such a measurement is done by a Time-over-Threshold (ToT) method. Fig. 18 illustrates this approach schematically. The time width, expressed by the leading and trailing edge, while the PMT signal exceeds a pre-defined threshold, can be converted to the energy loss in the detector material and, thus, to the nuclear charge of the projectile. To overcome the non-linearity of the produced amount of charge or signal height to the time width in standard ToT measurements, TOFD uses the filtered and integrated signal to measure the energy loss and identify the nuclear charge [67].

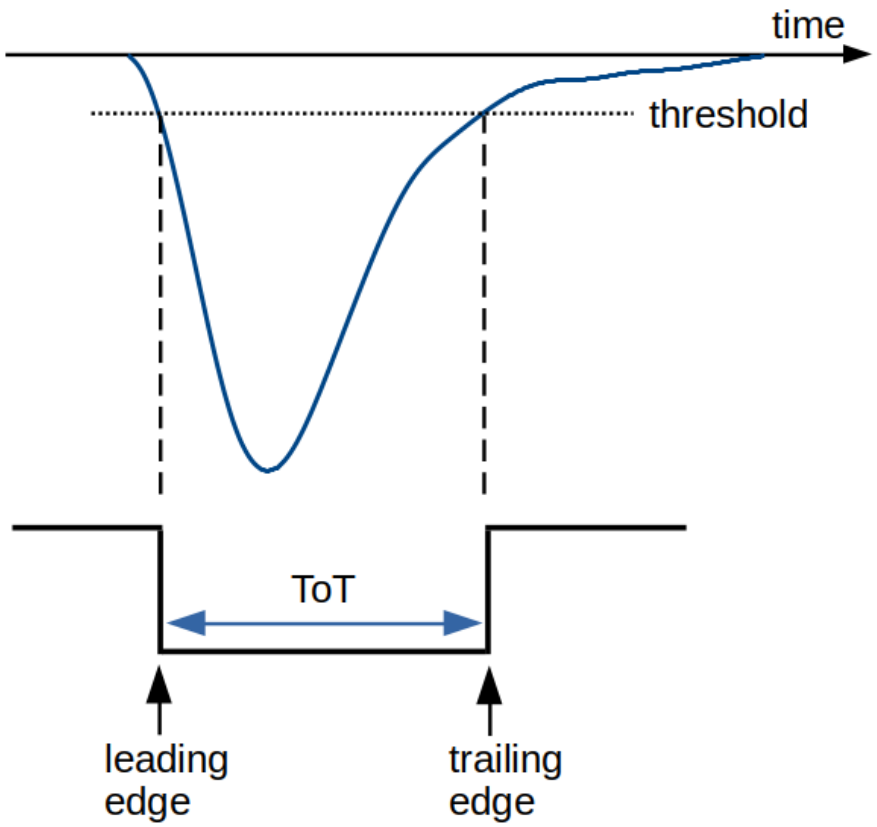

Figure 18: Time-over-Threshold measurement. The time width, while the signal exceeds the pre-defined threshold, is defined by the leading and trailing edge.

Time Measurement and Calibration

Time measurements for the leading and trailing edge information of the integrated and digitized signals are divided into coarse and fine time measurements. Counting the number of cycles of a 200 MHz readout clock defines the coarse time with a binning of 5 ns. Within such a clock cycle, the exact position of the signal rise with respect to the next clock cycle can be determined with an FPGA-based TDC. In a so-called tapped delay line (TDL), the incoming signal propagates through the delayed logic modules of the FPGA until the next clock cycle stops the sampling process. The number of modules can be converted in a time difference from the signal start to the end of the clock cycle, called fine time. This technique provides precision for the time measurement in the picosecond range. Fig. 19 illustrates the discussed relation between coarse and fine time together with a schematic view of an FPGA-based TDC measurement.

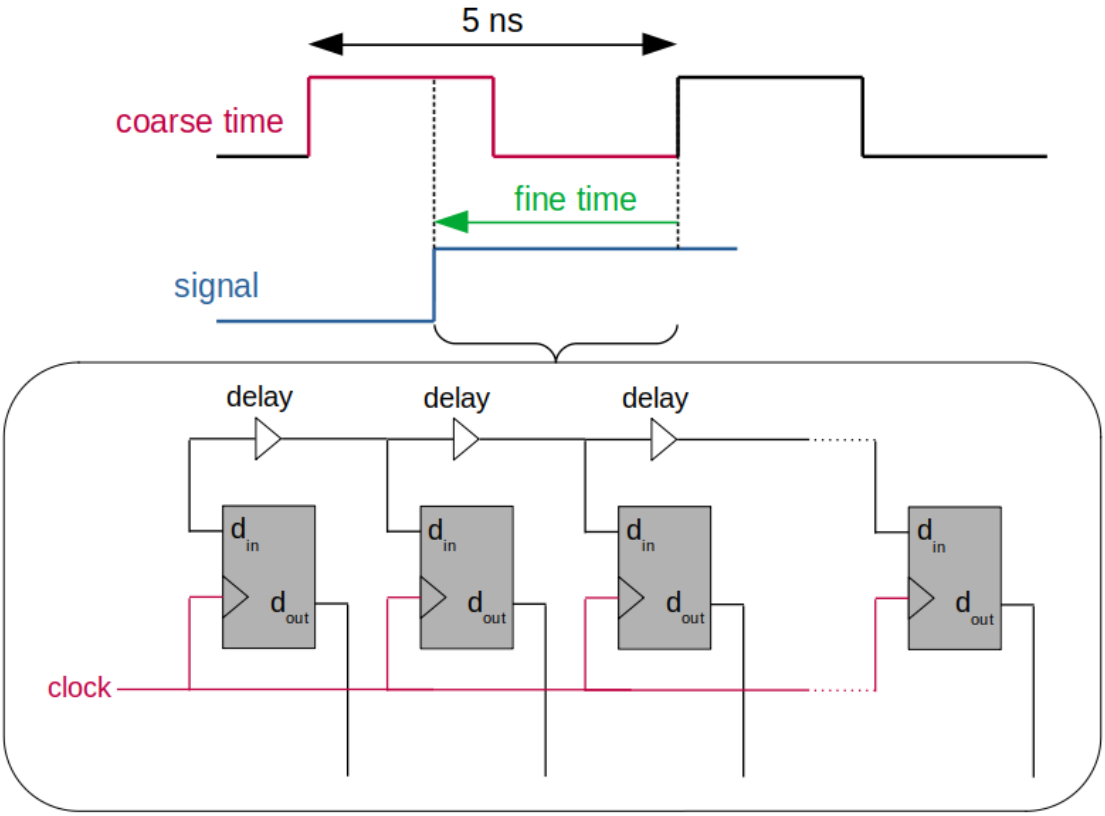

Figure 19: Time measurement with TOFD. The number of cycles of a 200 MHz clock defines the coarse time (red) with a precision of 5 ns. The fine time (green) is defined by the difference of the signal rise to the start of the next clock cycle and is determined with an FPGA-based TDC (lower panel). The signal is propagated through delayed FPGA modules until the next clock cycle stops the sampling process.

Coarse and fine time values are expressed in channel units. Since the fine time

counter is sensitive to the electronics' temperature shifts, a calibration should be carried out for each run individually. Also, the FPGA delay units are not constant; therefore, each channel needs its individual calibration parameter set. The accumulated and uniformly distributed fine time data for a single TDC channel is shown in the left panel of Fig. 20. By estimating the deviation of the measured data to a uniform distribution, a calibration function can be defined as

$$\text{Time} = \frac{\sum_{i=0}^{i=\text{bin}} \text{counts(i)}}{\sum_{i=0}^{i=\text{max}} \text{counts(i)}} \text{ClockTime} \tag{59}$$

The resulting calibration function is shown in the right panel of Fig. 20 and represents the correspondent time shift of each fine counter. This calibration procedure requires sufficient statistics for each TDC channel to generate a precise calibration function, which is stored in a lookup table.

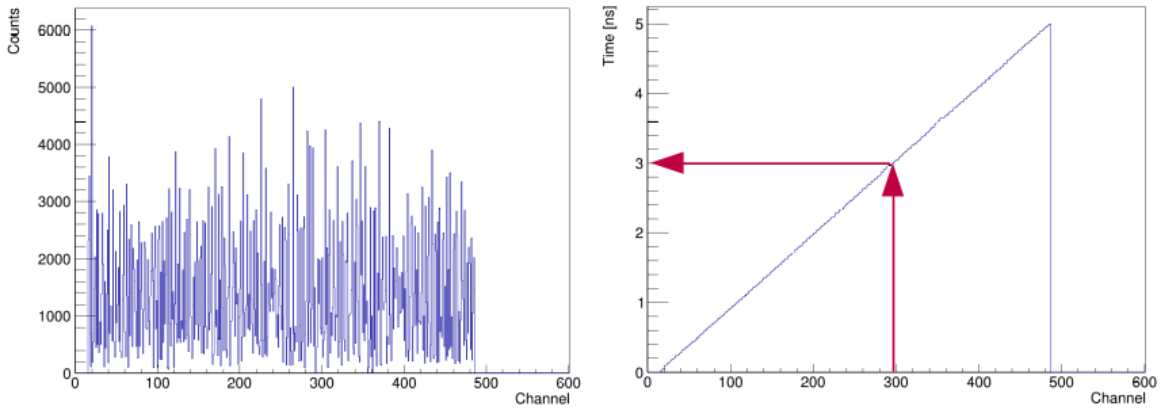

Figure 20: Time calibration for single TOFD channel. The left panel shows the accumulated fine time distribution of a single TDC channel. The resulting calibration function is shown in the right panel.

The resulting leading and trailing edge time information are calculated with the difference of corresponding coarse and fine time as:

$$\text{Time}_{\text{leading/trailing}} = \text{ClockCycle} \cdot \text{ClockTime} - \text{FineTime} \tag{60}$$

Position and Charge Calibration

The measured ToT values are proportional to the collected charges from the correspondent PMTs at each end of the scintillator bar. Since light is attenuated by traveling through the scintillator material, the PMT signal depends on the position where the particle hits the detector and can be expressed as

$$\text{ToT}_{\text{PMT1}} \propto \text{E}_{\text{PMT1}} = \text{E}_0 \cdot \exp(-\lambda \cdot \text{y}_{\text{PMT}}), \tag{61}$$

where λ is the absorption coefficient and y_{PMT1} is the distance between the particle impact position and the PMT. With this definition, the actual particle position on the bar can be calculated as

$$y_{TOFD} = \lambda \cdot \log\left(\frac{ToT_{PMT1}}{ToT_{PMT2}}\right) \tag{62}$$

The first calibration step is to gain match the ToT values for the PMT1 and PMT2. This is done with a horizontal sweep run in the middle of the active area of the detector. Fig. 21 shows the deposit particle energy (sqrt($ToT_{PMT1} \cdot ToT_{PMT2}$)) versus the calculated vertical position for a single bar in the sweep run. The prominent spot at around 100 represents the unreacted beam. Since the beam scans the detector in a central horizontal position, the deviation of the calculated position to zero is used to define an offset or gain-matching parameter for each PMT.
The absorption or attenuation coefficient is calculated in an identical procedure. With a horizontal sweep-run at a $y \neq 0$, λ can be determined to reproduce the adjusted beam height.

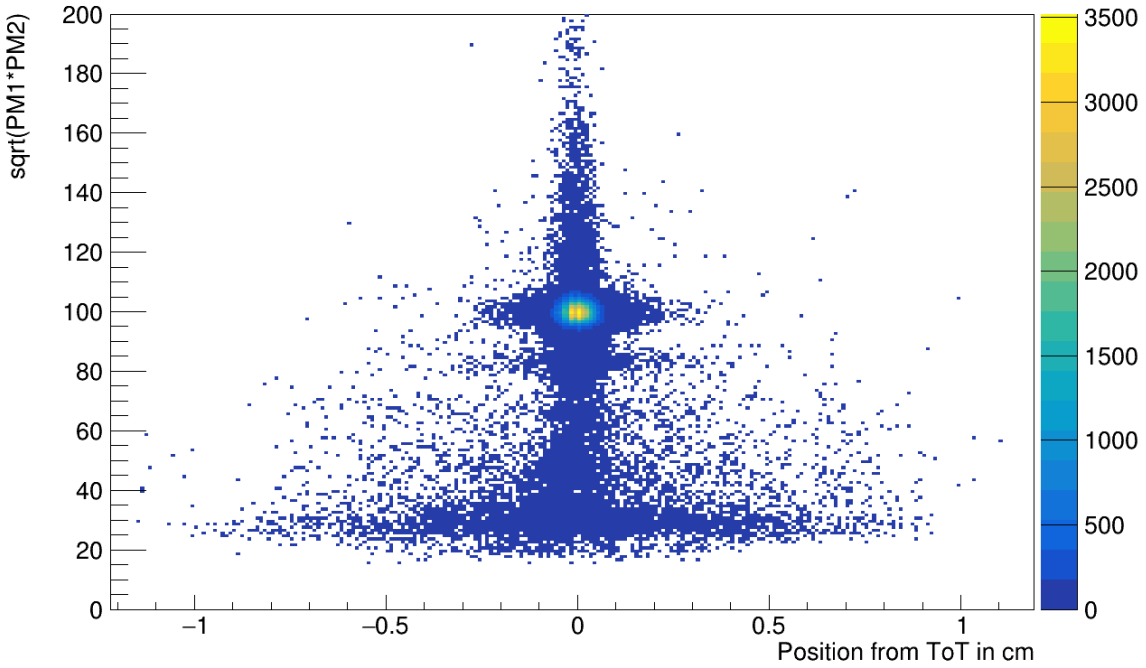

Figure 21: Deposit energy, calculated with sqrt($ToT_{PMT1} \cdot ToT_{PMT2}$), versus vertical hit position for a single bar in a horizontal sweep run.

As already mentioned, the measured energy depends strongly on the distance of the impact position of the particle to the PMT. This dependency turns out to become non-linear at the edges of the bar. To identify this non-linear behavior, a meander run is used. Fig. 22 shows again the deposited energy versus the vertical position for a single bar. The prominent band shows that the beam scanned the bar over a range of

around 100 cm. With a polynomial fit function of third degree, the position-dependent charge identification can be corrected as

$$Q_{TOFD} = \frac{\sqrt{ToT_{PMT1} \cdot ToT_{PMT2}}}{p_0 + p_1 \cdot y + p_2 \cdot y^2 + p_3 \cdot y^3}, \tag{63}$$

where $p_0 - p_3$ are the fitting parameters.

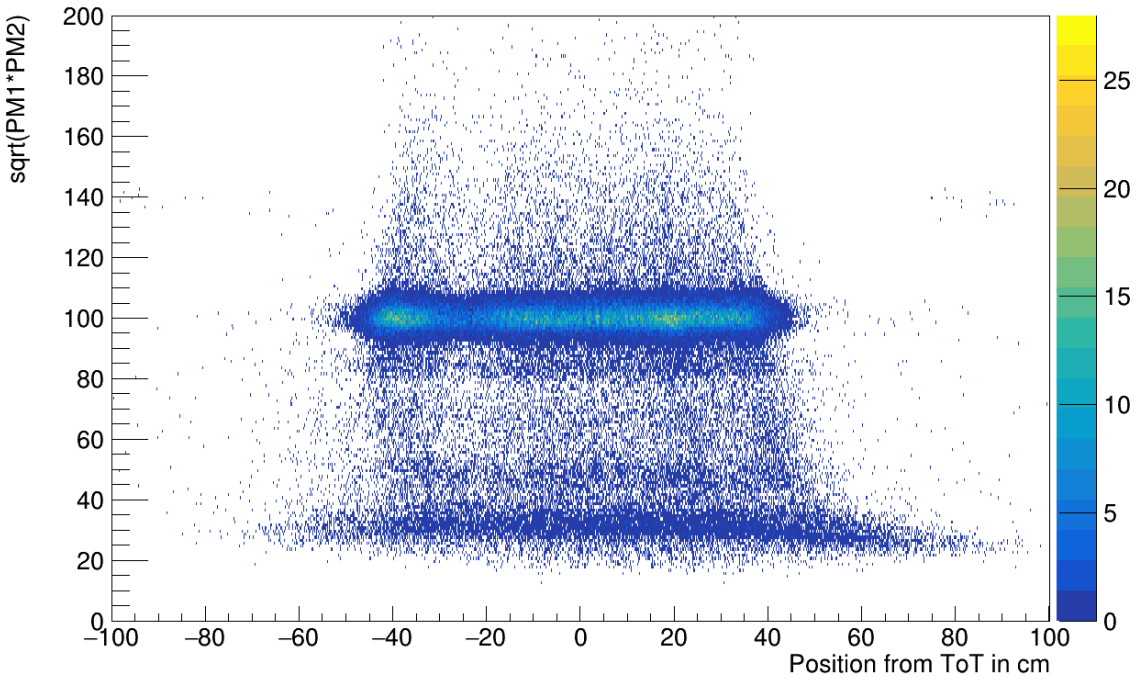

Figure 22: Deposit energy, calculated with sqrt($ToT_{PMT1} \cdot ToT_{PMT2}$), versus vertical hit position for a single bar in a meandering run scanning the full detector area.

In the final step, the energy loss for runs with different target thicknesses is compensated by introducing a parameter set that shifts the peak position to the nominal nuclear charge. The final calibrated charge of TOFD for plane 1 is shown in Fig. 23

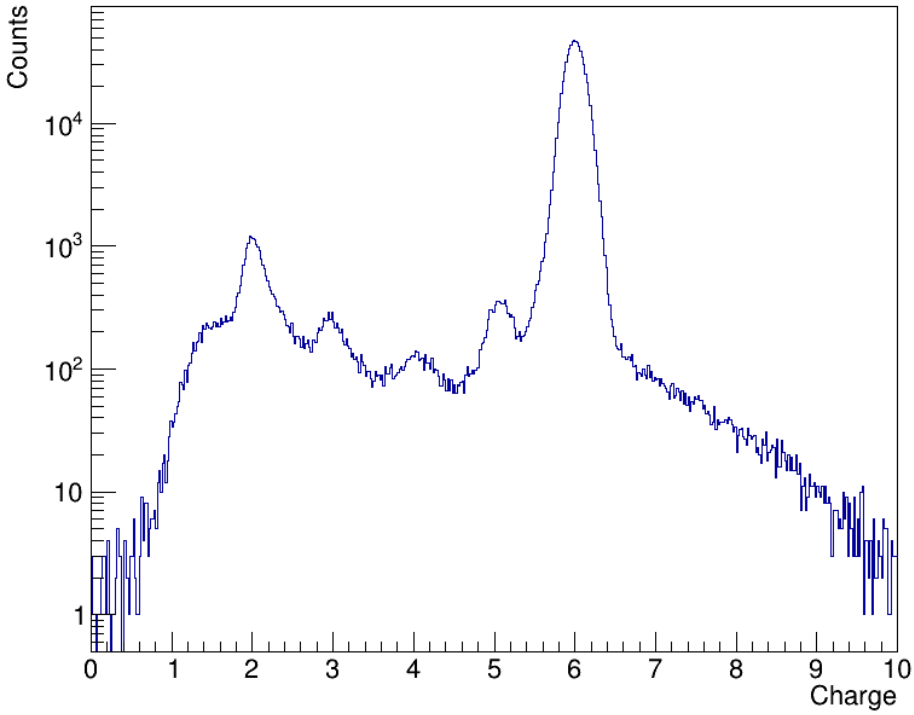

Figure 23: Calibrated nuclear charge for plane 1 of TOFD.

3.6.2 PSP Calibration

The PSP detectors used in the present work are of the type "Micron X5" designed by Micron Semiconductor Ltd [71]. Free charge carriers, produced in the resistive layer on top of each strip by charged particles or ionizing radiation passing the active area of the detector, are split up and collected at both ends. The detector is divided into 32 vertical strips on the front and 32 horizontal strips on the back side, all read out separately on both ends. By summing up the collected charge at both ends, the energy loss and, thus, the nuclear charge of the traverse particle can be determined. The position where the particle was hitting the detector can be calculated as

$$x = \frac{L_{Strip}}{2} \cdot \frac{E_1 - E_2}{E_1 + E_2}, \tag{64}$$

where $E_{1/2}$ are the measured energy at both sides and L_{Stirp} is the length of the strip. For precise position and charge identification, the response of the anodes has to be calibrated. Fig. 24 shows a schematic view of a PSP detector with selected strips. The area of the vertical blue strip is covered by 32 horizontal strips on the backside. Due to the even number of strips, the distance between strip 16 and the bottom anode is the same as between strip 17 and the top anode.

With this geometrical assumption, a set of gain-match parameters for all anodes and strips can be determined in the following way. The measured energy at the top

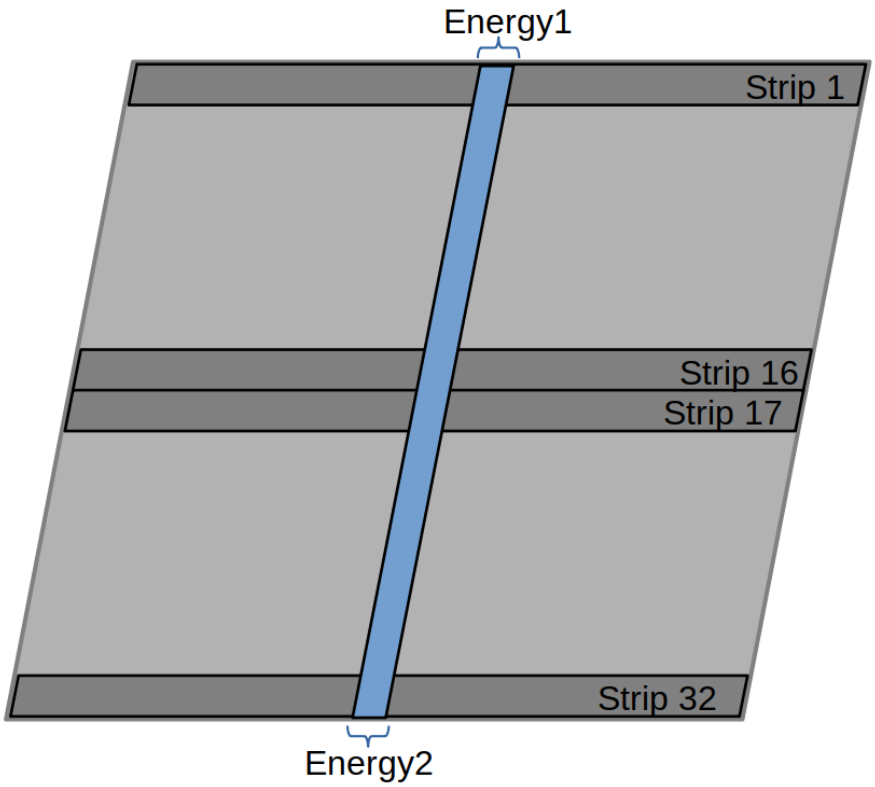

Figure 24: Schematic view of PSP Strips with selected strips highlighted.

anode (E_1) for the vertical strip, on condition that the same particle has passed the horizontal strip 17, has to be equal to E_2 for the same vertical strip, on condition that a particle has passed the horizontal strip 16. This condition can be expressed as

$$E_1^{\text{vert.}}(\text{Hit}^{\text{horz.}}_{\text{Str.17}}) = E_2^{\text{vert.}}(\text{Hit}^{\text{horz.}}_{\text{Str.16}}) \tag{65}$$

The resulting gain-match parameters are determined with a non-focused beam, which illuminates most of the detector area and are normalized to obtain uniform energy values. In the left panel of Fig. 25, the raw strip energy ($E_1 + E_2$) is plotted for the back and front sides. The different diagonals indicate that the response varies for different strips. After applying the gain-match parameters, all front and back side strips' energies are aligned (see right panel of Fig. 25). The resulting position information after gain-matching is shown in both panels of Fig. 26. The left panel shows the calculated horizontal position versus the strip number of the front side. The calculated vertical and horizontal position information are plotted in the right panel.

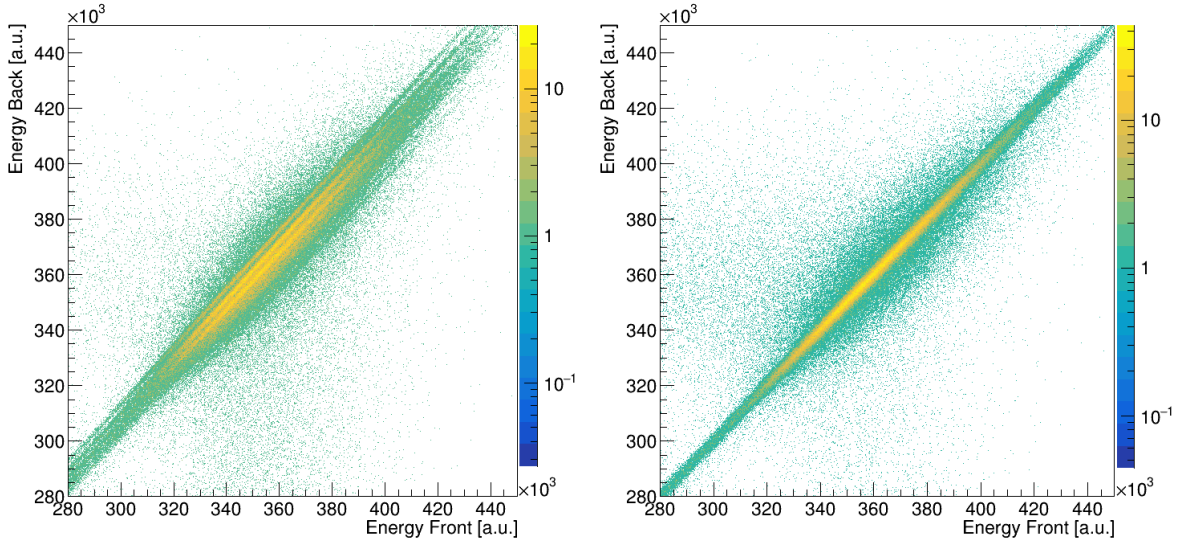

Figure 25: Left panel: Raw strip energy ($E_1 + E_2$) of PSP front side versus back side. Right panel: After applying the gain-match parameters, the front and back side strip energies are aligned.

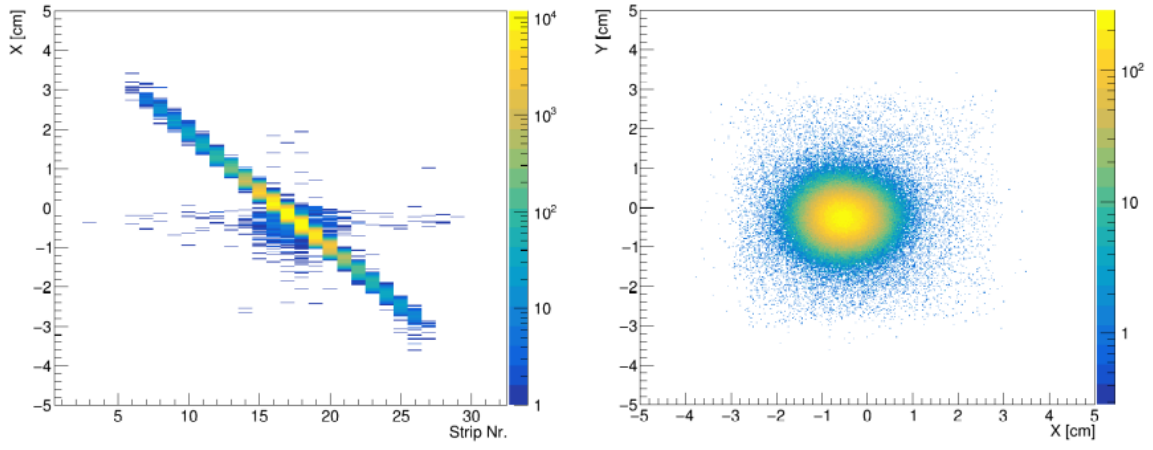

Figure 26: Position information of PSP detector after gain-matching. The left panel shows the calculated horizontal position versus the strip number of the front side. The calculated vertical and horizontal position information are plotted in the right panel.

4 Analysis of Total Interaction Cross Sections

This chapter provides a detailed description of the underlying analysis principle, which is based on the so-called Transmission method [72]. An expression for the total interaction cross-sections is derived, including all relevant quantities that must be extracted from the experimental data. It is explained how these quantities, first and second-order correction factors, and additionally the systematic uncertainties were precisely determined.

4.1 Transmission Measurements

The fundamental idea behind the total reaction cross-section measurement is to determine whether an incoming particle was undergoing a nuclear reaction inside the target material or not. As discussed in Chapter 1 (see Table 1) the total reaction cross section can be separated into an "inelastic scattering" plus an "interaction" part.

$$\sigma_R = \sigma_{inel} + \sigma_I \tag{66}$$

The first term on the left side describes the probability of excitation of the projectile ^{12}C nucleus into a bound state. Whereas "interaction" means that the nucleus changes its identity so at least one nucleon is removed or exchanged. Small momentum transfers in nucleon-nucleon collisions, which could lead to inelastic excitations of the nucleus are considered by the discussed Glauber reaction model. Whereas collective excitations of the nucleus are not included but can be neglected in the case of a low charge number of projectile and target [47]. The inelastic scattering part for ^{12}C+^{12}C collisions gives just a small contribution to the total reaction cross-section at high energies (around 6 mb at 200 MeV/nucleon beam energy according to ref. [57]) and was not identified in this experiment. Therefore, in the presented energy regime the total reaction cross section σ_{R} can be approximated with the total interaction cross section σ_{I}, the quantity which was measured in this work.

In order to ascertain whether a particle has changed its identity, a common starting point is the definition of the so-called Survival-Probability, which reads as

$$\mathrm{P_{surv.}} = \frac{\mathrm{N_2}}{\mathrm{N_1}} = \mathrm{e}^{-\mathrm{N_t}\cdot\sigma_{\mathrm{I}}}, \tag{67}$$

where $\mathrm{N_t}$ is the number of scattering centers per unit area in the target material (see Section 3.5) and σ_{I} is the total interaction cross-section. This equation describes the

ratio of non-reacted nuclei after the target (N_2) to all incoming nuclei (N_1). In the case of a target-out run (empty run), the argument of the exponential function becomes zero, and thus, the probability for a particle to survive is 100 %.
This expression has to be extended since the experimental setup does not only consist of a target but also several in-beam detectors. To exclude reactions of the projectile that occur within the setup material, the Survival-Probability of a target-in run has to be divided by the same for a target-out or empty run:

$$\frac{R_i}{R_o} = \frac{N_2^i/N_1^i}{N_2^o/N_1^o} = e^{-N_t \cdot \sigma_I} \tag{68}$$

Solving this equation for the interaction cross-section σ_I leads to the expression for a so-called Transmission measurement:

$$\sigma_I = -\frac{1}{N_t} \ln\left(\frac{R_i}{R_o}\right), \tag{69}$$

where $R_{i/o}$ are the ratios of the number of non-interacted nuclei after the target $N_2^{i/o}$ divided by the number of incoming nuclei $N_1^{i/o}$, for a target-in (i) and a target-out (o) run. These quantities have to be measured precisely in the experiment to calculate the total interaction cross-section.

Number of scattering centers N_t
The number of scattering centers per unit area is a target-specific constant (see Section 3.5). For all three carbon targets, this quantity was determined by measuring the target thickness in the beam direction. N_t and the correspondent uncertainty were calculated using the volume density given by the manufacturer and were listed in Table 2.

Number of incident nuclei N_1
This number has to be identified with detectors upstream of the target. A strict event selection in front of the target makes it possible to ensure ideal experiment conditions without biasing the final result. The goal is to select single ^{12}C particles hitting the target center. Details are discussed in the following Section 4.2 "Event Selection".

Number of non-reacted particles N_2
For each incoming particle, a clear signature must be recorded whether it has reacted within the target material. So, it is crucial to know the time- and rate-dependent efficiency of the detectors precisely. The strategy in the presented analysis is to minimize the systematic uncertainties by reducing the number of used detectors. For the 1st

order, just one detector, the TOFD time-of-flight wall, was used to identify all carbon isotopes within the acceptance at the very end of the setup (see Section 4.4).
For second-order corrections, the information of the PSP and Fiber detectors was implemented. By measuring the nuclear charge in the first step, this number also includes other carbon isotopes than ^{12}C. So, in the second step, the ratio of ^{12}C isotopes compared to all carbon isotopes within the acceptance window has to be identified for each run separately. This ratio is used as an isotope correction factor. (see Section 4.5.2)
In addition, it is essential to determine the geometrical acceptance of the TOFD detector for ^{12}C isotopes. Due to time constraints, the magnetic field of GLAD was chosen to be constant for all runs with specific beam energy and targets of different materials and thicknesses. Therefore, the geometrical acceptance for a particular isotope varies from run to run. (see Section 4.5.3)

4.2 Event Selection - Identification of incoming ^{12}C

The goal of the event selection is to end up with a "single particle per event" situation to ensure that the data is not corrupted by high multiplicities or overflow events that are not reproducing a reliable physical signal. This allows to assume no dead time correction for a busy DAQ and no signal alteration of the different detectors by particle interactions overlapping in time.
The event selection is done with detectors upstream of the target/reaction area, namely the LOS, ROLU, and PSP1 detectors. The significant advantage is that a particle selection upstream of the target area does not introduce any systematic bias if not changed between full and empty target measurements.
Several conditions must be fulfilled to accept an event by the event selection. The first one is the so-called TPat=1 condition. The TPat information is a flag for each event, indicating a specific reaction trigger; e.g., TPat=1 is the minimum bias trigger. This means that, on the one hand, the event was recorded during an "on-spill period". Additionally, this flag indicates that LOS has recorded at least one hit, and ROLU has not seen a signal from a particle passing in a time window of 4 μs. This situation is schematically illustrated for a single spill in the first two rows of Fig. 27. The red-shaped area indicates hits in LOS, which were recorded during an off-spill period. Whereas the green highlighted hits pass the TPat=1 condition.

Due to the spill structure of the delivered beam, it is possible to end up with higher hit multiplicities than 1 in LOS within the time window of the event building (4 μs), even at relatively low beam rates. So, in the next step, it is necessary to check the number of identified particles within one event (multiplicity) by LOS (see row 3 in Fig. 27). To

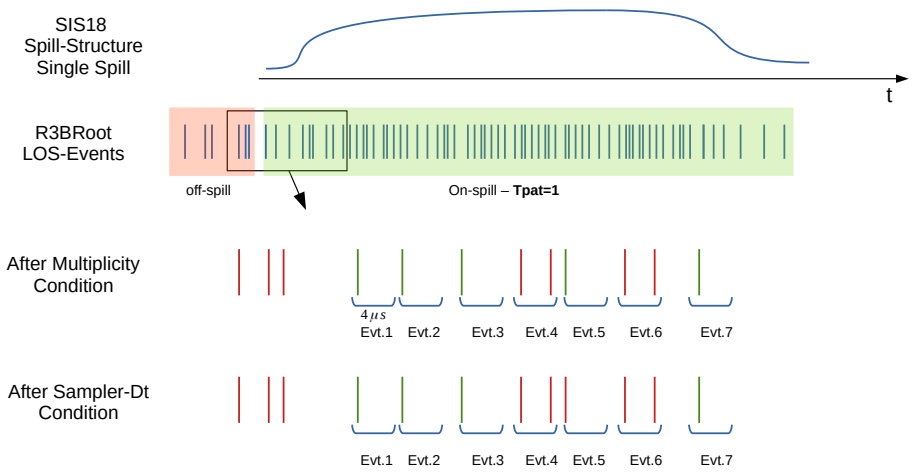

Figure 27: Schematic illustration of a single spill coming from SIS18. Blue lines indicate individual registered hits in the LOS detector. The red- and green-shaped areas highlight hits within an off- or on-spill period, respectively. The third row shows a zoomed selection of hits, where green lines represent hits that fulfill the condition of TPat=1 and a multiplicity=1 within a single event. After the condition of a time difference of 4 μs between the previous and following particles, Evt.5 was excluded in row 4.

ensure that LOS just measured a single particle within a time window of 4 μs, only events with a multiplicity of 1 in the Hit-Level of the LOS are selected. As an additional validation for the position- and charge-identification of LOS, a multiplicity of 8 is demanded on the Mapped-Level. This indicates that all 8 photomultiplier tubes of the LOS detector have provided a valid signal.
The next step is to identify the charge of the incoming particle (see Fig. 29). Besides the charge identification, LOS can also measure the XY position by comparing the time difference of the signals of the 8 photomultipliers (see Fig. 28). Choosing a circular acceptance area with a radius of 2 cm, together with the "not ROLU" condition, ensures that the single particle within the event has no large offset with respect to the beamline and, therefore, is focused on the target area.

In the last step, the time difference between particles before and after the selected event is checked. If this time difference is too small, these particles could cause overflows in the remaining systems. A multi-hit-TDC registers the hit-time of all particles passing the start detector, even for those that are not accepted as triggers for the remaining setup or came before the start trigger. By subtracting subsequently the hit-time of these events, it is possible to exclude events with particles that have a smaller time difference than 4 μs to the previous or following particle (see row 4 in Fig. 27 - Evt.5

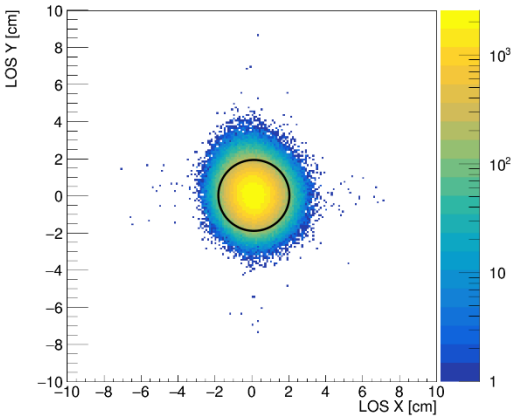

Figure 28: LOS XY beamspot

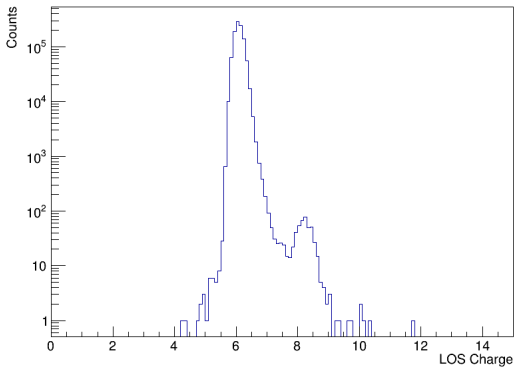

Figure 29: Measured Charge with LOS

was excluded since the time difference between the second hit in Evt.4 and the hit in Evt.5 is smaller than 4 μs).
All used conditions for the event selection are summarized in the following.

Condition	Description
TPat=1	On-spill event, LOS-notROLU
LOSMulti=1	Single particle registered by LOS per event
LOSQ=6	Measured particle charge = 6
LOSBeamspot	Particle hits LOS within a central region of 2cm diameter
Sampler	Δt between previous and following particles $>$ 4 μs

The number of incoming ^{12}C particles for all different beam energy and target combinations after the event selection are listed in Table 3.

N_1	400 MeV/nucleon	550 MeV/nucleon	650 MeV/nucleon	800 MeV/nucleon	1000 MeV/nucleon
Empty	1652117	1231433	1387134	817407	1518466
thin	1622938	622347	1281351	—	808247
medium	1619056	874350	625681	757914	733862
thick	1566584	1045329	1264460	765840	1341165

Table 3: Number of incoming ^{12}C particles for each beam energy and target after the event selection.

4.3 Identification of non-reacted ^{12}C

The total interaction cross-section is defined in this analysis with the probability that the incoming ^{12}C nucleus changes its identity. Therefore, it is sufficient to identify the number of survived ^{12}C after the target. As described in Chapter 4.1 the central quantity is the number of all carbon isotopes identified with the TOFD detector at the very end of the setup. Most plots in this chapter were taken from a run with 400 MeV/nucleon beam energy combined with the medium (10.793 mm) carbon target.

4.4 Carbon Identification with TOFD

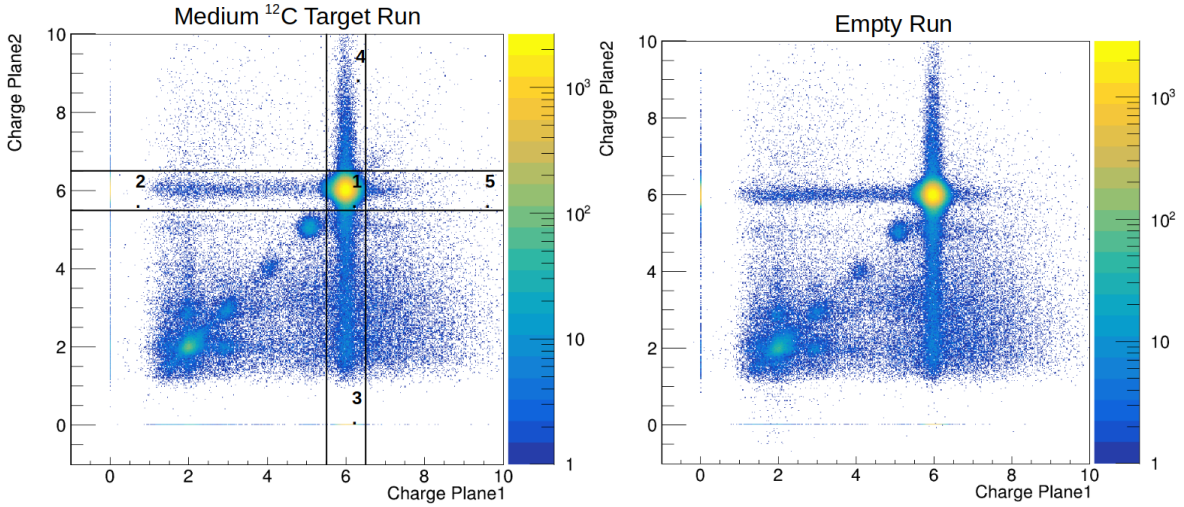

Figure 30: Measured charge of Plane 1 of TOFD versus Plane 2. (400 MeV/nucleon ^{12}C Beam - left panel: medium ^{12}C target - right panel: empty target run)

Fig. 30 shows the identified charge of Plane 1 versus Plane 2 - in the left panel for a run with the medium ^{12}C target and as a comparison in the right panel for an empty target run. Data points on the diagonal indicate particles where both planes have identified the same nuclear charge beginning from helium up to the prominent carbon spot at Q=6 (see region 1). Besides the consistent charge identification on the diagonal, vertical and horizontal bands starting from the carbon region are visible (regions 2 - 5). The part of the bands where one plane measured Q=6 but the other planes measured a smaller charge or did not register any hit (Q=0) - regions 2 and 3 - originates from the design of the TOFD detector. Particles, e.g., hit a paddle of Plane 1 at the edge and deposit just a fraction of the nominal energy within the detector or even completely go through the slit between two paddles. In this case, the particle will go straight into the central region of a paddle of Plane 2 due to the overlapping design. Depending on the amount of material the particle went through during such a graze shot, the energy loss

has continuous values which results in the band shape in the charge reconstruction. The more pronounced vertical band also has additional contributions to higher charges and a stronger contribution close to the Q=6 spot (regions 4 and 5). In both cases, the particle arrives as carbon (Q=6) at Plane 1 and reacts within the scintillator material. Due to this reaction, the particle might change its charge or velocity or even create secondary particles passing at least a part of the plane. Depending on the channel, Plane 2 measures a smaller or larger energy loss. Fig. 31 illustrates a schematic overview of the different reaction mechanisms within Plane 1 and 2 of TOFD.

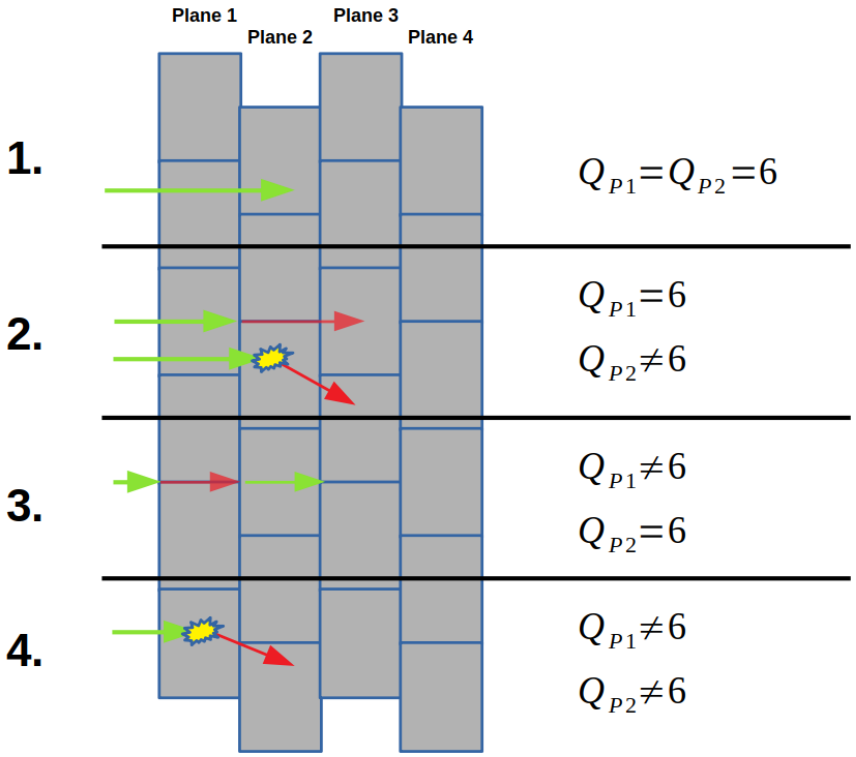

Figure 31: Schematic overview of the different reaction positions within the TOFD detector. In the first row, the carbon particle passes both planes in a central region of the correspondent bar - both planes have measured a charge Q=6. In the second row, Plane 2 has not identified a carbon isotope in contrast to Plane 1 due to a reaction in the detector material or by hitting the gap between two bars. If the particle passes the slit between two bars of Plane 1, it will go straight into the overlapping bar of Plane 2 (see row 3). Carbon particles reacting within the detector material of Plane 1 will not be identified with charge Q=6 by either Plane 1 or Plane 2 (see row 4).

For the sake of completeness, it is necessary to mention that carbon particles reacting in the first layers of the paddle material might not be identified as Q=6 by either Plane

1 or Plane 2. But this can be described as a reaction within the whole setup and thus is considered by the Transmission method and therefore excluded by the relative measurement between target runs normalized to empty runs.

The condition for an identified carbon isotope with the TOFD detector ($N_{Q=6}^{TOFD}$) is fulfilled if either Plane 1 or Plane 2 has measured a particle with charge 6 ± 0.5. By this, the dependency on the local gap size between bars and the effect of different incident angles is canceled. In addition to that, with this condition, even the tails of the Gaussian distributed carbon spot are considered within the cut, while the influence of the detector resolution on the result is minimized.
Table 4 lists the number of identified carbon isotopes with TOFD for all beam and target combinations.

$N_{Q=6}^{TOFD}$	400 MeV/nucleon	550 MeV/nucleon	650 MeV/nucleon	800 MeV/nucleon	1000 MeV/nucleon
Empty	1588948	1182554	1330271	783938	1453606
thin	1498013	573647	1179167	—	741459
medium	1432954	773474	552932	668904	645902
thick	1085472	846197	1024507	619190	1081477

Table 4: Number of identified carbon particles with TOFD for each beam energy and target after the event selection.

4.4.1 1st Order Correction - Carbon Identification Efficiency

Due to the overlapping design of TOFD, a geometrical acceptance within the setup aperture of 100% is assumed. To validate the efficiency of the carbon identification, TOFD can be virtually divided into two identical separate detectors:

- Detector 1: Plane 1 & Plane 2
- Detector 2: Plane 3 & Plane 4

If the later or more downstream Detector 2 has registered a particle with charge $= 6 \pm 0.5$ in both planes, Detector 1 should have measured the same charge in either one of its planes. Fig. 32 shows the measured charges of Plane 1 and Plane 2 under the condition that Plane 3 and Plane 4 have measured a charge of 6 ± 0.5. Using this cross-check, it is possible to define an efficiency factor for the carbon identification for each run individually:

$$\epsilon_{Q=6}^{TOFD} = \frac{N(P1_{Q=6} \cup P2_{Q=6} | P3_{Q=6} \cap P4_{Q=6})}{N(P3_{Q=6} \cap P4_{Q=6})} \tag{70}$$

The number of identified carbon isotopes has to be divided by this efficiency factor to correct for the number of carbon isotopes reaching the TOFD detector

$$N_{Q=6} = \frac{N_{Q=6}^{TOFD}}{\epsilon_{Q=6}^{TOFD}} \tag{71}$$

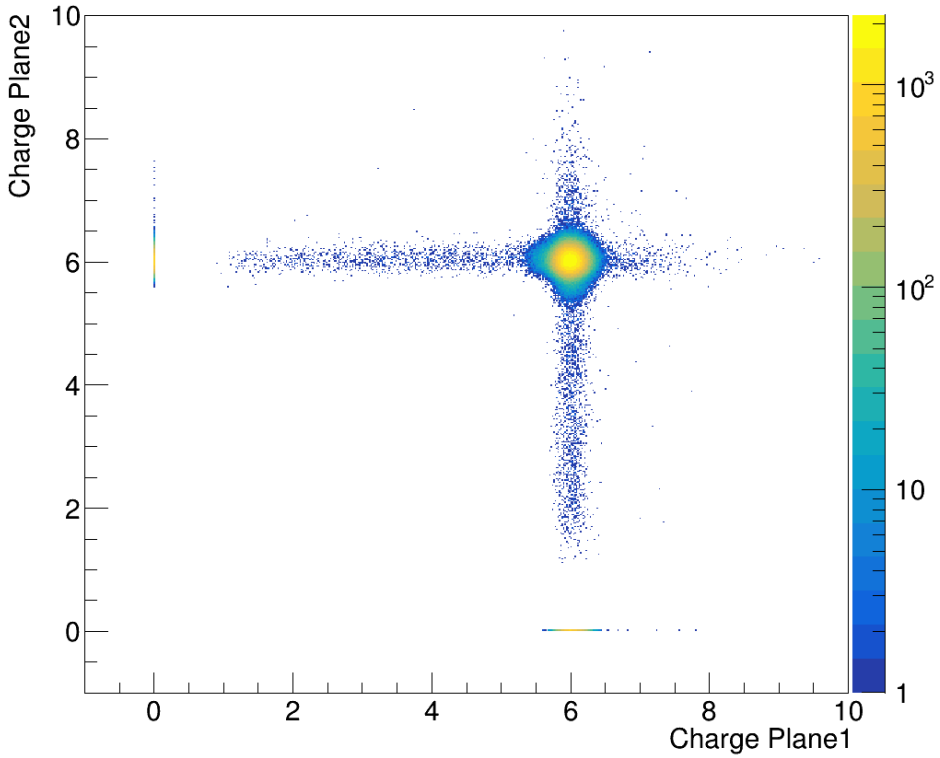

Figure 32: Measured charge of Plane1 of TOFD versus Plane2 under the condition that Plane3 and Plane 4 have measured a charge of 6 ± 0.5.

4.4.2 Sensitivity of Carbon Identification

With the two-dimensional condition that either Plane 1 or Plane 2 has identified a particle with charge 6 ± 0.5 (which corresponds to region 1-5 in Fig. 30), most of the 2D Gaussian distribution is considered. The ± 0.5 gate is most sensitive to the tails of regions 2-5, which have much less statistics. To correct for the sensitivity of the gate, the efficiency correction factor is used. In Fig. 33, the total interaction cross section is plotted for charge gate sizes ranging from ± 0.3 to ± 0.6. In red without any correction factor and in green including the efficiency correction factor.

The sensitivity of the gate size is clearly visible in the red data, where no correction factor is used. After applying the efficiency correction, this effect is compensated. Therefore, the efficiency-corrected charge identification is independent of the gate size. The fluctuations between $\Delta Q = \pm 0.45$ and ± 0.55 are considered in the systematic uncertainty for this quantity.

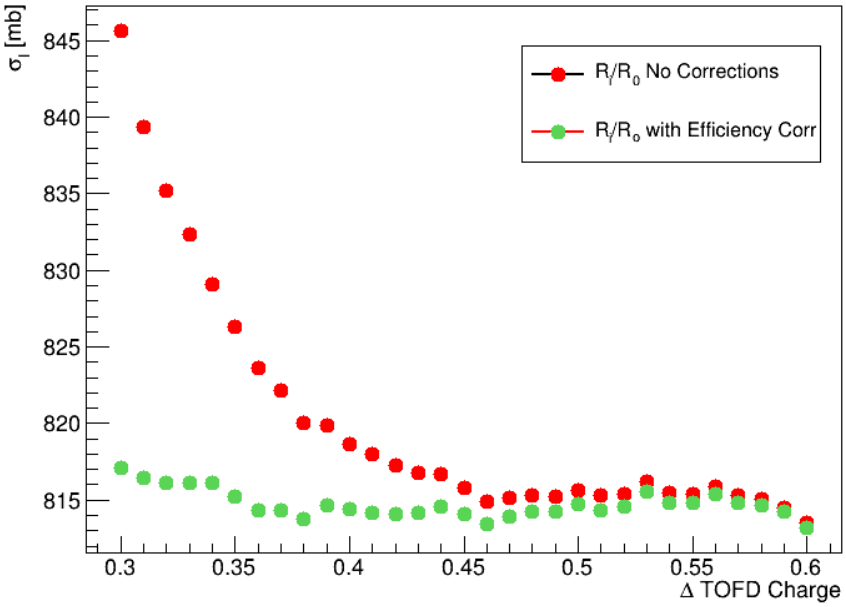

Figure 33: Total interaction cross section for different charge gate sizes, ranging from ± 0.3 to ± 0.6, for the carbon identification with TOFD. The red data points illustrate the cross section without any correction factor. The efficiency correction factor is included in the green data.

4.5 2nd Order Correction Factors

After identifying all carbon isotopes in the 1st order only with TOFD, the capability of the whole setup was used to determine the different corrections needed to determine the number of transmitted ^{12}C more precisely. Eq. (71) shows the efficiency corrected expression for the carbon identification or particles with charge 6 at the very end of the setup with the TOFD detector. This number also includes different carbon isotopes than ^{12}C within the geometrical acceptance window of TOFD. Therefore, it is necessary to identify the ratio of ^{12}C compared to all identified carbon isotopes $N_{Q=6}^{TOFD}$. Fig. 34 shows a schematic sketch of the trajectories of two different carbon isotopes entering a magnetic field (blue-shaped area) at the same position. Both isotopes are getting deflected with a different radius due to their different mass-to-charge ratio $\frac{A}{q}$ according to the well-known relation:

$$B\rho = \frac{A}{q} \cdot \gamma \cdot \beta \cdot c \tag{72}$$

where B is the magnetic field strength, ρ is the bending radius, c is the speed of light in vacuum, γ is the Lorentz-Factor and β is relativistic velocity. In the sketched example of ^{12}C and ^{11}C with the same velocity and a constant magnetic field, both particles will get deflected with a different bending radius ρ and thus end up at different positions after the magnetic field.
According to Eq. (72), it is necessary to measure the positions and angles before and after GLAD, as well as the velocity of the particles, for a full identification. For the separation of carbon isotopes, the velocity can be considered constant due to the approximately same energy loss within the setup material. Additionally, in the case of light nuclei like ^{11}C and ^{12}C, the mass-to-charge ratio difference is around 10%. Therefore, to identify the mass of a carbon particle entering the magnetic field of GLAD, which is finally detected by TOFD, it is sufficient to measure the X position in front and after GLAD. This was done using the PSP detectors after the target area and in front of the GLAD entrance and the Fiber detectors in the detector chamber after GLAD.

4.5.1 Determination of X-Positions before and after GLAD

Both systems, PSP and Fiber detectors, have a high segmentation. Typically, several segments share a signal above the threshold, which could result in hit multiplicities larger than 1, as shown in Fig. 35. The first step is to define conditions that exclude background signals and identify the beam particle signal in both data sets.

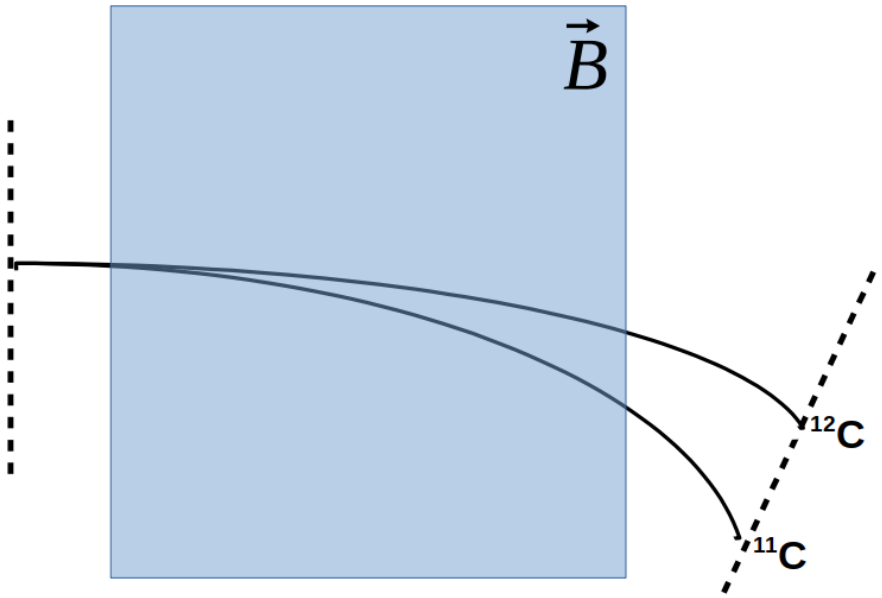

Figure 34: This figure illustrates the trajectories of two different carbon isotopes entering a magnetic field (blue-shaped area) at the same position. Since both particles have the same velocity, they will end up at different positions after the magnetic field due to their different mass, resulting in a different bending radius.

PSP Detector

The two upper panels in Fig. 35 show the multiplicity of hits with an energy deposit within PSP2 or PSP3, which corresponds to a particle with charge 6 (see Fig. 36). Since the event selection, described before, ensures that just a single carbon particle enters the setup within a 4 μs event, these high multiplicities or "ghost-carbon-events" cannot be explained regarding spill-structure effects.

The left panel in Fig. 37 shows the correlation between the measured X position of PSP2 and PSP3 for "Q=6"-Hits for all possible combinations and no restrictions on the multiplicity. The right panel shows the same correlation but for events where PSP2 and PSP3 have a "Q=6"-Hit-Multiplicity of 1. PSPs are double-sided silicon strip detectors with 32 vertical strips on the front and 32 horizontal strips on the back. All strips have a width of 0.3 cm and a length of 9.57 cm and are read out on both ends of the strip. The X position of an individual hit was calculated in the case of the horizontal back-strips with the following formula:

$$X_{\text{horiz.Strip}} = \frac{E_1 - E_2}{E_1 + E_2} \cdot \frac{9.57\text{cm}}{2} \tag{73}$$

, where E_1 and E_2 are the gain-matched signal amplitudes at both ends of the strip. If the back-side has not seen a Q=6-hit, it could be caused by a so-called interstrip

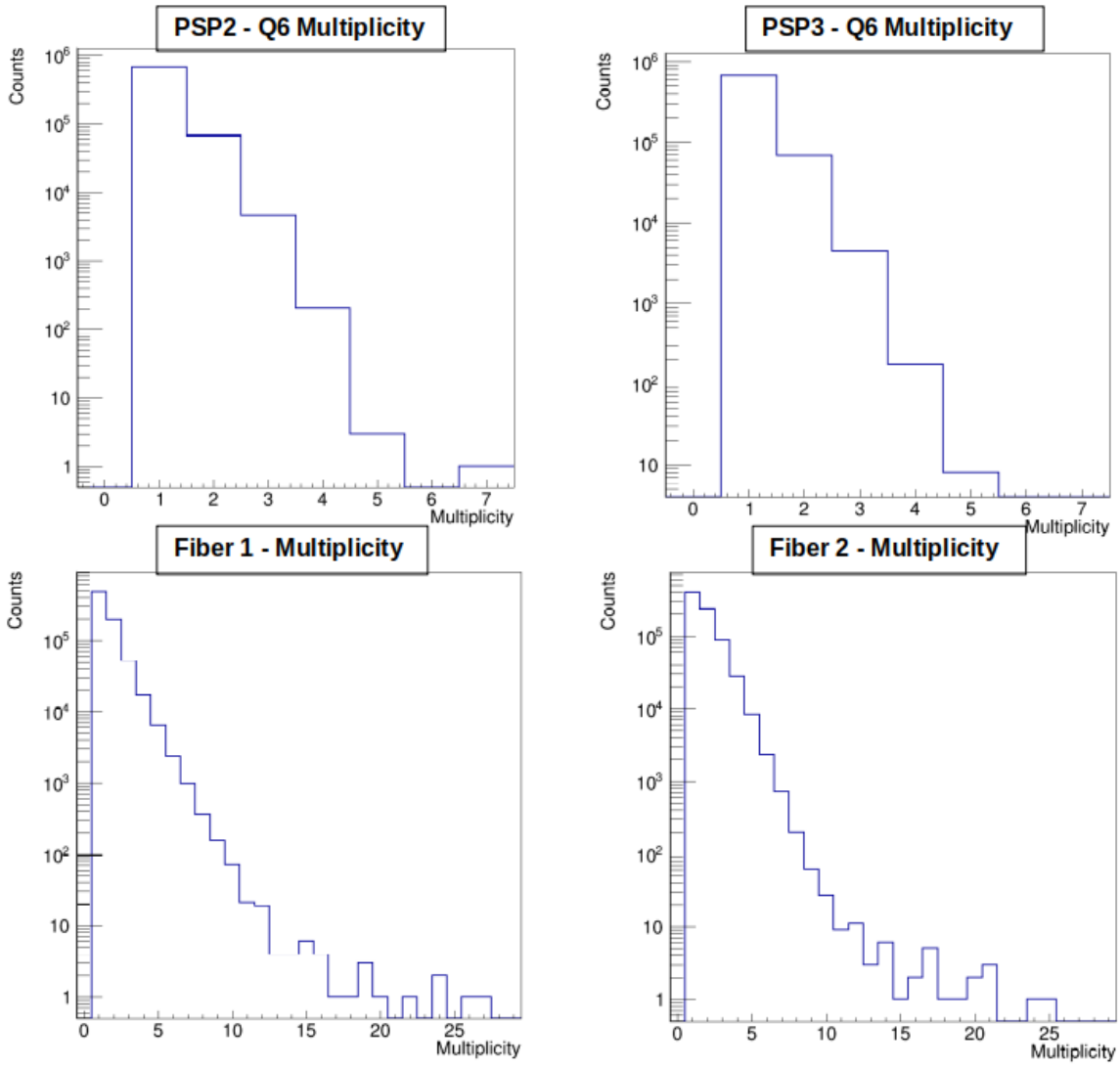

Figure 35: Both upper panels show the multiplicity of hits with an energy loss within PSP2 or PSP3 corresponding to an identified particle with charge 6, respectively. Both lower panels show the hit multiplicity of Fiber 1 and Fiber 2, respectively.

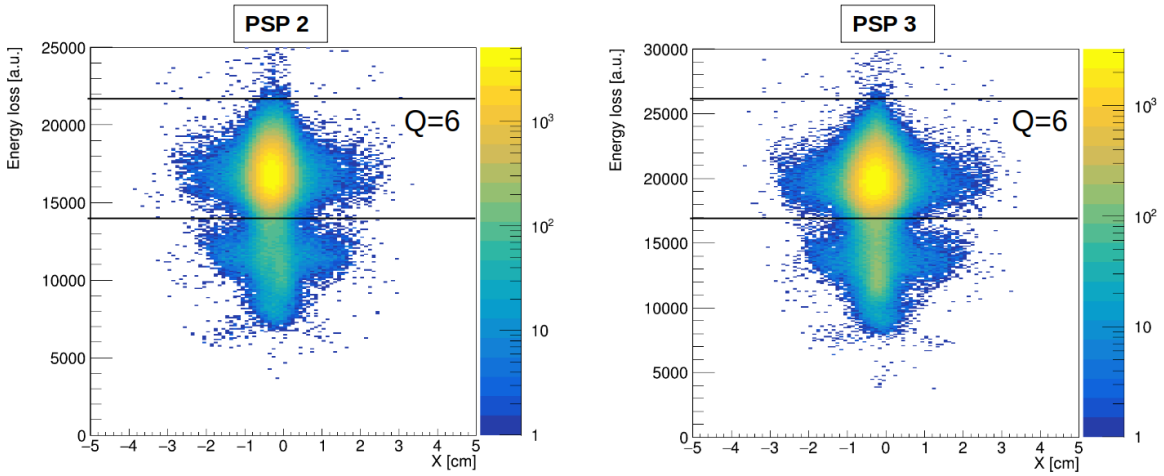

Figure 36: Both panels show the energy loss in arbitrary units in PSP2 and PSP3 versus the measured X position respectively. The main spot at around 18000 and 20000 indicate carbon particles. Whereas the spot at around 12000 and 14000 correspond to boron particles.

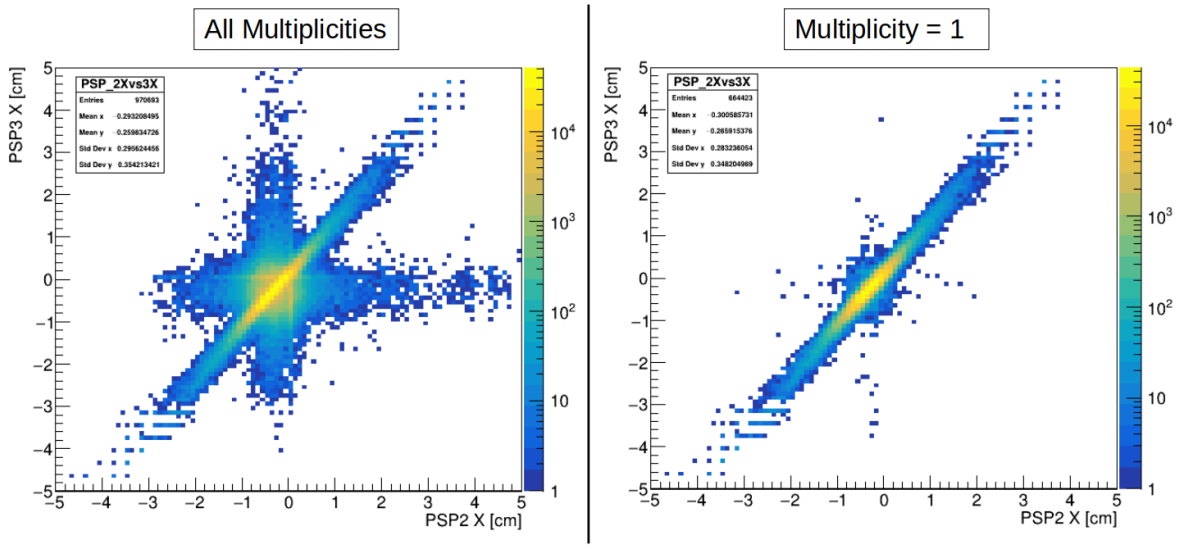

Figure 37: Both panels show the correlation between the measured X positions of PSP2 and PSP3 for hits with an energy loss equal to particles with charge 6. The left panel shows every possible combination of "Q=6"-Hits within an event and no restriction on the multiplicity of these hits. Whereas the panel on the right shows the position correlation just if both detectors have a "Q=6"-Hit-multiplicity of 1.

event, where the energy loss for one strip is below the threshold. Another possible explanation is if the particle hits a strip near one end, the energy at the other end is below the threshold. In this case, the hit is not registered due to missing energy information on one side of the strip. These effects could be compensated by checking the front layer for a Q=6-hit. The X position of a vertical strip can be calculated with the strip number as

$$X_{\text{vertical.Strip}} = (0.3\text{cm} \cdot \text{StripNo.}) - \frac{9.57\text{cm}}{2}, \tag{74}$$

with StripNo. $\in [0; 32]$. Such an X position measurement using vertical strips gives discrete values depending on the strip number which can be seen at the edges of the diagonal in Fig. 37.
The comparison of both correlation plots in Fig. 37 illustrates that the high multiplicities include uncorrelated "ghost"-hits, which would result in a wrong position determination for the mass identification.
To make a reliable position measurement with the PSP detectors in front of the magnetic field of GLAD, the following conditions were used:

1. Carbon (Q=6 - see Fig. 36) hit in PSP2 and PSP3 (back or front layer)

2. Correlated X position of PSP2 with PSP3 (see Fig. 37)

Fiber Detector

Both lower panels in Fig. 35 show the hit multiplicities in Fiber 1 and Fiber 2 without any condition but the already discussed event selection. The fact that these multiplicities have values larger than 1 can be understood by considering the design of the fiber detectors. The scintillating material is sensitive to cross-talk and background radiation in the experimental cave. But also, the coupling of fibers in bunches and pairs within the MAPMT and SAPMT creates a connection, which results in cross-talk and light sharing.
The left panel of Fig. 38 shows all possible combinations of the X positions of Fiber 1 and Fiber 2. The already mentioned background events can be seen as uncorrelated data points. The first reasonable condition for the correct identification of the X position of the remaining nucleus is a position correlation, which can be seen in the right panel of Fig. 38. The condition was performed by defining two linear equations as an upper and lower limit to exclude background events. On the other hand, these limits must be chosen large enough to include particles passing both detectors with a large angle with respect to the 18-degree line.

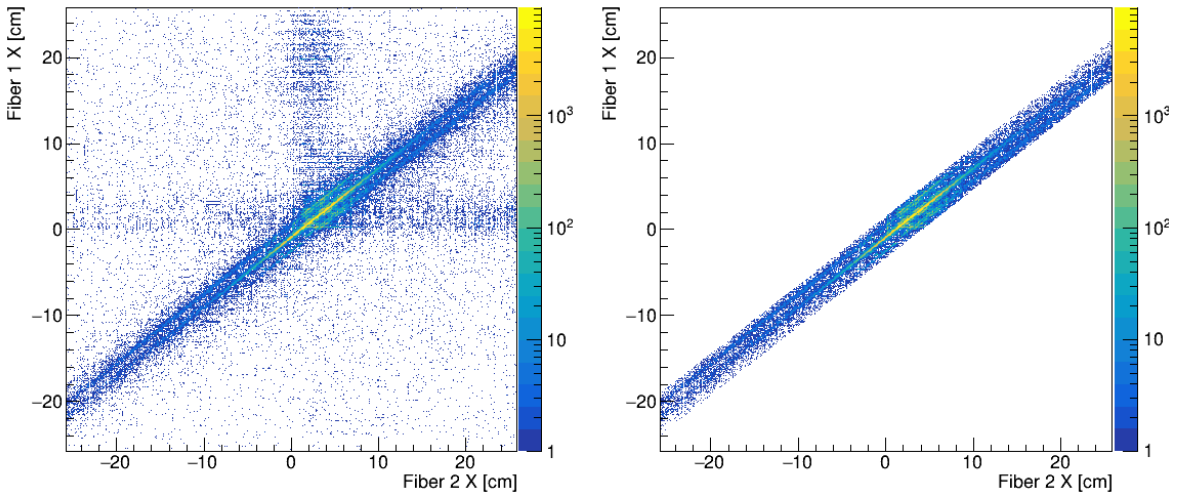

Figure 38: Both panels show the correlation between the measured X positions of Fiber 1 and Fiber 2.

For the remaining position-correlated hits, it is possible to ask for a time correlation between the measured hit and the minimum bias trigger coming from the start detector (see Fig. 39).

All figures show the representative example of a run where a 400 MeV/nucleon ^{12}C beam hits the medium ^{12}C target. In this case, scattering effects inside the target and setup material are broadening the beam significantly, as shown in Fig. 38 where the more downstream Fiber 2 is already fully covered by the beam while Fiber 1 is not. In this case, it is necessary to include the missing beam edge distribution of Fiber 1. Even though a position correlation with Fiber 2 is not possible for this part.
To summarize the situation for the position identification after the magnetic field of GLAD, the following conditions were used:

1. Position correlation between Fiber 1 and Fiber 2, which excludes most background radiation but includes large scattering angles (see Fig. 38) of carbon fragments

2. Time correlation with the minimum bias trigger coming from the LOS detector (see Fig. 39)

3. Include edge distribution of particles that exceed the active area of Fiber 2

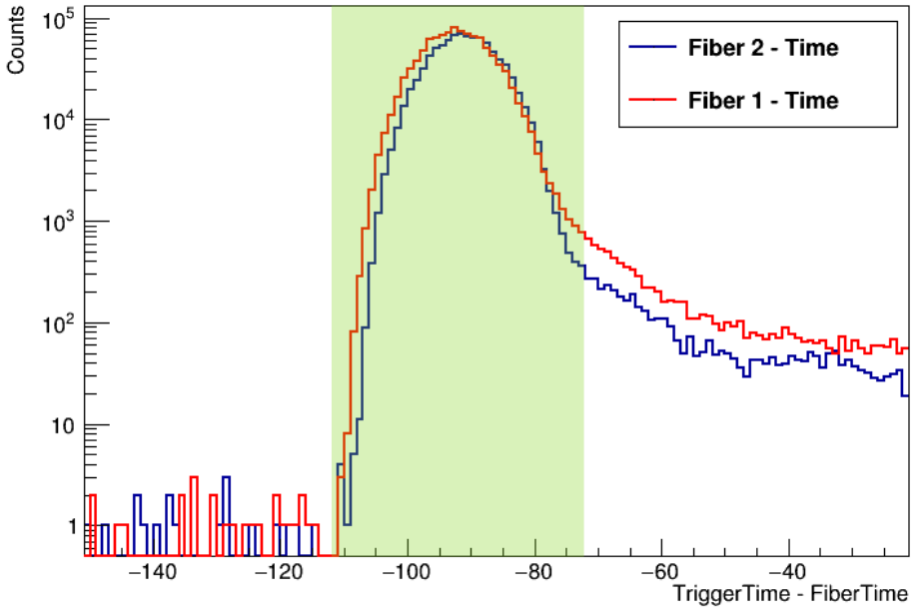

Figure 39: Time difference between the minimum bias Trigger from the start detector and the Hit-Time of Fiber 1 (red) and Fiber 2 (blue), respectively.

4.5.2 The Isotope Correction Factor

According to the discussed hit selection of the previous section, a selection of reliable hits and their corresponding X position from PSP3 and Fiber 1 were chosen. The left panel of Fig. 40 shows all possible combinations of both horizontal position information. The two diagonal distributions represent the ^{12}C and ^{11}C isotopes respectively. The broad horizontal band (around PSP3X = 0 - 1 cm) indicates the remaining background events in the Fiber 1 data and particles scattered in the setup material between PSP3 and Fiber 1. By applying the condition that TOFD has registered a particle with charge 6 ± 0.5, the picture evolves as shown in the right panel of Fig. 40 where the hit with the highest energy loss was chosen.

In this plot, it is visible that most of the ^{11}C distribution is bent to larger angles due to their lower mass and gets deflected apart the 18 degrees line and thus does not reach the geometrical acceptance window of the TOFD detector at the very end of the setup. The ratio of the ^{12}C nuclei within the carbon data of TOFD can be estimated by defining again an upper and lower geometrical limit which divides the ^{12}C from the ^{11}C distribution. The number of ^{12}C isotopes $N_{^{12}C}^{TOFD,PSP,Fib}$ can be defined by checking whether a particle is fulfilling the condition of the defined position distribution. As indicated, this number depends not only on the time- and rate-dependent efficiency of TOFD but also on the same of PSP and Fiber detectors. By defining the following

ratio as

$$R_{^{12}C} = \frac{N_{^{12}C}^{TOFD,PSP,Fib}}{N_{Q6}^{TOFD,PSP,Fib}} = \frac{N_{^{12}C} \cdot \epsilon_{TOFD,PSP,Fib}}{N_{Q6} \cdot \epsilon_{TOFD,PSP,Fib}} = \frac{N_{^{12}C}}{N_{Q6}}, \tag{75}$$

where N_{Q6} is the total number of events in the right panel of Fig. 40, two subsets of the same data set are divided, where both depend on exactly the same efficiencies. Therefore, $R_{^{12}C}$ is independent of the rate- and time-dependent efficiency of the PSP and Fiber detectors.

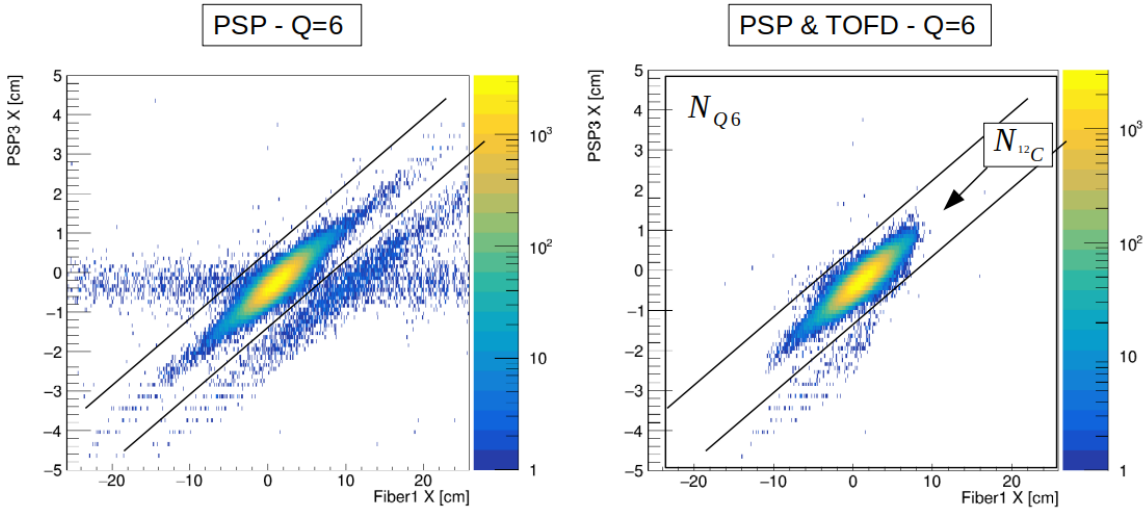

Figure 40: X position of PSP3 in front of GLAD versus X position of Fiber 1 after the magnetic field of GLAD. The shown X positions were chosen under the discussed conditions of the previous section. The right panel shows the correlated horizontal positions under the additional conditions that TOFD registered a particle with charge 6 ± 0.5 in the same event.

Table 5 shows the calculated ratios of ^{12}C isotopes compared to all identified carbon isotopes within the acceptance window of TOFD for all given beam energies and target thicknesses. The listed uncertainties were deduced from the uncertainty of a Gaussian fit on the ^{11}C distribution.

To correct the number of identified carbon isotopes (see Eq. (71)) for other isotopes than ^{12}C, this factor has to be multiplied in the following way:

$$N_{^{12}C} = N_{Q=6} \cdot R_{^{12}C} = \frac{N_{Q=6}^{TOFD}}{\epsilon_{Q=6}^{TOFD}} \cdot R_{^{12}C} \tag{76}$$

$R_{^{12}C}$	400 MeV/nucleon	550 MeV/nucleon	650 MeV/nucleon	800 MeV/nucleon	1000 MeV/nucleon
Empty	0.99998(1)	0.99996(2)	0.99997(2)	0.99997(1)	0.99998(1)
thin	0.99962(3)	0.99948(2)	0.99943(2)	—	0.99975(2)
medium	0.99945(1)	0.99926(2)	0.99920(1)	0.99930(3)	0.99960(3)
thick	0.99938(1)	0.99922(1)	0.99908(2)	0.99921(2)	0.99945(3)

Table 5: Ratio of ^{12}C isotopes compared to all carbon isotopes identified with the TOFD detector for all beam energy and target combinations together with the respective systematic uncertainties.

4.5.3 Estimation of Geometrical Acceptance

The effect of the limited geometrical acceptance of the experimental setup can already be seen in Fig. 40. After applying the TOFD-charge condition on the data set, the edges of the ^{12}C distribution are cut off in the right panel. This effect becomes more apparent by looking at the XY beam position using Fiber 3 and Fiber 4, which were installed after the exit window of the vacuum pipe and right in front of TOFD. Fig. 41 shows the carbon beam position for an initial beam energy of 400 MeV/nucleon and different targets: Empty (panel a), thin carbon (panel b), medium carbon (panel c), and thick carbon (panel d). Due to the different energy loss within the target material, the bending radius of the remaining beam gets softer with the target thickness according to Eq. (72) since the magnetic field strength was chosen to be constant for all runs of the same initial beam energy.

Before defining the final expression for the limited-acceptance correction factor, it is necessary to recall that all correction factors have to be related to the main quantity, the number of identified carbon isotopes with TODF (Eq. (71)). Fig. 42 shows the PSP versus Fiber X positions for the identified carbon isotopes with TOFD (green-shaded area). The sum of all data points in this plot is $N^{TOFD}_{Q6,\epsilon(Fib,PSP)}$. The blue-shaded areas illustrate the regions mostly affected by the limited geometrical acceptance.

The first step is to determine the number of particles that got lost due to the limited geometrical acceptance $N_{^{12}C,missing}$. Using this number, it is possible to define the ratio of all identified carbon isotopes with TOFD (N^{TOFD}_{Q6}) compared to the full or reconstructed ^{12}C distribution as the following:

$$A_C = \frac{N^{TOFD}_{Q6,\epsilon(Fib,PSP)}}{N_{^{12}C,missing,\epsilon(Fib,PSP)} + N^{TOFD}_{Q6,\epsilon(Fib,PSP)}}, \tag{77}$$

where the indices ϵ(Fib,PSP) indicate that all quantities depend on the same rate-

and time-dependent efficiency of the Fiber and PSP detectors.

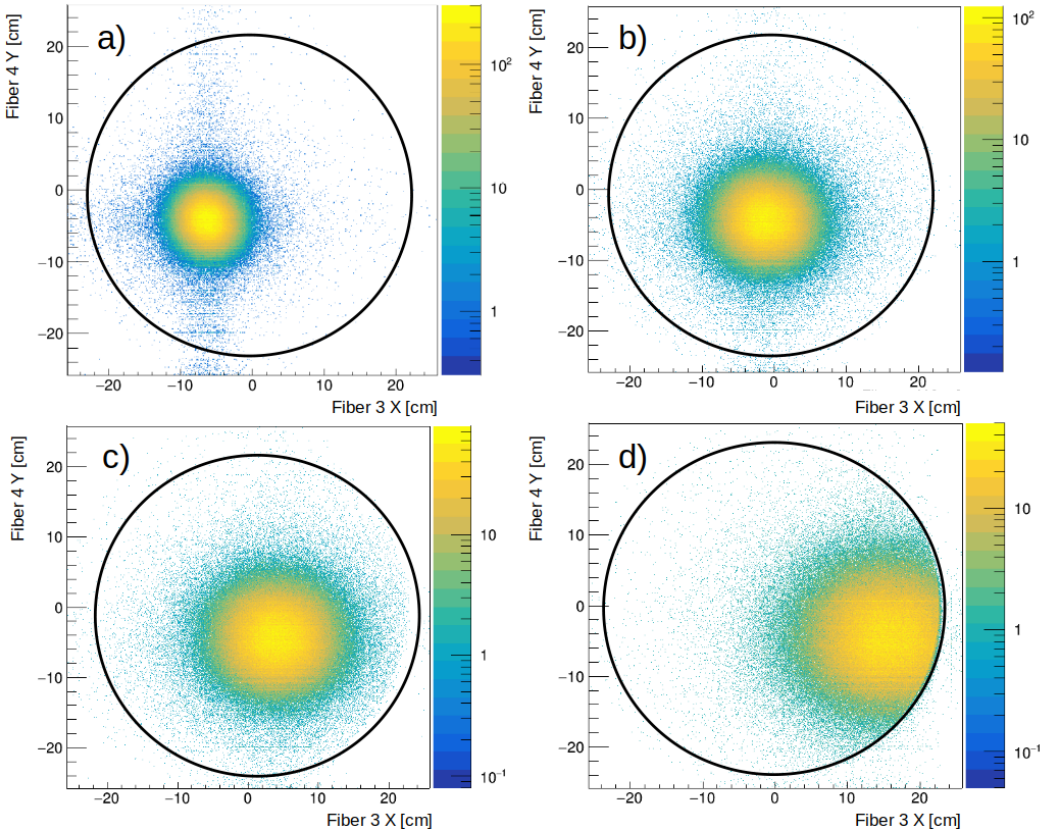

Figure 41: All panels are showing the XY position (Fiber 3 and Fiber 4) of the carbon beam after the exit of the vacuum pipe for a beam energy of 400 MeV/nucleon and different targets: Empty (a), thin carbon (b), medium carbon (c) and thick carbon (d).

The main assumption of this strategy is that the active area of Fiber 1 has 100 % geometrical acceptance for the ^{12}C isotopes. This was checked with data from a run with 400 MeV/nucleon and the thick carbon target. In this combination, the beam has the largest angular straggling in the target and setup material. In addition, in this configuration, we have the smallest bending radius and, thus, the highest deflection compared to the 18-degree line after the magnetic field.

The position distribution of the ^{12}C beam is illustrated in the left panel in Fig. 43 by the correlation between the horizontal position information in front (PSP3) and after the magnetic field (Fiber 1). The projection on the x-axis (Fiber 1) of this distribution is shown in the right panel of Fig. 43. A Gaussian was fitted to estimate the mean value (black vertical line) of the distribution. The active area of Fiber 1 fully covers the left tail of the distribution (green-shaded area). Whereas the right tail (red shaded area) might be cut and exceed the active area of Fiber 1.

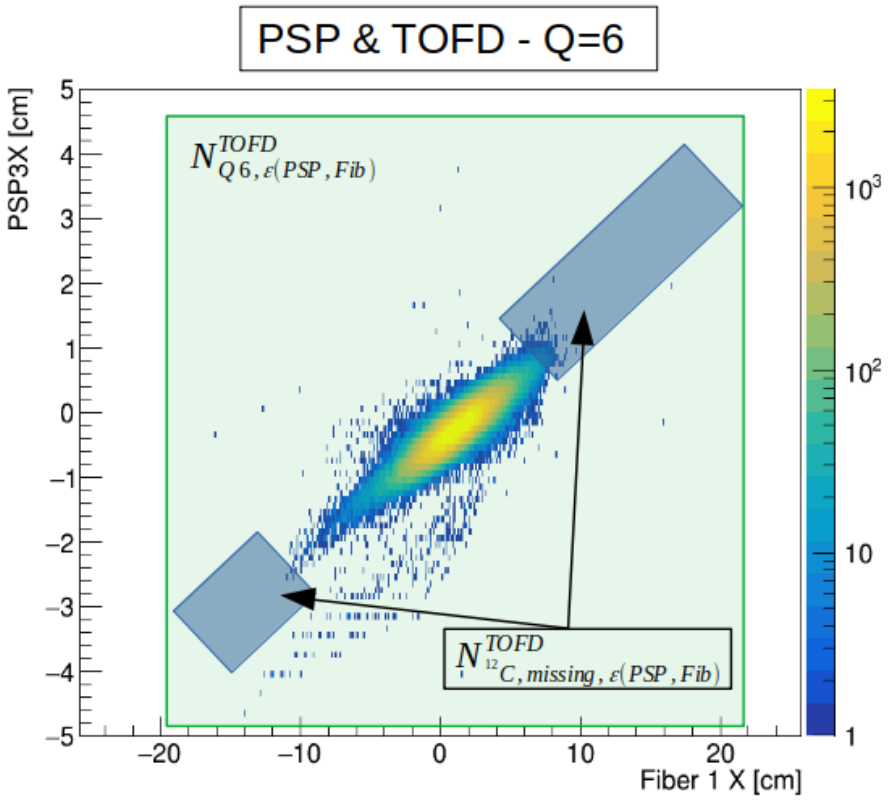

Figure 42: This plot shows all X positions of PSP3 versus Fiber 1 under the condition that TOFD identified a carbon isotope within the same event. The blue-shaded area indicates the main region of particle loss due to the limited geometrical acceptance.

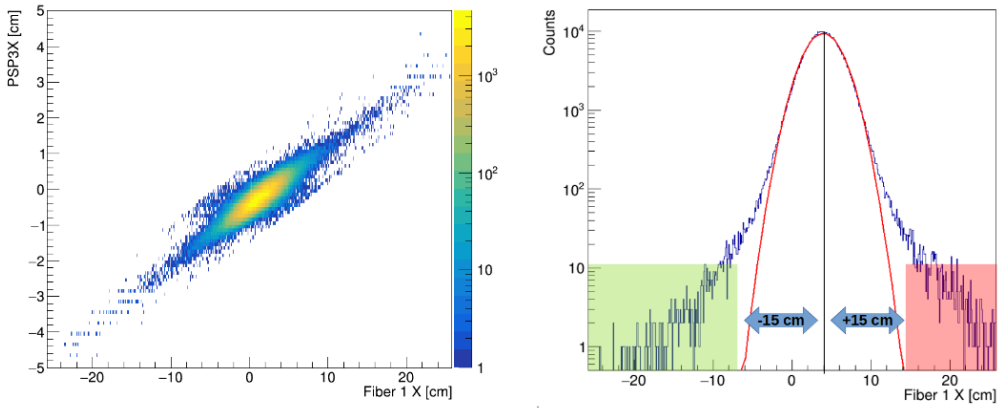

Figure 43: 2D and 1D position distribution of ^{12}C particles after the target. The shaded areas in the right panel indicate the tail regions, where the detector covers the beam distribution (green) or it might exceed the active area.

Two areas with the same distance with respect to the mean value of the Gaussian are defined to compare the integral of the right and left tails.
Even for this "extreme" situation, the integral of the green-shaded area (integral: 206 counts) is smaller than the red-shaded area (integral: 239 counts). This might be an effect of the statistical fluctuations in these areas. Nevertheless, these small values already prove that even if the distribution might exceed the active area, the effect must be smaller than any of the systematic or statistical uncertainty.

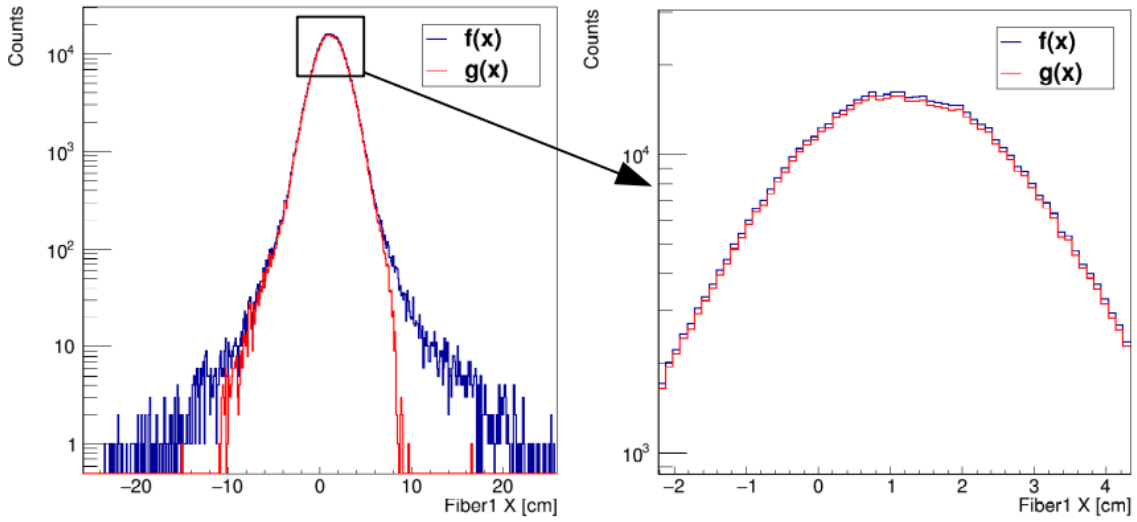

Figure 44: The left panels shows the 1D position distribution of the ^{12}C isotopes on the Fiber 1 plane. The blue graph - f(x) - illustrates the distribution with just the PSP-Q=6 condition. The red graph - g(x) - illustrates the same data set with the additional TOFD-Q=6 condition. The right panel shows the zoomed peak region of the lower left panel.

The left panel in Fig. 44 compares the 1D position distribution of the ^{12}C isotopes with just the PSP Q=6 condition in blue and the additional TOFD Q=6 condition in red. An enlarged view of the peak region (right panel) shows that besides the hard cut-off of the distribution tails, the statics also drop in the central region after applying the TOFD condition. This effect is related to reactions within the remaining setup material from Fiber 1 up to the TOFD detector. It is important to remind that reactions within the setup material are excluded by dividing a target-run by an empty-run (see Eq. (69)) and should not be corrected in this step. So, to use the blue "full-acceptance" distribution f(x) as a template for the limited-acceptance ^{12}C distribution g(x) in red, it has to be scaled down to compensate for the reactions in the remaining setup material.

The Scaling Factor

As mentioned above, the scaling factor represents the reaction probability within the setup material from Fiber 1 up to TOFD. It has thus to be determined for each run individually. For this purpose, it is necessary to define a region where the static drop is not caused by the limited geometrical acceptance but only by reactions in the setup. In the horizontal direction, this region can be defined by dividing the red limited-acceptance distribution g(x) by the blue full-acceptance distribution f(x) (see Fig. 45).

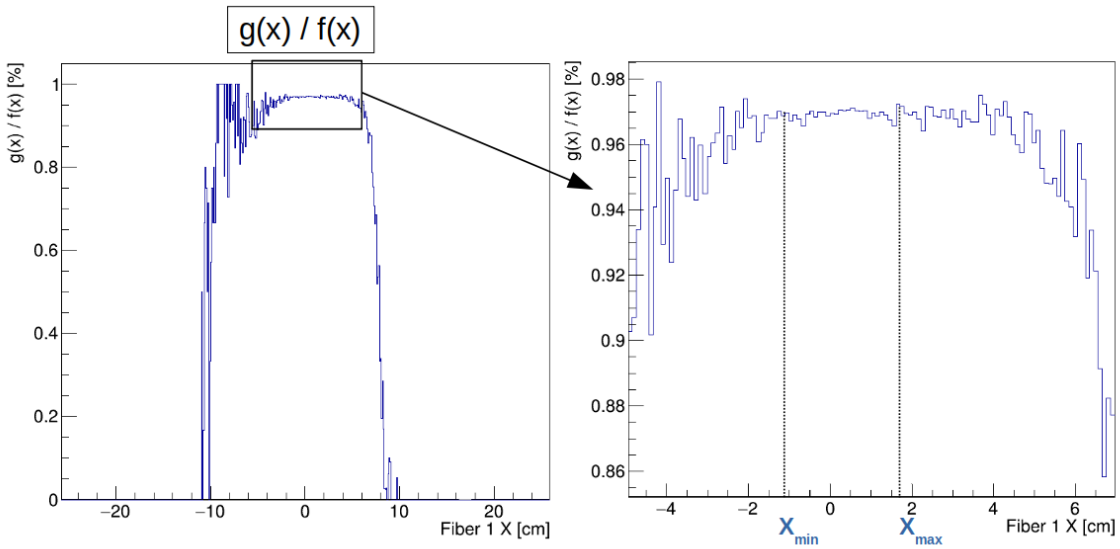

Figure 45: Ratio of limited-acceptance distribution g(x) and full-acceptance distribution f(x) position distribution. The right panel shows a detailed view of the indicated central area.

The plateau already indicates an almost constant region. Nevertheless, this region can also be affected by the limited geometrical acceptance in the vertical direction. This effect is illustrated in Fig. 46, where both panels show the XY position of PSP3 for particles with Q=6. In the right panel, the additional condition of TOFD Q=6 was added. Here, it is shown that even in the central region ($-1.5\text{cm} < \text{X} < +1.5\text{cm}$), the vertical direction is affected by the limited geometrical acceptance of the setup between Fiber 1 and TOFD. This effect is dominating for the low beam energy runs (400 and 550 MeV/nucleon) in combination with the medium and thick carbon targets since these combinations produce the largest energy loss and angular straggling for the remaining beam after the target.

Consequently, it is crucial to define a subset of g(x) and f(x) with the condition that the particle was passing PSP3 in a central Y-position, restricted by Y_{min} = -1.5 cm and Y_{max} = +0.5 cm, as indicated in the right panel of Fig. 46. These subsets will be named $\text{g}_{\text{S}}(\text{x})$ and $\text{f}_{\text{S}}(\text{x})$ in the following. This additional condition ensures that particles of this

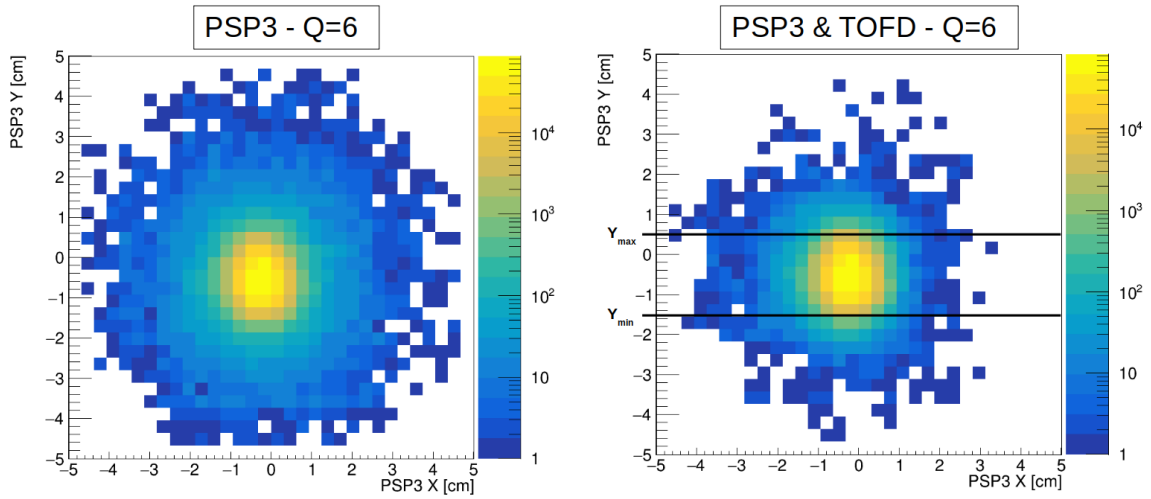

Figure 46: Both panels are showing the XY position of PSP3 for particles with Q=6. The right panel has the additional condition that TOFD has identified a particle with Q=6.

subset, which are passing PSP3 and Fiber 1 in a central X-Position, are not affected by the limited geometrical acceptance in Y-direction.
The following relation defines the scaling factor:

$$S = \frac{\int_{x_{min}}^{x_{max}} g_{S,\epsilon(Fib,PSP)}(x)}{\int_{x_{min}}^{x_{max}} f_{S,\epsilon(Fib,PSP)}(x)}, \tag{78}$$

where x_{min} and x_{max} are a lower and upper limit for the plateau area (see Fig. 45) and have to be defined for each beam energy and target individually. Since $g_S(x)$ is a subset of $f_S(x)$, the time- and rate-dependent efficiencies of Fiber 1 and PSP3 (ϵ(Fib,PSP)) are the same and cancel out by diving them. Therefore, the scaling factor S is not efficiency dependent.

Number of missing ^{12}C isotopes

The derived scaling factor is now used to compensate for the statistical difference between g(x) and f(x) caused by reactions within the setup material and thus the number of ^{12}C isotopes that are lost due to the geometrical acceptance is defined as:

$$N_{^{12}C,missing,\epsilon(Fib,PSP)} = \int_{Fib_{min}}^{Fib_{max}} f_{\epsilon(Fib,PSP)}(x) \cdot S - \int_{Fib_{min}}^{Fib_{max}} g_{\epsilon(Fib,PSP)}(x), \tag{79}$$

where Fib_{max} and Fib_{min} are indicating the area of the ^{12}C distribution in Fig. 44 which is affected by the limited geometrical acceptance. As discussed earlier in this chapter,

due to large scattering angles for low beam energies and thick targets, these limits represent the complete active area of the Fiber detector for this combination. In the case of high beam energies (650 - 1000 MeV/nucleon), the angular straggling gets less dominant in the central region (see XY beam position for all beam energy and target combinations in the appendix chapter). Therefore, the limited geometrical acceptance is dominant at the edges in the X direction of Fig. 44.

The Acceptance Correction Factor

Using Eqs. (77) to (79), it is possible to define the factor A_C, which is the ratio of identified carbon isotopes with TOFD compared to the full reconstructed ^{12}C distribution as

$$A_C = \frac{N_{Q6}^{\mathrm{TOFD}}}{\left(\int_{\mathrm{Fib_{min}}}^{\mathrm{Fib_{max}}} \mathrm{f(x)} \cdot \left(\frac{\int_{x_{\mathrm{min}}}^{x_{\mathrm{max}}} g_S(x)}{\int_{x_{\mathrm{min}}}^{x_{\mathrm{max}}} \mathrm{f}_S(x)} \right) - \int_{\mathrm{Fib_{min}}}^{\mathrm{Fib_{max}}} g(x) \right) + N_{Q6}^{\mathrm{TOFD}}} \tag{80}$$

As discussed previously in this chapter, all input parameters are subsets of the same data set and thus have again the same time- and rate-dependent efficiency dependency of the PSP and Fiber detectors (see Eq. (77) - Eq. (79)), which are canceling out by dividing all numbers. Therefore, the acceptance correction factor A_C is independent of the respective efficiencies.

Systematic Uncertainty

The most sensitive quantity in Eq. (80) is the scaling factor or, more precisely, the chosen limits $x_{\mathrm{min/max}}$, which are defining the integration area. To test this quantity in the case of its systematic uncertainty for A_C, both limits were shifted simultaneously by $\pm$ 3 mm to reduce and extend the integration area. The resulting values for A_C are plotted against the shift width in Fig. 47. The difference between the maximum and minimum value of A_C is taken as an upper limit for the systematic uncertainty for this correction factor.

Further, the influence of the position-dependent efficiency of the Fiber detectors was investigated. For this purpose, a fiber sweep-run was used, where both detectors (Fiber 1 and Fiber 2) were moved simultaneously vertically to the beam. In Fig. 48, the X position of Fiber 1 versus Fiber 2 for the sweep-run is plotted. The diagonal shows that the whole active area of both detectors was illuminated during that run.

In the first step, events where the PSP3 and TOFD detectors have registered a carbon (Q=6) particle were selected to ensure that both fiber detectors could have registered that particle and to exclude background events. Under that condition, one

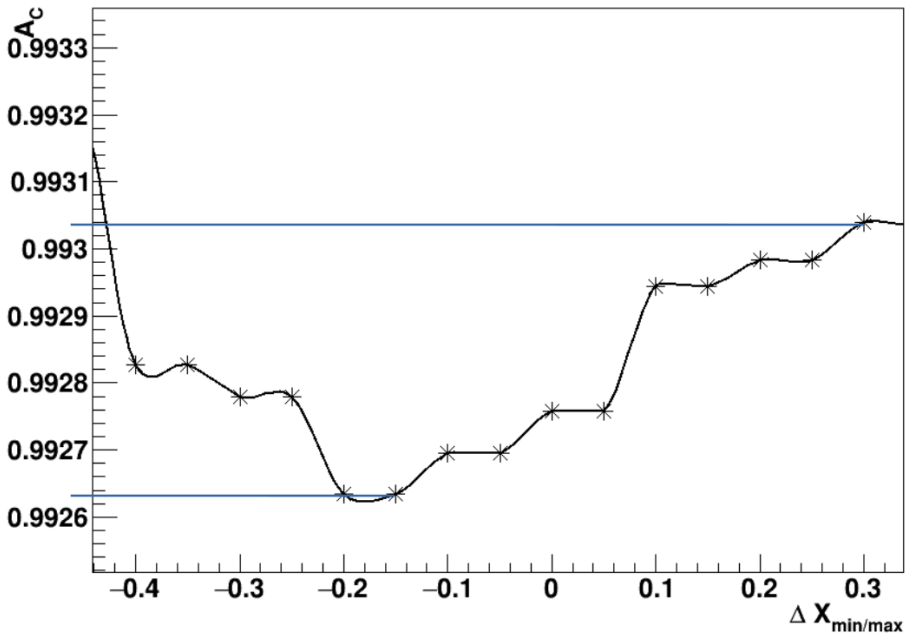

Figure 47: The Graph shows the resulting A_C factor for varying X_{min} and X_{max} values for a run with 400 MeV/nucleon and the medium carbon target.

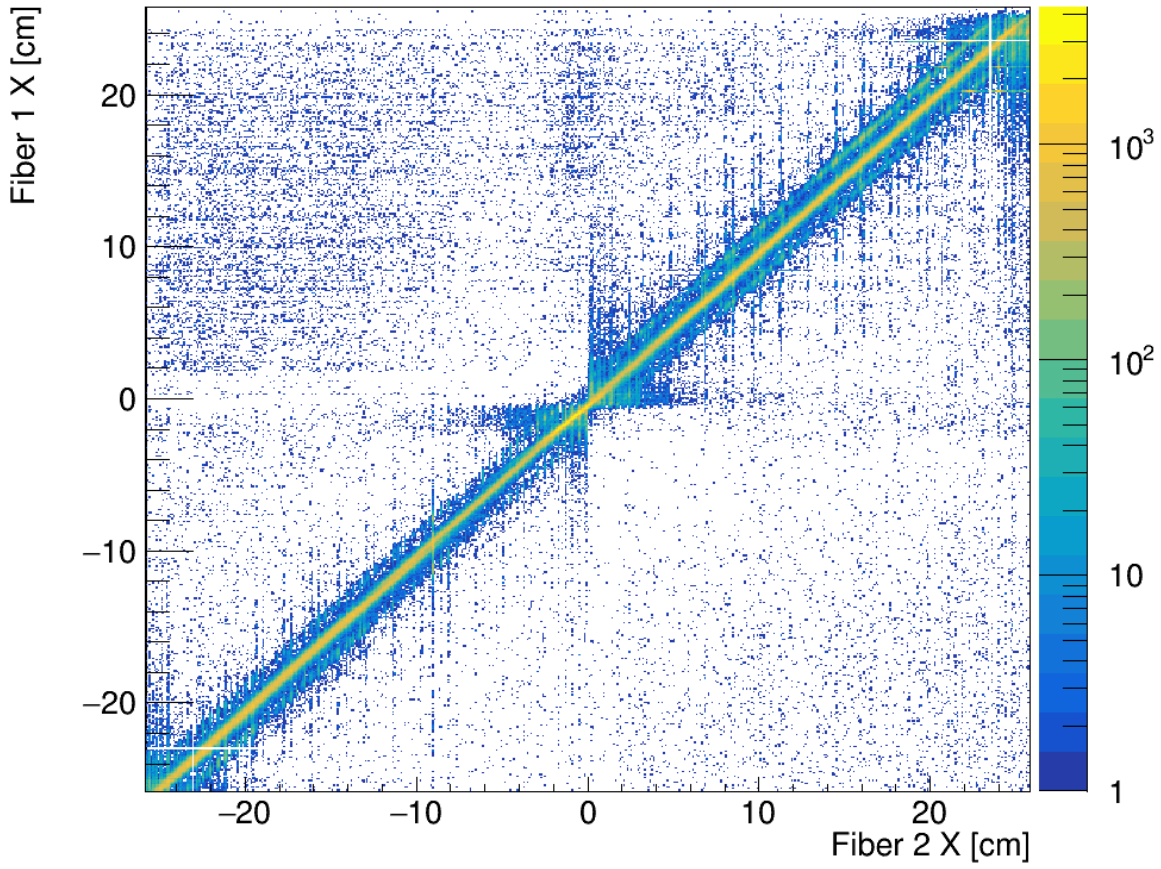

Figure 48: X-position information of Fiber 1 versus Fiber 2 for a sweep run.

hit for Fiber 1 per event with a reasonable energy loss and time difference with respect to the minimum bias trigger was chosen to avoid double-counting. For each event of this data set with a valid Fiber 1 hit, it was checked if Fiber 2 also registered a particle. By comparing the later subset with the data set of all valid Fiber 1 hits, an efficiency for each single fiber under the condition of detection in both detectors was estimated. This ratio is plotted in Fig. 49.

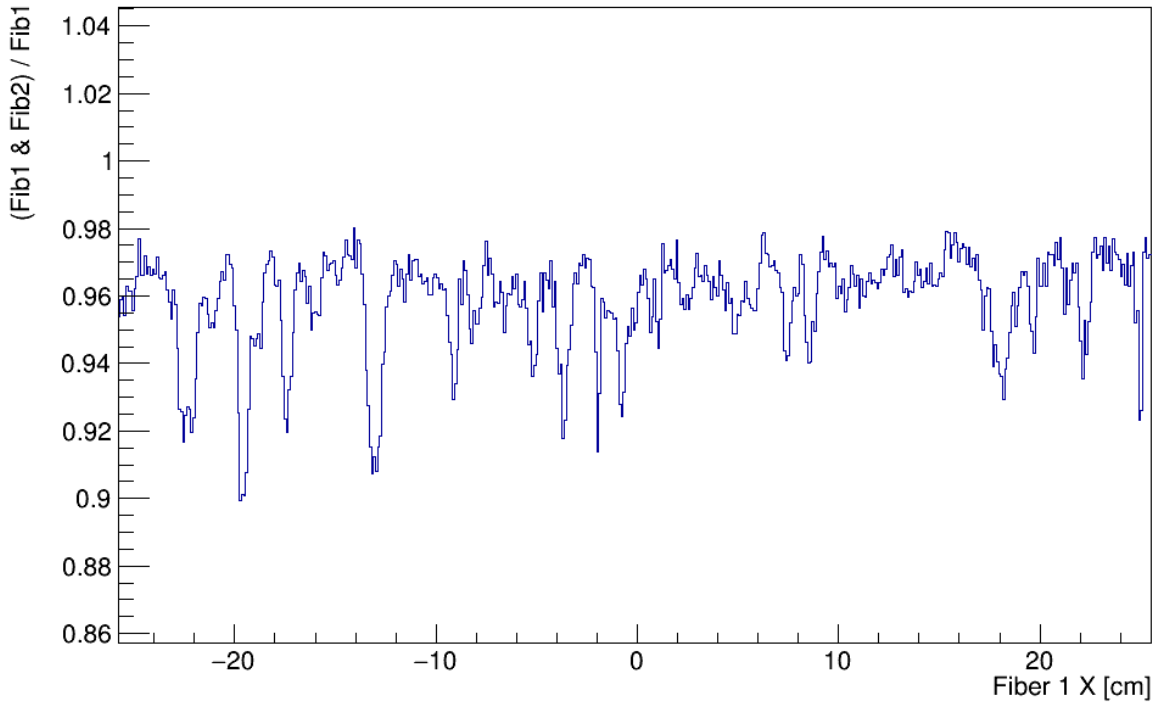

Figure 49: Efficiency per fiber for Fiber 1.

The efficiency is oscillating between 98% and 90% over the whole active area. To check the influence of such a fiber-dependent efficiency on the determination of the acceptance correction factor, the correspondent efficiency of each fiber was multiplied on both position distributions f(x) and g(x) (Fig. 44). The difference between the resulting acceptance correction factors with and without the position-dependent efficiency correction is for all target and beam energy combinations in the range of 0.008%. This is much smaller than the estimated systematic uncertainty of this correction factor. Since the oscillating efficiency is distributed over the whole active area of the Fiber detector and it has to be multiplied on both position distributions f(x) and g(x), the effect cancels in the first order. The remaining contribution will be added to the systematic uncertainty of the acceptance correction.
Table 6 summarizes the final values of A_C for all beam energy and target combinations together with the respective systematic uncertainties.

The final expression for the number of non-reacted ^{12}C particles reads as the follow-

A_C	400 MeV/nucleon	550 MeV/nucleon	650 MeV/nucleon	800 MeV/nucleon	1000 MeV/nucleon
Empty	0.99990(5)	0.99985(2)	0.99995(3)	0.99997(5)	0.99999(1)
thin	0.99691(20)	0.99832(20)	0.99933(10)	—	0.99982(10)
medium	0.99293(30)	0.99681(30)	0.99872(20)	0.99932(30)	0.99951(20)
thick	0.84063(40)	0.99042(20)	0.99682(30)	0.99781(10)	0.99851(20)

Table 6: Ratio of identified carbon isotopes with TOFD compared to the full reconstructed ^{12}C distribution.

ing:

$$N_2^{i/o} = \frac{N_{Q=6}^{TOFD}}{\epsilon_{Q=6}^{TOFD}} \cdot \left(1 - (1 - R_{^{12}C}) + \left(\frac{1}{A_C} - 1\right)\right) \tag{81}$$

4.6 Combined Statistical and Systematic Uncertainties

The statistical uncertainty of the Transmission method (Eq. (69)) is calculated using the Gaussian error propagation as

$$\Delta\sigma_{stat.} = \sqrt{\left(\frac{\partial\sigma_I}{\partial N_t}\Delta N_t\right)^2 + \left(\frac{\partial\sigma_I}{\partial R_i}\Delta R_i\right)^2 + \left(\frac{\partial\sigma_I}{\partial R_o}\Delta R_o\right)^2}, \tag{82}$$

where ΔN_t denotes the uncertainty of the target thickness measurement (as described in Section 3.5 and listed in Table 2) and $\Delta R_{i/o}$ are the standard errors of the independent binomial distributed quantities $R_{i/o}$:

$$\Delta R_{i/o} = \sqrt{\frac{R_{i/o}(1 - R_{i/o})}{N_1^{i/o}}} \tag{83}$$

The final expression of Eq. (82) is:

$$\Delta\sigma_{stat.} = \sqrt{\left(\frac{\sigma_I \Delta N_t}{N_t}\right)^2 + \frac{1}{N_t^2}\left(\frac{1 - R_i}{R_i N_1^i} + \frac{1 - R_o}{R_o N_1^o}\right)} \tag{84}$$

The systematic uncertainties of the different input quantities of Eq. (69) were discussed in their respective chapter and are listed in Tables 5 and 6.
The total systematic uncertainty of the cross-section includes the uncertainty of the target run and the empty run. Therefore, to calculate the total systematic uncertainty for the acceptance and the isotope correction factor, the following expressions based on the Gaussian error propagation were used:

$$\Delta\sigma_{\text{Acc.}} = \sqrt{\left(\frac{\partial\sigma_{\text{I}}}{\partial \text{A}^{\text{i}}_{\text{C}}}\Delta\text{A}^{\text{i}}_{\text{C}}\right)^2 + \left(\frac{\partial\sigma_{\text{I}}}{\partial \text{A}^{\text{o}}_{\text{C}}}\Delta\text{A}^{\text{o}}_{\text{C}}\right)^2} \tag{85}$$

$$\Delta\sigma_{\text{Iso.}} = \sqrt{\left(\frac{\partial\sigma_{\text{I}}}{\partial \text{R}^{\text{i}}_{^{12}\text{C}}}\Delta\text{R}^{\text{i}}_{^{12}\text{C}}\right)^2 + \left(\frac{\partial\sigma_{\text{I}}}{\partial \text{R}^{\text{o}}_{^{12}\text{C}}}\Delta\text{R}^{\text{o}}_{^{12}\text{C}}\right)^2}, \tag{86}$$

where $\Delta\text{A}^{\text{i/o}}_{\text{C}}$ and $\Delta\text{R}^{\text{i/o}}_{^{12}\text{C}}$ denote the uncertainties for the target and empty run listed in Tables 5 and 6.

5 Results and Discussion

In this chapter, the experimentally obtained total interaction cross sections of $^{12}C+^{12}C$ collisions at different incident beam energies are presented and discussed. The absolute cross section values and corresponding experimental uncertainties are based on the presented analysis (see Chapter 4). A direct comparison with experimental data from previous experiments is used to discuss the validity of the presented measurement and analysis method. Moreover, the presented results are used to challenge theoretical predictions based on the reaction model published in [42] and discussed in Chapter 2.

5.1 Total Interaction Cross-Section Results

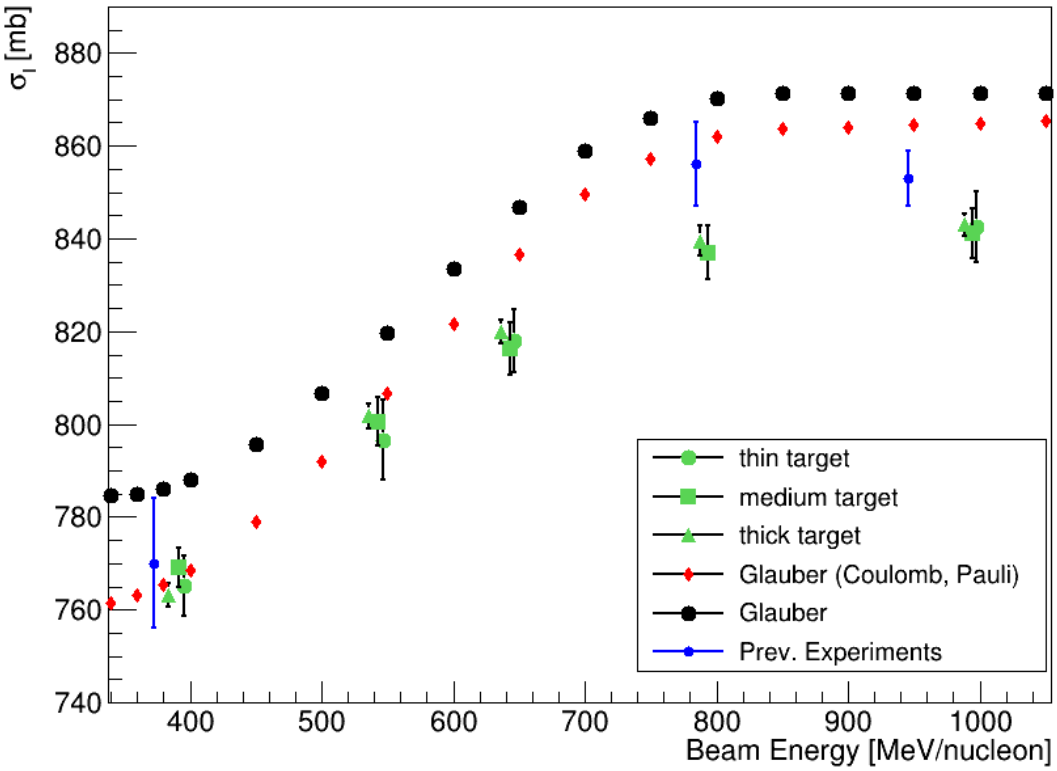

Figure 50: Total interaction cross-section of $^{12}C + ^{12}C$ versus the beam energy. Experimental data for all target beam combinations (green symbols) of the present work are compared with calculations (black and red symbols) based on the discussed reaction model (see Chapter2 and [42]) and data from previous experiments (blue symbols) by Takechi et al. [55], Tanihata et al. [54] and Ozawa et al. [56].

The results of the measured total interaction cross section of $^{12}C+^{12}C$ collisions are

summarized for all target and beam combinations in Table 7 and are plotted in Fig. 50 with green symbols. The independent statistical ($\Delta\sigma_{\text{stat.}}$) and systematic contribution ($\Delta\sigma_{\text{sys.}}$) are also listed in Table 7.

Beam Energy [MeV/nucleon]	^{12}C target	σ_{I} [mb]	$\Delta\sigma_{\text{stat.}}$ [mb]	$\Delta\sigma_{\text{sys.}}$ [mb]
400	thin	765.2(65)	5.41	3.60
	medium	769.2(42)	3.75	1.92
	thick	763.2(25)	1.86	1.69
550	thin	796.6(86)	8.15	2.86
	medium	800.5(52)	4.74	2.07
	thick	801.8(26)	2.47	0.92
650	thin	818.0(67)	6.24	2.42
	medium	816.3(56)	5.36	1.69
	thick	819.9(25)	2.30	1.07
800	medium	834.5(58)	5.26	2.34
	thick	836.2(32)	2.97	1.29
1000	thin	844.0(77)	7.45	1.92
	medium	841.3(54)	5.14	1.74
	thick	842.9(24)	2.27	0.77

Table 7: The measured total interaction cross-sections (σ_{I}) for all different beam and target combinations together with the independent statistical ($\Delta\sigma_{\text{stat.}}$) and systematic contributions ($\Delta\sigma_{\text{sys.}}$).

The total experimental uncertainty is dominated by the statistical contribution ($\Delta\sigma_{\text{stat.}}$). This emphasizes the usage of relatively thick reaction targets to minimize this uncertainty. Nevertheless, the investigation of absolute cross sections for specific reaction channels with thick targets requires a suitable experimental setup with corresponding acceptance. The large lever arm of TOFD enables a precise isotope separation, even for heavier nuclei than carbon. On the other hand, the geometrical acceptance of the same detector was limited in the presented experiment. The loss of acceptance amounts to several percent, especially for low beam energies (400 and 550 MeV/nucleon) in combination with the medium and thick carbon targets. This is also reflected in the systematic uncertainty $\Delta\sigma_{\text{sys.}}$ for these combinations. One reason is the increased angular straggling of particles after the target for lower beam energies. The main contribution to this limitation is a result of the constant magnetic field for one beam energy and all target combinations due to time constraints. The limited

geometrical acceptance and contamination of different carbon isotopes than ^{12}C in the TOFD data could be analyzed and compensated with efficiency-independent correction factors (see Section 4.5). A check of the validity of the ascertained correction factor can be seen in the agreement of the results with targets of different thicknesses. This minimizes the systematic uncertainty on the target specification or calculated number of scattering centers per unit area. The systematic uncertainties can be estimated as an upper limit, reflected in the small scattering of the three data points for one energy. The highest accuracy with a total uncertainty between $\pm 0.29\%$ and $\pm 0.39\%$ was achieved in measurements with the thick carbon target.

5.2 Comparison with Previous Experiments and Theory

The blue symbols in Fig. 50 denote results from previous experiments by Takechi et al.[55] (370 MeV/nucleon), Tanihata et al. [54] (790 MeV/nucleon) and Ozawa et al.[56] (950 MeV/nucleon). The results presented in this work agree with the experimental data at 370 and 950 MeV/nucleon within the given uncertainties but deviate from the data of Tanihata et al. by approximately 1.5 % (2 σ). Despite this relatively small discrepancy, the comparison with the blue data points shows that the presented experimental data reproduces the energy dependence of the total interaction cross section in the low and high-energy regions. This agreement with independent measurements also confirms the validity of the presented analysis method.

Calculated data points based on the Glauber model, published in [42] and discussed in Chapter 2, are represented by the black and red symbols in Fig. 50. The black data points are showing calculations that were performed without in-medium corrections. The red diamonds represent calculations, including Coulomb repulsion and Pauli blocking. It is visible that the not-corrected Glauber calculation cannot reproduce the experimental data, neither from previous experiments nor the presented data, and overestimates them by about 20 mb. This strongly emphasizes the inclusion of in-medium corrections to the reaction model, as discussed in Chapter 2. Pauli-Blocking reduces the cross section primarily for energies below 500 MeV/nucleon. Coulomb repulsion introduces a more constant reduction over the whole energy regime. The relatively large experimental uncertainties of Takechi et al. (370 MeV/nucleon), Tanihata et al. (790 MeV/nucleon) and Ozawa et al. (950 MeV/nucleon) do not allow for a precise statement on the predictive power of both model modifications. However, they already indicate that the medium-corrected Glauber calculations improve the agreement with experimental data at energies around 400 MeV/nucleon but still overestimate the same at energies between 800 and 1000 MeV/nucleon. The precise cross-section data presented in this work confirm this statement for the first time. For an initial beam energy of 400

and 550 MeV/nucleon, the obtained cross sections agree with the in-medium corrected Glauber calculation, thus verifying the proposed strength of in-medium modifications. The presented data show a softer rise of the cross section for higher energies, where the in-medium corrected Glauber calculation overestimates the experimental data by 2.5% at maximum energy. This discrepancy indicates an enhanced transparency of the nucleus at higher energies than expected from interpolating the free nucleon-nucleon cross section in the reaction model.

The origin of this effect could not be explained by theory so far. As reported in [42], additional in-medium modifications to the Glauber framework, such as Fermi motion, higher-order eikonal corrections, or relativistic corrections, modify the calculated cross section by less than 0.1 %. A systematic study on the influence of the density distribution on the cross-section calculation for ^{12}C+^{12}C collisions was presented in [46]. It was reported that an experimental uncertainty of 0.4 % for the charge radius of ^{12}C results in an uncertainty for the total interaction cross section of around ± 5mb. Therefore, this effect is also too small to explain the discrepancy between the presented total interaction cross section values and calculations at high energies.

It was discussed in Chapter 4 that in the case of ^{12}C+^{12}C collisions in the presented energy regime the total reaction cross section can be approximated with the total interaction cross section. Contributions to the total reaction cross section from inelastic excitation of the ^{12}C nucleus, which are included in the reaction model, were estimated to be smaller than the presented experimental uncertainty [57]. Whereas collective excitations are not included in the calculations but are identified in the measurement if they lead to particle evaporation. However, this would lead to an increase of the Glauber cross sections and thus would further increase the discrepancy with the experimental data. Therefore, the measurement of both inelastic contributions will not help to explain the discrepancy.

5.3 Discussion of further Investigations

It needs to be emphasized again that the discussed reaction model reproduces the experimental data at energies between 400 and 550 MeV/nucleon precisely. Even at higher energies, the agreement within 2.5 %, without using any free parameter but only realistic implemented in-medium modifications, is a remarkable result.

Nevertheless, the origin of the discrepancy between the presented experimental data and calculations at high energies remains an unanswered question. This exciting topic has to be investigated by both the theoretical and experimental sides in future work.

The high accuracy of the presented total interaction cross-section data allows for systematic studies of further in-medium modifications not included in the reaction model

so far.

A possible influence on the reaction or pion production probability might come from α-clusters of correlated nucleon-pairs inside the ^{12}C nucleus. These spatial nucleonic structures have been revealed by various experiments, e.g. using energetic probes like photons, pions, leptons, or hadrons [73]. Measuring total interaction cross sections with different composite projectiles could provide evidence of whether inner nuclear structure correlations, which are not considered in the global density distribution, influence the reaction probability. A direct comparison of total interaction cross sections of e.g. ^{4}He+p collisions with predictions based on the same reaction model discussed in this work, could indicate whether clustering inside the nucleus decreases the reaction probability. A similar approach would be measuring total interaction cross sections of ^{12}C+p. Suppose the enhanced transparency of composite nuclei arises from structure or binding effects. In that case, the relative discrepancy between experimental total interaction cross sections and theory should scale with the number of nucleons.

Another attempt would be to investigate the potential suppression of specific reaction channels in composite nuclei compared to nucleon-nucleon collisions. As discussed in Section 2.2, the dominant inelastic reaction channel in the presented energy regime is the one- and two-pion production. Compared to the charged-pion production, the interacting nucleons do not change their identity by creating a neutral pion. Therefore, the question is whether the neutral pion production could happen without interaction of the valence quarks, which define the charge radius of the nucleus, but by an interaction of the gluonic content of the nucleon. In a recent publication by Duran et al., a measurement of the gluonic form factor and a confining scalar gluon density envelope of the proton was presented [74]. If this gluon density envelope is modified by the binding energy in the nucleus, it could point to a new interpretation of the in-medium interaction range for pion productions of nucleons in a tightly bound system, which can explain the discrepancy between data and theory. Kinematically complete measurements of charged and neutral pion production reactions in nucleon-nucleon and nucleon-nucleus collisions could be used to study the energy-dependent evolution of the corresponding cross sections. A relatively softer increase of the neutral pion production cross section, than for charged pion, with increasing beam energy in nucleus-nucleus collisions compared to nucleon-nucleon collisions, could point to an in-modified interaction.

6 Summary

A precise measurement of the neutron-skin thickness of exotic nuclei will provide experimental constraints on the symmetry energy near saturation density and, thus, on the equation of state (EOS) of asymmetric nuclear matter. The measurement of total interaction and neutron-removal cross sections was proposed as a robust experimental tool to probe the neutron density distribution of exotic nuclei at relativistic energies. By directly comparing experimentally obtained total interaction cross sections with predictions based on a realistic reaction model, it is possible to determine the nucleon density distribution. In the case of the Glauber model, calculations are based on two input parameters: the free nucleon-nucleon cross section and the target and projectile density distribution. Adjusting the density distribution inside the nucleus with density functional theory calculations is used to reproduce the measured cross sections and constrain the predictions on the EOS symmetry energy and its slope parameter L. The measurement of the total interaction cross sections of ^{12}C+^{12}C collisions at relativistic energies represent the ideal case for a direct comparison with results based on a realistic reaction model since the charge radius of ^{12}C is well known from electron scattering data. The precise measurement of total interaction cross sections under those stable conditions is needed to quantify the uncertainty and, hence, the predictive power of the reaction model.

In the framework of this thesis, a precision experiment was prepared, performed and analyzed to study total interaction cross sections of ^{12}C+^{12}C collisions. The obtained cross-section data cover an energy range of 400 to 1000 MeV/nucleon with a total experimental uncertainty of down to 0.4 %, representing the most precise currently available data in this energy regime. The measurement is based on the transmission method, where the number of incoming and non-reacted ^{12}C nuclei before and after the reaction target were identified with high accuracy using the R^{3}B experimental setup. Cross-section data from previous experiments validate the measurement and analysis method of the presented work. The comparison with theoretical calculations, based on the Glauber model, verify the impact of in-medium modifications at low energies. The discrepancy between the reaction calculation and this new data is about 2.5% at high beam energies above 700 MeV/nucleon. The enhanced transparency of the ^{12}C nucleus at higher energies could not be explained in the Glauber model so far and has to be further investigated by theory and upcoming experiments.
A possible attempt for a future experiment would be to investigate the suppression of the reaction probability at higher energies using a liquid hydrogen target. If nucle-

onic structure effects cause the reduced reaction probability, the discrepancy between identical calculations, as discussed in Chapter 2, and measured ^{12}C+p total interaction cross sections should scale accordingly. In an adjusted complete-kinematics experiment, specific reaction channels could be identified and compared to those in nucleon-nucleon collisions. This might help to constrain the origin of the decreased reaction probability of composite nuclei at higher energies.

The presented analysis has proven the capability of the R^{3}B setup at FAIR for precise measurements of absolute cross sections. To constrain the symmetry energy L parameter by around ± 10 MeV with measurements of total reaction and charge-changing cross sections of neutron-rich nuclei, an experimental and theoretical uncertainty of better than 2 % is needed [38]. This experimental required accuracy was fulfilled in the presented work under stable conditions for ^{12}C+^{12}C collisions. Therefore, this work reconfirms the statement that R^{3}B at the FAIR facility will be the optimal experimental setup for proposed experiments to measure the neutron-skin thickness of exotic nuclei in nuclear fragmentation reaction and thus to constrain the symmetry energy slope parameter near saturation density.
As a final remark, the discussed discrepancy between experimental results and predictions from the Glauber reaction model might point to the conclusion that the model-dependent uncertainty of future experiments on the neutron-skin thickness in the energy regime between 400 and 600 MeV/nucleon is minimized. It was shown that integrated cross sections can be precisely reproduced in this regime by the discussed Glauber model without any free parameters for ^{12}C+^{12}C collisions. Nevertheless, a further investigation of this effect at higher energies is essential to understand how this scales with the mass number or isospin asymmetry. An agreement of experimental results and theoretical calculations within 2.5 % is still a remarkable result.

A Appendix

Total Interaction Cross-Section Calculations

Beam Energy [MeV/nucleon]	σ_I^{EOL} [mb]	$\sigma_I^{EOL,Corr}$ [mb]
180.0	811.4	765.1
200.0	801.9	760.5
220.0	795.6	758.3
240.0	791.8	757.9
260.0	789.9	758.8
280.0	789.3	760.7
300.0	787.4	760.9
320.0	785.5	760.8
340.0	784.7	761.6
360.0	784.9	763.2
380.0	786.0	765.5
400.0	787.9	768.6
450.0	795.6	778.9
500.0	806.6	791.9
550.0	819.6	806.6
600.0	833.4	821.7
650.0	846.9	836.5
700.0	859.0	849.5
750.0	866.0	857.2
800.0	870.1	862.0
850.0	871.2	863.6
900.0	871.3	864.1
950.0	871.3	864.5
1000.0	871.3	864.9
1050.0	871.3	865.3
1100.0	871.3	865.6
1150.0	871.3	865.8

Table 8: Calculated total interaction cross-sections of $^{12}C+^{12}C$ collisions, based on the reaction model discussed in Chapter 2 and published in [42], for different beam energies. The cross-section data was provided by Carlos Bertulani.

Additional Figures

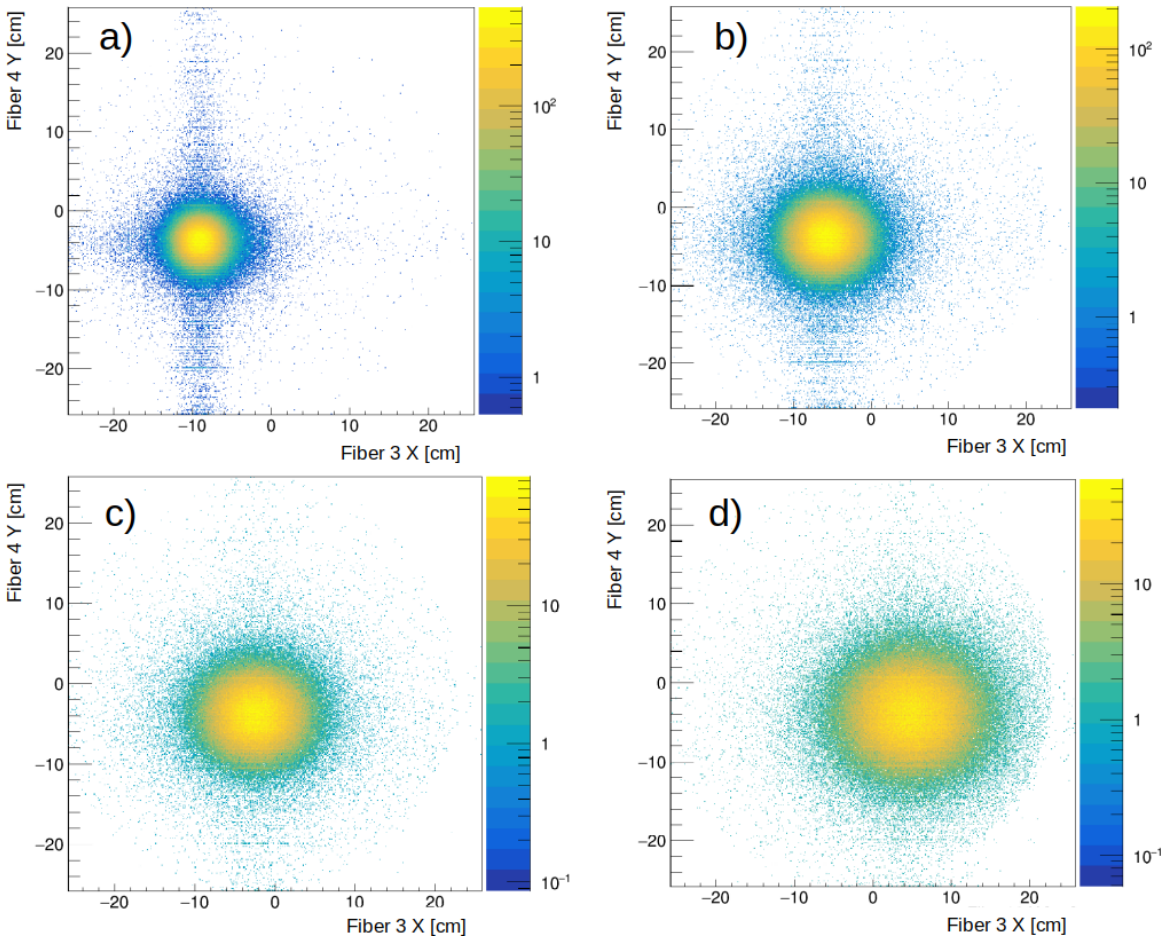

Figure 51: All panels are showing the XY-postion (Fiber 3 and Fiber 4) of the carbon beam after the exit of the vacuum pipe for beam energy of 550 MeV/nucleon and different targets: Empty (a), thin carbon (b), medium carbon (c) and thick carbon (d).

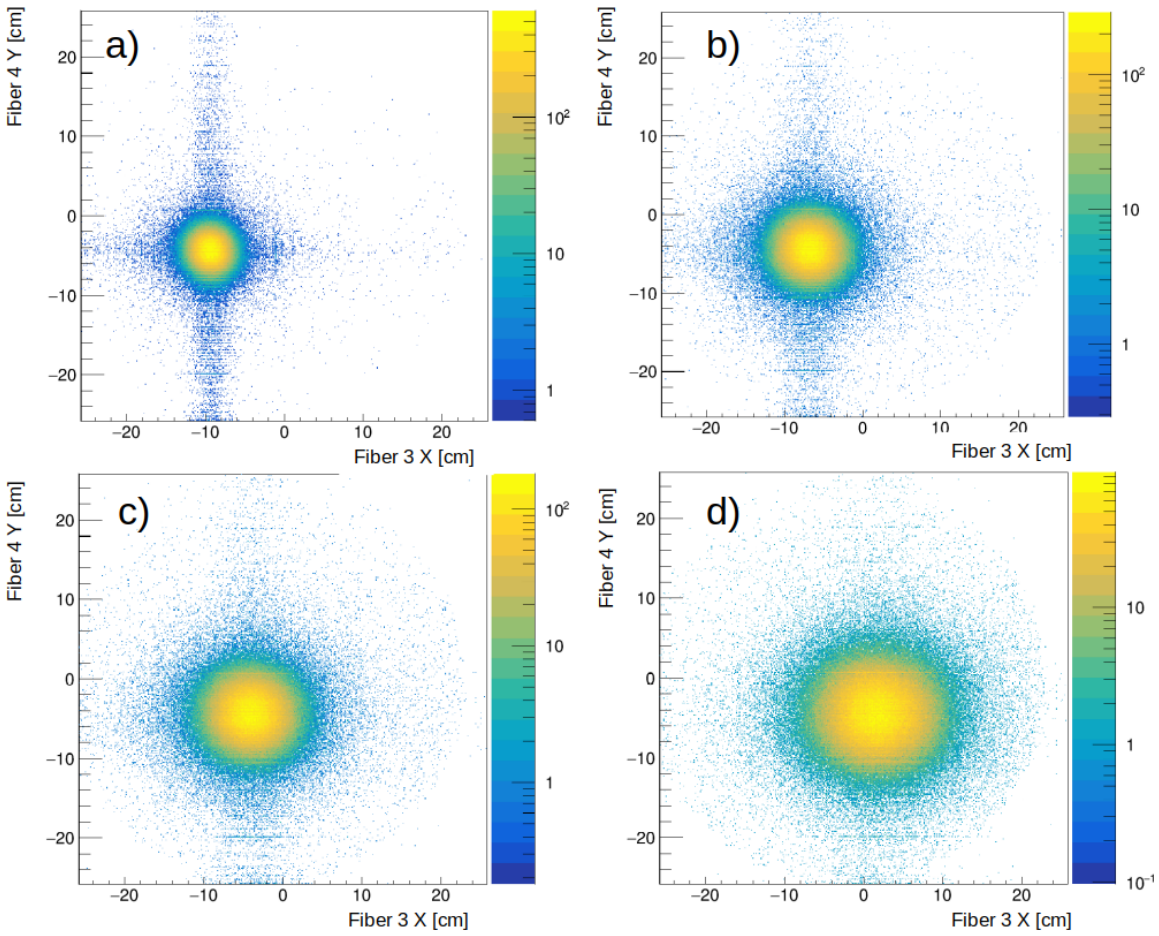

Figure 52: All panels are showing the XY-postion (Fiber 3 and Fiber 4) of the carbon beam after the exit of the vacuum pipe for beam energy of 650 MeV/nucleon and different targets: Empty (a), thin carbon (b), medium carbon (c) and thick carbon (d).

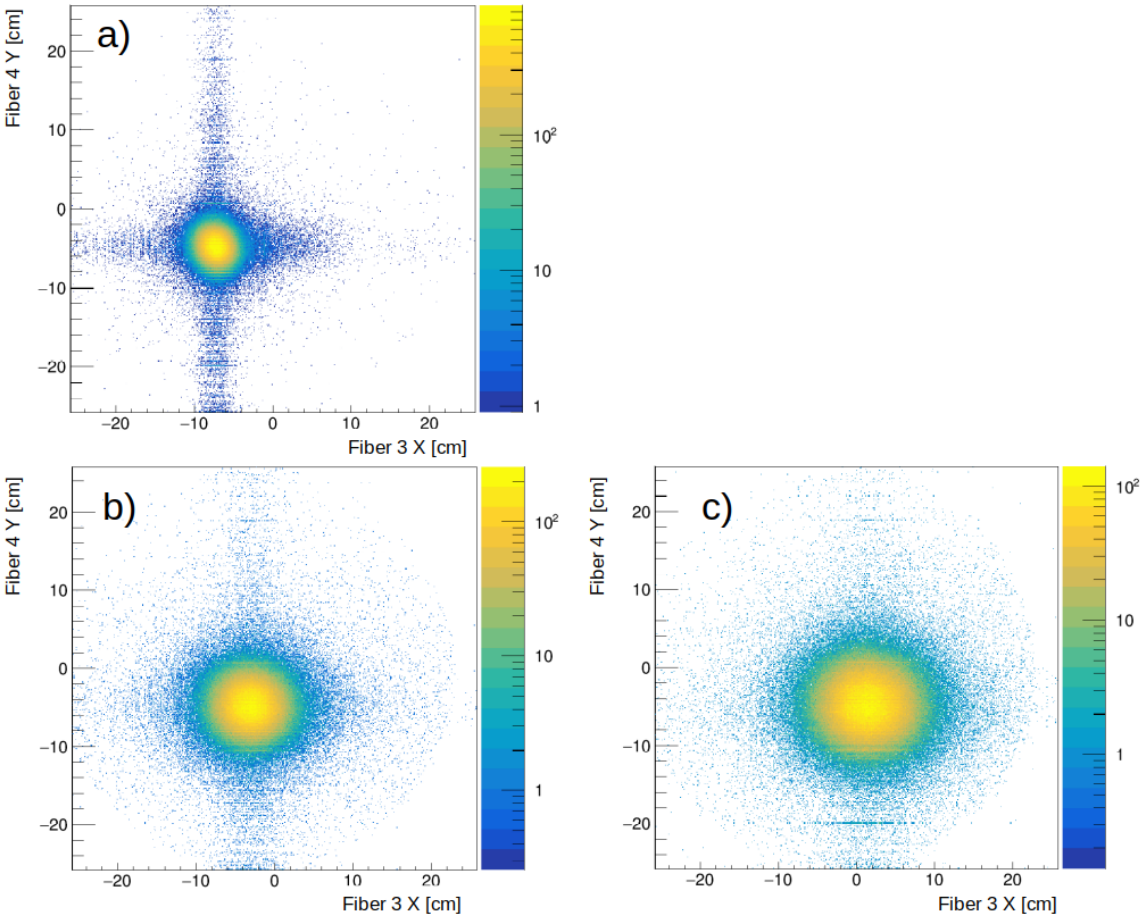

Figure 53: All panels are showing the XY-postion (Fiber 3 and Fiber 4) of the carbon beam after the exit of the vacuum pipe for beam energy of 800 MeV/nucleon and different targets: Empty (a), medium carbon (b) and thick carbon (c).

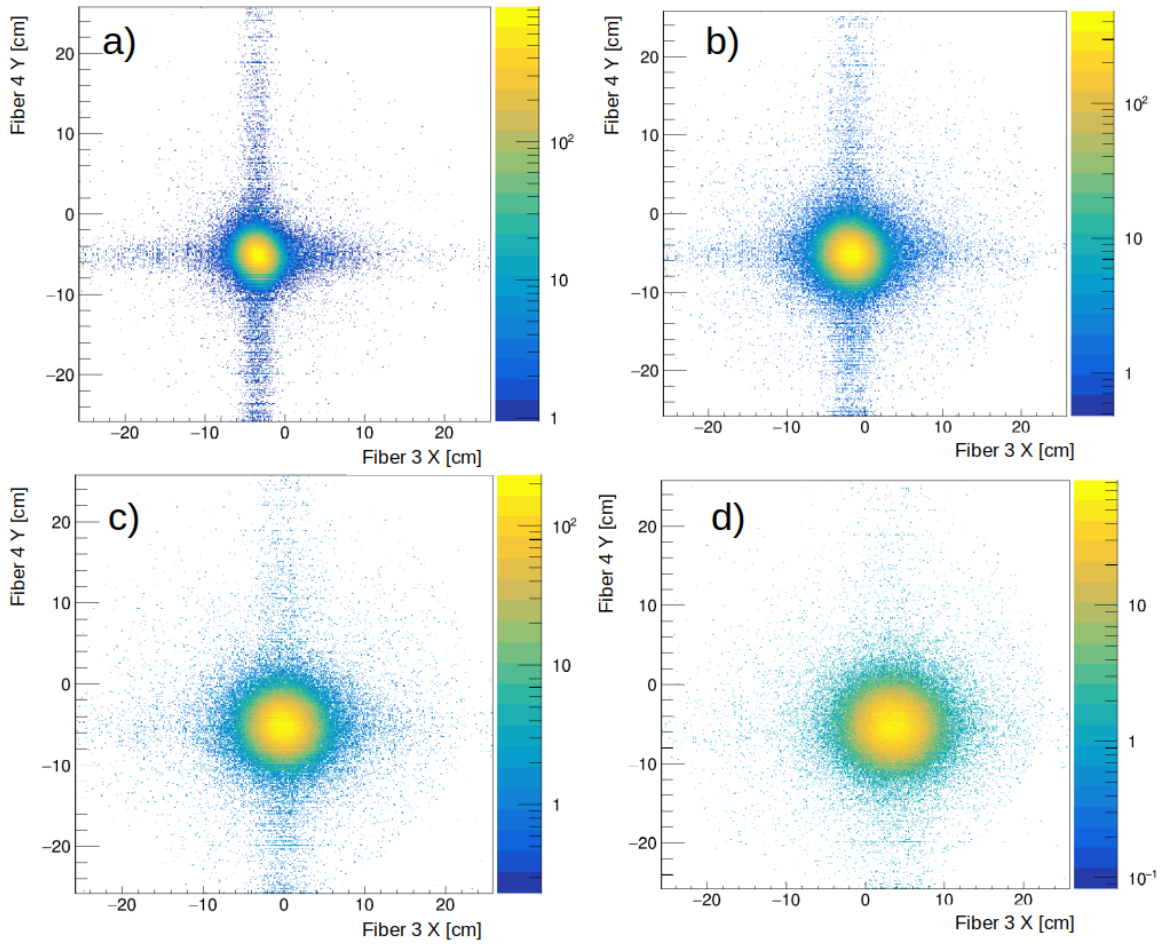

Figure 54: All panels are showing the XY-postion (Fiber 3 and Fiber 4) of the carbon beam after the exit of the vacuum pipe for beam energy of 1000 MeV/nucleon and different targets: Empty (a), thin carbon (b), medium carbon (c) and thick carbon (d).

References

[1] T. Aumann and C. A. Bertulani, "Indirect methods in nuclear astrophysics with relativistic radioactive beams," *Progress in Particle and Nuclear Physics*, vol. 112, p. 103753, 2020.

[2] J. Birkhan, M. Miorelli, S. Bacca, S. Bassauer, C. Bertulani, G. Hagen, H. Matsubara, P. von Neumann-Cosel, T. Papenbrock, N. Pietralla, *et al.*, "Electric dipole polarizability of ca 48 and implications for the neutron skin," *Physical review letters*, vol. 118, no. 25, p. 252501, 2017.

[3] T. Aumann and T. Nakamura, "The electric dipole response of exotic nuclei," *Physica Scripta*, vol. 2013, no. T152, p. 014012, 2013.

[4] C. Horowitz, S. J. Pollock, P. A. Souder, and R. Michaels, "Parity violating measurements of neutron densities," *Physical Review C*, vol. 63, no. 2, p. 025501, 2001.

[5] X. Roca-Maza, "Neutron skin of ^{208}Pb, nuclear symmetry energy and the parity radius experiment," *Phys. Lett.*, vol. 106, p. 252501, 2011.

[6] W. Baade and F. Zwicky, "Cosmic rays from super-novae," *Proceedings of the National Academy of Sciences*, vol. 20, no. 5, pp. 259–263, 1934.

[7] J. Chadwick, "Possible existence of a neutron," *Nature*, vol. 129, no. 3252, pp. 312–312, 1932.

[8] A. T. N. Facility, "ATNF pulsar catalogue." https://www.atnf.csiro.au/research/pulsar/psrcat/, june 2023.

[9] J. Lattimer, "Neutron stars and the nuclear matter equation of state," *Nucl. Part. Sci.*, vol. 71, no. 1, pp. 433–464, 2021.

[10] H.-T. Janka, F. Hanke, L. Hüdepohl, A. Marek, B. Müller, and M. Obergaulinger, "Core-collapse supernovae: Reflections and directions," *Progress of Theoretical and Experimental Physics*, vol. 2012, no. 1, p. 01A309, 2012.

[11] H.-T. Janka, "Explosion mechanisms of core-collapse supernovae," *Annual Review of Nuclear and Particle Science*, vol. 62, pp. 407–451, 2012.

[12] S. L. Shapiro and S. A. Teukolsky, *Black holes, white dwarfs, and neutron stars: The physics of compact objects*. John Wiley & Sons, 2008.

[13] J. M. Lattimer and M. Prakash, "The physics of neutron stars," *science*, vol. 304, no. 5670, pp. 536–542, 2004.

[14] J. Lattimer, "Constraining the symmetry parameters of the nuclear interaction," *The Astrophysical Journal*, vol. 771, no. 51, 2013.

[15] K. Sumiyoshi, T. Kojo, and S. Furusawa, "Equation of state in neutron stars and supernovae," *arXiv preprint arXiv:2207.00033*, 2022.

[16] G. Burgio, H.-J. Schulze, I. Vidaña, and J.-B. Wei, "Neutron stars and the nuclear equation of state," *Progress in Particle and Nuclear Physics*, vol. 120, p. 103879, 2021.

[17] B. P. Abbott, R. Abbott, T. Abbott, F. Acernese, K. Ackley, C. Adams, T. Adams, P. Addesso, R. Adhikari, V. B. Adya, *et al.*, "Gw170817: observation of gravitational waves from a binary neutron star inspiral," *Physical review letters*, vol. 119, no. 16, p. 161101, 2017.

[18] M. Miller, F. K. Lamb, A. Dittmann, S. Bogdanov, Z. Arzoumanian, K. C. Gendreau, S. Guillot, A. Harding, W. Ho, J. Lattimer, *et al.*, "Psr j0030+ 0451 mass and radius from nicer data and implications for the properties of neutron star matter," *The Astrophysical Journal Letters*, vol. 887, no. 1, p. L24, 2019.

[19] H. T. Cromartie, E. Fonseca, S. M. Ransom, P. B. Demorest, Z. Arzoumanian, H. Blumer, P. R. Brook, M. E. DeCesar, T. Dolch, J. A. Ellis, *et al.*, "Relativistic shapiro delay measurements of an extremely massive millisecond pulsar," *Nature Astronomy*, vol. 4, no. 1, pp. 72–76, 2020.

[20] J. R. Oppenheimer and G. M. Volkoff, "On massive neutron cores," *Physical Review*, vol. 55, no. 4, p. 374, 1939.

[21] J. Xu, Z. Zhang, and B.-A. Li, "Bayesian uncertainty quantification for nuclear matter incompressibility," *Physical Review C*, vol. 104, no. 5, p. 054324, 2021.

[22] A. Sorensen, K. Agarwal, K. W. Brown, Z. Chajecki, P. Danielewicz, C. Drischler, S. Gandolfi, J. W. Holt, M. Kaminski, C.-M. Ko, *et al.*, "Dense nuclear matter equation of state from heavy-ion collisions," *arXiv preprint arXiv:2301.13253*, 2023.

[23] M. Tsang, "Constraints on the symmetry energy and neutron skin from experiments and theory," *Phys. Rev. C*, vol. 86, no. 1, p. 015803, 2012.

[24] A. Brown, "Neutron radii in nuclei and the neutron equation of state," *Phys. Rev. Lett.*, vol. 85, pp. 5296–5299, 2000.

[25] S. Typel and B. A. Brown, "Neutron radii and the neutron equation of state in relativistic models," *Physical Review C*, vol. 64, no. 2, p. 027302, 2001.

[26] S. Typel, "Neutron skin thickness of heavy nuclei with α-particle correlations and the slope of the nuclear symmetry energy," *Phys. Rev. C*, vol. 89, no. 6, p. 064321, 2014.

[27] M. Bender, P.-H. Heenen, and P.-G. Reinhard, "Self-consistent mean-field models for nuclear structure," *Reviews of Modern Physics*, vol. 75, no. 1, p. 121, 2003.

[28] H. Sagawa and K. Hagino, "Theoretical models for exotic nuclei," *The European Physical Journal A*, vol. 51, pp. 1–31, 2015.

[29] C. Bertulani, H. Liu, and H. Sagawa, "Global investigation of odd-even mass differences and radii with isospin-dependent pairing interactions," *Physical Review C*, vol. 85, no. 1, p. 014321, 2012.

[30] I. Tanihata, H. Hamagaki, O. Hashimoto, Y. Shida, N. Yoshikawa, K. Sugimoto, O. Yamakawa, T. Kobayashi, and N. Takahashi, "Measurements of interaction cross sections and nuclear radii in the light p-shell region," *Physical Review Letters*, vol. 55, no. 24, p. 2676, 1985.

[31] P. Hansen and B. Jonson, "The neutron halo of extremely neutron-rich nuclei," *Europhysics Letters*, vol. 4, no. 4, p. 409, 1987.

[32] W. Mittig, J. Chouvel, Z. W. Long, L. Bianchi, A. Cunsolo, B. Fernandez, A. Foti, J. Gastebois, A. Gillibert, C. Grégoire, *et al.*, "Measurement of total reaction cross sections of exotic neutron-rich nuclei," *Physical Review Letters*, vol. 59, no. 17, p. 1889, 1987.

[33] R. Warner, J. Kelley, P. Zecher, F. Becchetti, J. Brown, C. Carpenter, A. Galonsky, J. Kruse, A. Muthukrishnan, A. Nadasen, *et al.*, "Evidence for a proton halo in b 8: Enhanced total reaction cross sections at 20 to 60 mev/nucleon," *Physical Review C*, vol. 52, no. 3, p. R1166, 1995.

[34] M. Fukuda, T. Ichihara, N. Inabe, T. Kubo, H. Kumagai, T. Nakagawa, Y. Yano, I. Tanihata, M. Adachi, K. Asahi, *et al.*, "Neutron halo in 11be studied via reaction cross sections," *Physics Letters B*, vol. 268, no. 3-4, pp. 339–344, 1991.

[35] T. Suzuki, H. Geissel, O. Bochkarev, L. Chulkov, M. Golovkov, D. Hirata, H. Irnich, Z. Janas, H. Keller, T. Kobayashi, *et al.*, "Neutron skin of na isotopes studied via their interaction cross sections," *Physical review letters*, vol. 75, no. 18, p. 3241, 1995.

[36] T. Suzuki, H. Geissel, O. Bochkarev, L. Chulkov, M. Golovkov, N. Fukunishi, D. Hirata, H. Irnich, Z. Janas, H. Keller, *et al.*, "Nuclear radii of na and mg isotopes," *Nuclear Physics A*, vol. 630, no. 3-4, pp. 661–677, 1998.

[37] L. Chulkov, G. Kraus, O. Bochkarev, P. Egelhof, H. Geissel, M. Golovkov, H. Irnich, Z. Janas, H. Keller, T. Kobayashi, *et al.*, "Interaction cross sections and matter radii of a= 20 isobars," *Nuclear Physics A*, vol. 603, no. 2, pp. 219–237, 1996.

[38] T. Aumann, "Peeling off neutron skins from neutron-rich nuclei: Constraints on the symmetry energy from neutron-removal cross section," *Phys. Rev. Lett.*, vol. 119, p. 262501, 2017.

[39] C. Bertulani and J. Valencia, "Neutron skins as laboratory constraints on properties of neutron stars and on what we can learn from heavy ion fragmentation reactions," *Physical Review C*, vol. 100, no. 1, p. 015802, 2019.

[40] W. Nörtershäuser and I. D. Moore, *Nuclear Charge Radii*, pp. 1–70. Singapore: Springer Nature Singapore, 2020.

[41] C. Bertulani and C. De Conti, "Pauli blocking and medium effects in nucleon knockout reactions," *Physical Review C*, vol. 81, no. 6, p. 064603, 2010.

[42] E. Teixeira, T. Aumann, C. Bertulani, and B. Carlson, "Nuclear fragmentation reactions as a probe of neutron skins in nuclei," *The European Physical Journal A*, vol. 58, no. 10, pp. 1–16, 2022.

[43] R. J. Glauber, "Lectures on Theoretical Physics - Vol 1," *Interscience Publishers Inc*, 1959.

[44] J. Al-Khalili, "An introduction to halo nuclei," in *The Euroschool Lectures on Physics with Exotic Beams, Vol. I*, pp. 77–112, Springer Berlin Heidelberg Berlin, Heidelberg, 2004.

[45] C. Bertulani and P. Danielewicz, "Introduction to Nuclear Reactions," *CRC Press*, vol. Second Edition, 2021.

[46] F. Schindler, *Total reaction, charge-changing, and neutron-removal cross sections of the heavy, neutron-rich nuclei 124Sn, 128Sn, 132Sn, and 134Sn measured with large acceptance at R3B.* PhD thesis, Technische Universität Darmstadt, 2017.

[47] C. Bertulani. private communication.

[48] M. S. Hussein, R. Rego, and C. A. Bertulani, "Microscopic theory of the total reaction cross section and application to stable and exotic nuclei," *Physics Reports*, vol. 201, no. 5, pp. 279–334, 1991.

[49] K. O. et al., "Data files and plots of cross-sections and related quantities in the 2014 review of particle physics." https://pdg.lbl.gov/2015/hadronic-xsections/, 2014.

[50] T. Mayer-Kuckuk, *Kernphysik: Eine Einführung*. Springer-Verlag, 2002.

[51] E. Rutherford, "Lxxix. the scattering of α and β particles by matter and the structure of the atom," *The London, Edinburgh, and Dublin Philosophical Magazine and Journal of Science*, vol. 21, no. 125, pp. 669–688, 1911.

[52] M. Takechi, M. Fukuda, M. Mihara, K. Tanaka, T. Chinda, T. Matsumasa, M. Nishimoto, R. Matsumiya, Y. Nakashima, H. Matsubara, *et al.*, "Reaction cross sections at intermediate energies and fermi-motion effect," *Physical Review C*, vol. 79, no. 6, p. 061601, 2009.

[53] A. S. Goldhaber, "Statistical models of fragmentation processes," *Physics Letters B*, vol. 53, no. 4, pp. 306–308, 1974.

[54] I. Tanihata in *Proceedings of the First International Conference on Radioactive Nuclear Beams: 16-18 October 1989, University of California at Berkeley, Lawrence Berkeley Laboratory, Berkeley, California*, p. 477, World Scientific Publishing Company Incorporated, 1990.

[55] M. Takechi, M. Fukuda, M. Mihara, K. Tanaka, T. Chinda, T. Matsumasa, M. Nishimoto, R. Matsumiya, Y. Nakashima, H. Matsubara, K. Matsuta, T. Minamisono, T. Ohtsubo, T. Izumikawa, S. Momota, T. Suzuki, T. Yamaguchi, R. Koyama, W. Shinozaki, M. Takahashi, A. Takizawa, T. Matsuyama, S. Nakajima, K. Kobayashi, M. Hosoi, T. Suda, M. Sasaki, S. Sato, M. Kanazawa, and A. Kitagawa, "Reaction cross sections at intermediate energies and fermi-motion effect," *Phys. Rev. C*, vol. 79, p. 061601, Jun 2009.

[56] A. Ozawa, O. Bochkarev, L. Chulkov, D. Cortina, H. Geissel, M. Hellström, M. Ivanov, R. Janik, K. Kimura, T. Kobayashi, A. Korsheninnikov, G. Münzenberg, F. Nickel, Y. Ogawa, A. Ogloblin, M. Pfützner, V. Pribora, H. Simon, B. Sitár, P. Strmen, K. Sümmerer, T. Suzuki, I. Tanihata, M. Winkler, and K. Yoshida, "Measurements of interaction cross sections for light neutron-rich nuclei at relativistic energies and determination of effective matter radii," *Nuclear Physics A*, vol. 691, no. 3, pp. 599–617, 2001.

[57] J. Y. Hostachy, "Elastic And Inelastic Scattering Of ^{12}C Ions At Intermediate Energies," *Nuclear Physics A*, vol. 490, pp. 441–470, 1988.

[58] Beschleunigeranlage, "GSI." https://www.gsi.de/, july 2023.

[59] R. Collaboration *et al.*, "A universal setup for kinematical complete measurements of reactions with relativistic radioactive beams (r3b), letter of intent, 2004," *See< http://www-win. gsi. de/r3b/Documents/LoI-R3B-final. pdf.*

[60] D. Rossi, P. Adrich, F. Aksouh, H. Alvarez-Pol, T. Aumann, J. Benlliure, M. Böhmer, K. Boretzky, E. Casarejos, M. Chartier, *et al.*, "Measurement of the dipole polarizability of the unstable neutron-rich nucleus ni 68," *Physical review letters*, vol. 111, no. 24, p. 242503, 2013.

[61] L. T. Bott, K. Göbel, M. Heil, A. Kelić-Heil, R. Reifarth, M. Aliotta, T. Almusidi, H. Alvarez-Pol, L. Atar, L. Atkins, *et al.*, "Coulomb dissociation of 16o into 4he and 12c," in *EPJ Web of Conferences*, vol. 279, p. 04003, EDP Sciences, 2023.

[62] C. Collaboration *et al.*, "Technical report for the design construction and commissioning of the califa endcap," tech. rep., Technical report, 2014.

[63] P. Cabanelas, D. González, H. Alvarez-Pol, J. Boillos, E. Casarejos, J. Cederkall, D. Cortina, M. Feijoo, D. Galaviz, E. Galiana, *et al.*, "Performance recovery of long csi (tl) scintillator crystals with apd-based readout," *Nuclear Instruments and Methods in Physics Research Section A: Accelerators, Spectrometers, Detectors and Associated Equipment*, vol. 965, p. 163845, 2020.

[64] A. Knyazev, J. Park, P. Golubev, J. Cederkäll, H. Alvarez-Pol, J. Benlliure, P. Cabanelas, E. Casarejos, L. Causeret, D. Cortina-Gil, *et al.*, "Simulations of light collection in long tapered csi (tl) scintillators using real crystal surface data and comparisons to measurement," *Nuclear Instruments and Methods in Physics Research Section A: Accelerators, Spectrometers, Detectors and Associated Equipment*, vol. 1003, p. 165302, 2021.

[65] C. Collaboration *et al.*, "Technical report for the design construction and commissioning of the califa barrel," tech. rep., Technical Report, 2012.

[66] R. collaboration *et al.*, "Technical report for the design, construction and commissioning of neuland: The high-resolution neutron time-of-flight spectrometer for r3b," *GSI and Collaborators*, 2011.

[67] M. Heil, A. Kelić-Heil, L. Bott, T. Almusidi, H. Alvarez-Pol, L. Atar, L. Atkins, T. Aumann, J. Benlliure, K. Boretzky, *et al.*, "A new time-of-flight detector for the r 3 b setup," *The European Physical Journal A*, vol. 58, no. 12, p. 248, 2022.

[68] H. T. Johansson, "UCESB - Unpack & Check Every Single Bit." http://fy.chalmers.se/~f96hajo/ucesb/, Aug 2023.

[69] CERN, "ROOT - Data Analysis Framework." https://root.cern.ch/, Aug 2023.

[70] D. Bertini, "R3broot, simulation and analysis framework for the r3b experiment at fair," in *Journal of Physics: Conference Series*, vol. 331, p. 032036, IOP Publishing, 2011.

[71] M. S. Ltd, "Micron X5." http://www.micronsemiconductor.co.uk/product/x5/, Aug 2023.

[72] I. Tanihata, H. Savajols, and R. Kanungo, "Recent experimental progress in nuclear halo structure studies," *Progress in Particle and Nuclear Physics*, vol. 68, pp. 215–313, 2013.

[73] R. Dalal and I. MacGregor, "Nucleon-nucleon correlations inside atomic nuclei: synergies, observations and theoretical models," *arXiv preprint arXiv:2210.06114*, 2022.

[74] B. Duran, Z.-E. Meziani, S. Joosten, M. Jones, S. Prasad, C. Peng, W. Armstrong, H. Atac, E. Chudakov, H. Bhatt, *et al.*, "Determining the gluonic gravitational form factors of the proton," *Nature*, vol. 615, no. 7954, pp. 813–816, 2023.

List of Figures

List of Tables

Acknowledgement

Als erstes möchte ich mich bei Laura Fabbietti und den Mitgliedern des E62-Lehrstuhls bedanken dass ich Teil dieses großartigen Teams sein durfte.

Eine ganz besonderen Dank möchte ich an Roman Gernhäuser dafür ausprechen dass er mir die Möglichkeit gegeben hat dieses Projekt zu verwirklichen, Erfahrungen auf einer Vielzahl an Experimenten sammeln durfte und Teil der R^3B Kollaboration zu werden. Ohne deine Betreuung, Erklärungen zu Detektoren, die Diskussionen über meine Ergebnisse und Physik, und deine krititschen Kommentare zu jedem Vortrag und Abstract wäre ich nicht so weit gekommen.

Bei Thomas Aumann und Carlos Bertulani möchte ich für die Möglichkeit bedanken dieses Experiment zu analysieren und auch für die Gespärche über die Theory und Hintergrund der Messung.

Ich möchte mich ganz speziell bei Petra Zweckinger und Ralf Lang dafür bedanken dass ich bei euch immer ein offenes Ohr und Hilfe für alles mögliche bekommen habe. Ohne euch beide würde hier nichts laufen.
Hierbei will ich mich auch bei der ganzen Mittagsessen-Crew Roman, Petra, Ralf und Dominik bedanken. Die Pause pünktlich um 11 Uhr und die Gespräche mit euch waren immer eine schöne Zeit auf die ich mich gefreut habe. Auch Jürgen Friese und Sissy Körner möchte ich für all die Gespräche im Seminarraum danken und dass auch ihr immer ein offenes Ohr für mich hattet.

Meinen Büro-Kollegen Tobias Jenegger, Philipp Klenze und Laszlo Varga möchte ich für die tolle Zeit und Arbeitsatmosphäre in unserem Container danken.

Desweiteren möchte ich allen meinen Kollegen der R^3B Kollaboration danken. Ohne euch wäre das Experiment dieser Arbeit nicht möglich gewesen. Auch möchte ich mich für die schöne Zeit und tollen Gespräche während all unserer Experimente und Kollaborations-Meetings bei euch bedanken.

Zuletzt möchte ich mich bei meinen Eltern, Geschwistern und Freunden für all die Unterstützung während der letzten Jahre bedanken. Dafür dass ihr immer für mich da wart wenn ich mal eine Ablenkung gebraucht habe und dass ihr mir bei all meinen Entscheidungen den Rücken gestärkt habt. Ganz besonders möchte ich mich natürlich bei Lotte dafür bedanken dass du mich immer unterstützt hast, so verstädnisvoll für alle meine Launen in stressigen Phasen warst und mich auf diesem Weg begleitet hast.